博士論文

Experimental Verification and Numerical Analysis on the Excitation and Propagation of Electron Bernstein Waves in the Internal Coil Torus Plasmas

(内部導体トーラスプラズマにおける電子バーンスタイン波の
励起・伝搬に関する実験的検証と数値解析)

内島　健一朗

新領域創成科学研究科
先端エネルギー工学専攻

Acknowledgement

I would like to thank my supervisor Professor Ogawa for his long time supervision in my research. He taught me the fundamental of plasma physics, what is the research, how to presentation, and so on. Even though I'm not so good student, Professor Ogawa taught and given me a lot of things for very long time.

I also would like to thank Mr. Morikawa. He taught me how to do the experiment, and what is the experiment. It's no exaggeration to say that all my skill for doing the experiment is given by him. He advised me any time when I'm in trouble with the experiment.

For the previous research, I'd like to thank my seniors. Dr. Yatsuka, Mr. Kinjo and all researchers in previous researches made the chance to start my research. My research is standing on the grand seniors works. I'd like to thank all of them again.

In my student life, my friends in the laboratory give me a lot of wonderful time. Discussion with them gives me many hints of my research, and talking with them makes me happy. One of the most wonderful things I got in my student life is the encounter with them. I would like to thank my dear friends.

Finally, I would like to thank my family. Any time when I'm in trouble, they shear my sadness, any time when I feel happy, they shear my happiness. The existence of my family helps me and gives me the powers in any time. Because of their encouragement, I can write this article.

Contents

Figure List

Chapter 1
Introduction

1.1 Nuclear Fusion Energy

1.1.1 Nuclear Fusion

The nuclear fusion is one of the advanced energy resource for the electric power plant and the research and development are being pushed forward. Nuclear fusion is a process that produces heavy nucleus by collision reaction of light nucleus, and an atomic reaction causes mass defects and generates a huge amount of energy. At this time, fusion reactions that are thought to be available on the earth are as following reactions;

$$D + T \rightarrow {}^{4}He(3.52MeV) + n(14.06MeV) \quad (1.1)$$

$$D + D \rightarrow T(1.01MeV) + p(3.03MeV) \quad (1.2)$$

$$D + D \rightarrow {}^{3}He(0.82MeV) + n(2.45MeV) \quad (1.3)$$

$$D + {}^{3}He \rightarrow {}^{4}He(3.67MeV) + p(14.67MeV). \quad (1.4)$$

Nuclear fusion can be caused by hitting particle beam on light nucleus, but in such a way most of the beam energy is wasted on the ionization of the target particles and the thermalization by elastic scattering before the fusion reaction. Therefore, nuclear fusion utilizing high temperature plasma has been researched. If high temperature plasma, where the particles are separated into ions and electrons, can be confined in a certain region, ions collide with each other with overcoming the electric repulsive force and nuclear fusion reaction is expected.

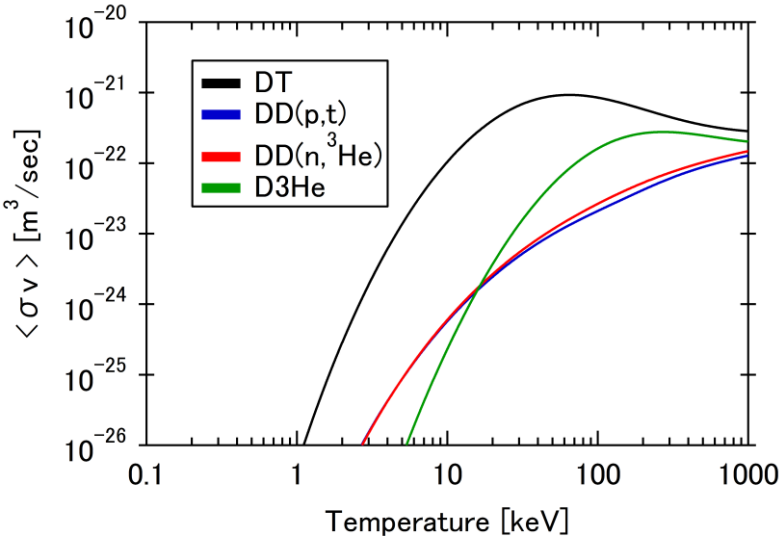

Figure 1.1: Maxwellian fusion reactivities for D-T, D-D and D- ^{3}He

1.1.2 Nuclear Fusion Reactivity

Nuclear fusion reaction requires approaching less than the distance working nuclear force with overcoming Coulomb repulsive force. Probability of fusion reaction is referred as fusion reactivity which is a product of reaction cross section σ and relative velocity v of each nucleus and product of two nucleus's density and fusion reactivity has the dimension of reaction times per unit volume and unit time. Maxwellian averaged reactivity $< \sigma v >$ is a function of temperature, and those of Eqs. (1.1) ~ (1.4) are in the nuclear data file issued by INDC (International Nuclear Data Committee) in IAEA [1]. Figure 1.1 shows temperature dependence of fusion reactivity $< \sigma v >$ curves [2] [3]. D-T reaction has the most probability and the curve of this reaction has a peak value at nearly 50 keV. To cause effective fusion reactions, it is necessary to heat fuel particles at least the order of ~10 keV.

1.1.3 Energy Confinement

Energy confinement is an important concept for nuclear fusion energy. Thermal energy of the plasma is referred as $(3/2)n\kappa(T_e + T_i)$, where n, κ, T_e and T_i

denote plasma density, Boltzmann constant, electron temperature and ion temperature, respectively and plasma confinement time τ is defined as

$$\tau \equiv \frac{(3/2)n\kappa(T_e + T_i)}{P_{loss}} \approx \frac{3n\kappa T}{P_{loss}}, \tag{1.5}$$

where P_{loss} is energy loss per unit volume and unit time. In order for plasmas to retain high temperature, it is necessary to balance energy loss and heating power produced by fusion reaction and outer input. In D-T reaction, one reaction creates an alpha particle which has $Q_\alpha = 3.5\,\mathrm{MeV}$ energy and a neutron which has $Q_n = 14.06\,\mathrm{MeV}$. Alpha particles heat up electrons and ions by Coulomb collisions, while neutrons have few interactions with plasma, so output power per unit volume is

$$P_\alpha = \frac{n^2}{4} < \sigma v > Q_\alpha, \tag{1.6}$$

assuming that the density ratio of Deuterium and Tritium is $n_D : n_T = 1:1$. Fusion reaction can continue without any input power, if $P_{loss} \leq P_\alpha$, i.e.

$$n \cdot \tau \geq \frac{12\kappa T}{< \sigma v > Q_\alpha}. \tag{1.7}$$

This is one of a fundamental indicator about product of density and confinement time. J. D. Lawson evaluated criterion for producing thermonuclear reactor, so called Lawson criterion [4], which postulates $n\tau \geq 1.5 \times 10^{20}$ m^{-3}sec. and $T \geq$10keV. Nuclear fusion reaction requires high temperature plasmas and long confinement time is also important for nuclear fusion power plant.

1.2 Magnetic Confinement

In magnetic field, charged particles are received Lorentz force, which is perpendicular to the magnetic field, and move helically around magnetic field line, so that magnetic field restricts the motion of charged particles and confines plasma. There are several plasma experimental devices, which have a concept of magnetic confinement, such as tokamak, sterallator, reversed field pinch, tandem mirror and internal coil. Tokamaks and sterallators are most progressed devices for plasma

confinement and nuclear fusion reactor. On the other hand, in this work, a dipole confinement which has magnetic field like a planet is treated. The configuration is produced by an internal coil device the Mini-RT. Internal coil devices and dipole confinement are developing for applying nuclear fusion reactor, and this configuration has the possibility of the exceedingly high beta plasma confinement by Alfvénic flow [5] [6]. Beta value is an important parameter for magnetic confinement plasma and is defined as the ratio of plasma pressure and magnetic pressure

$$\beta = \frac{\sum n_s \kappa T_s}{B^2/2\mu_0}, \tag{1.8}$$

where subscript 's' denotes the species. High beta means high density and high temperature plasmas are confined in relatively low magnetic field, so that the beta value is an important index of economy of nuclear fusion reactor. To realize compact and economic fusion reactor, high beta plasma studies have been carried out [7] [8] [9].

1.3 Plasma Heating

Plasma heating method is generally categorized as follows; ohmic heating, Neutral Beam Injection (NBI) heating and Radio Frequency (RF) heating. In particular, Electron Cyclotron Heating (ECH), which is a kind of RF heating, has engineering benefits; the Electron Cyclotron Wave (ECW) has competence to propagate in a vacuum and to be transmitted with high electric power density, and physical benefits; fundamental structure of energy absorption is revealed and can be predicted theoretically with ease and the ECW can affect local plasma heating and current drive. ECH is a practicable method for plasma heating and is organized in International Thermonuclear Experimental Reactor (ITER) [10]. However, since the ECW has the cutoff density, it is difficult to generate and heat the high density plasma with ECH. The cutoff density is determined by the strength of magnetic field, the frequency of microwaves, and etc, and waves in plasmas have several modes by interaction with charged particles. The Electron Bernstein Waves (EBWs)

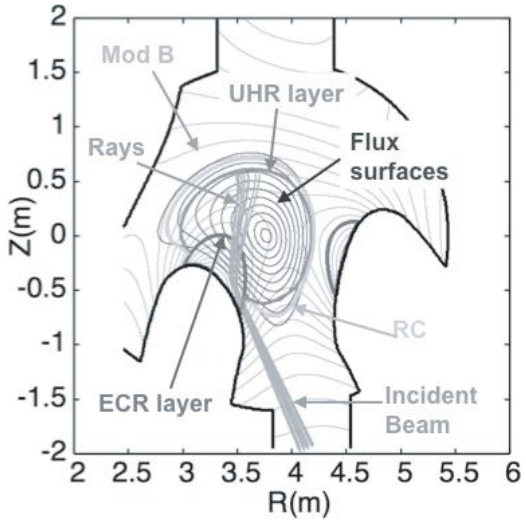

Figure 1.2: Schematic of the SX-mode launching in the LHD [16]

Contours of flux surfaces, the UHR layer, the ECR layer and the RC are plotted on the plane.

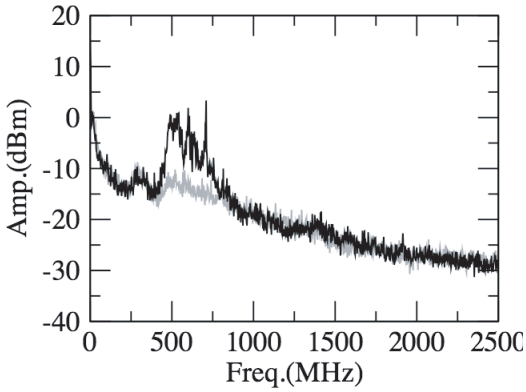

Figure 1.3: Frequency spectrum of a LH wave [16]

Black and grey shows the frequency spectrum during EC wave launching and the background level, respectively.

are electrostatic mode waves, which have no cutoff density and plural energy absorption layers. Therefore, EBW heating is expected to be one of the most promising methods for generating and heating high density plasmas and heating and current drive by EBWs are actively investigated [11] [12] [13] [14] [15]. As an example, the following is an EBW heating experimental result in the Large Helical Device [16]. H. Igami *et al.* launched the slow extraordinary mode from the lower port antenna in the LHD, and made the SX microwaves reach the Upper Hybrid Resonance (UHR) layer. Figure 1.2 shows a schematic of the ray trajectories of the incident beam in the LHD. The launched X mode microwaves can reach the center of the plasma through the region where the electron density and temperature are very low and the width of evanescent region lying the Right-handed Cutoff (RC) and the UHR is very thin. Figure 1.3 shows the frequency spectrum of a Lower Hybrid (LH) wave along with its harmonics range. This figure shows that the parametric decay wave in the LH wave frequency occurred because of the coupling process at the UHR that the SX-mode reaches, so that it suggests that the SX-mode reached

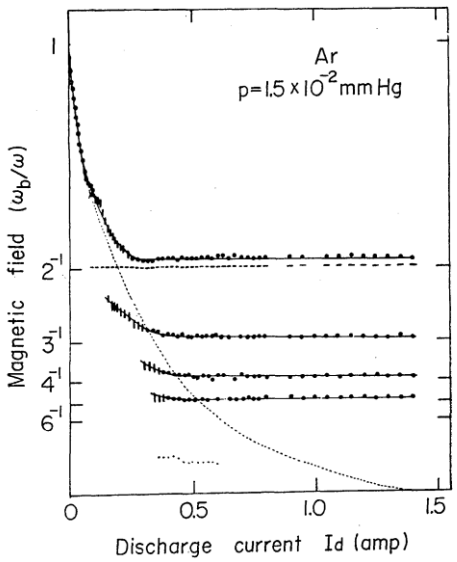

Figure 1.4: Harmonic structure of the dispersion relation [18].

the UHR layer and that the condition of the EBW excitation was fulfilled.

I. B. Bernstein has predicted the existence of the EBW as an electrostatic mode which propagates perpendicular to the external magnetic field with theoretical analysis of hot plasma [17]. K. Mitani *et al.* showed the harmonic structure of the dispersion relation by investigating the resonant radiation from a magnetoactive plasma for the extraordinary wave [18]. This is the first experimental verification of the EBW. They measured the microwave radiations from the positive column immersed in a magnetic field by means of X-band radiometer and observed that the radiation patterns exhibit the resonant peaks near the 2^{nd}, 3^{rd}, 4^{th} and 5^{th} cyclotron harmonics in addition to the frequency of the UHR. These observed radiations were interpreted as the EBW which leaked out from the thin column plasma and radiated with the waveguide mode. During much of the same period, F. W. Crawford *et al.* [19] and R. S. Harp [20] also measured the transmission and emission of the EBW in linear plasma devices. Later on, it began to study a new method to heat overdense plasmas with the EBW [21] [22], and demonstrated EBW heating and EBW emission in the W7 – AS stellarator [11]. In addition to overdense plasma heating, EBW is used for current drive and start-up assistance in Spherical torus [7] [14] [13].

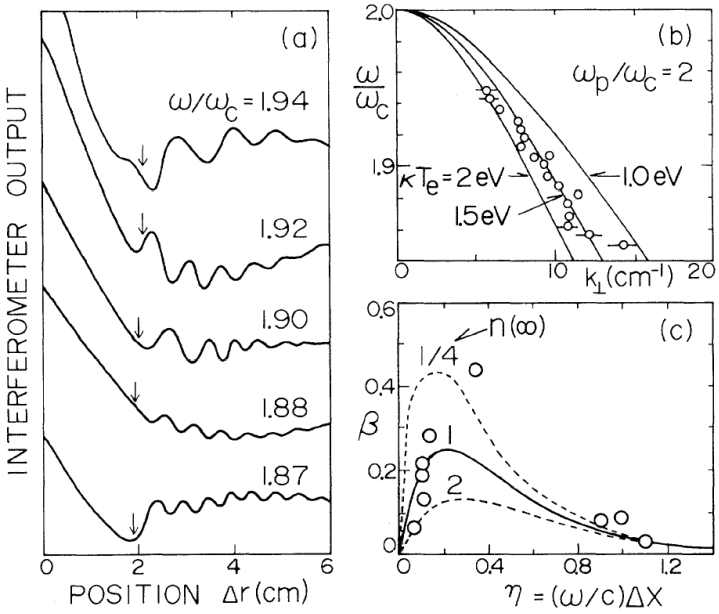

Figure 1.5: EBW measurement in a linear plasma device with a coax-fed wire antenna [24].

(a) Spatial waveforms by interferometer (arrows indicate the location of the UHR)

(b) Experimental and theoretical curves of the dispersion relation of EBW

(c) Mode conversion efficiency from X-mode into EBW

Actual proofs of EBWs have been carried out mainly with indirect measurements like as electron cyclotron emission measurement, and EBW heating and EBW current drive experiments are interested in their effects on the plasma. Inserting probes, however, enables the direct investigation of waves in the plasma, and a few actual proofs of EBW with direct measurement by probing antennas have been carried out. S. Gruber and G. Bekefi investigated longitudinal waves in a magnetically confined linear hot-cathode arc discharge 5 cm in diameter [23]. They showed a drastic change in wavelength was observed with increasing magnetic field strength. H. Sugai verified experimentally that short-wavelength waves excited around the upper hybrid resonance (UHR) were mode-converted EBWs in a pulsed discharge plasma with a cathode of 60 cm diameter [24]. Y. Y. Podoba *et al.* demonstrated mode conversion from O-mode to X-mode waves around a cutoff layer and a phase jump around the UHR on the WEGA stellarator [25]. They measured

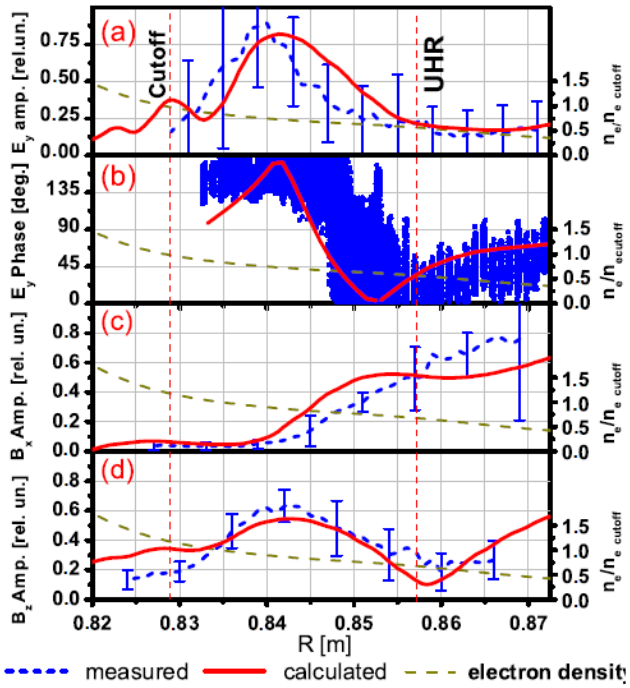

Figure 1.6: Radial profiles of electric and magnetic field components in the WEGA stellarator [25].

(a) – (d) show measured and calculated E_y (X-mode) amplitude, E_y phase, B_x (O-mode) and B_z (X-mode) wave components, respectively. The phase jump of ~ 180° near the UHR confirm the existence of the UHR layer in the device, and B_x decreases and B_y increase between the cutoff and the UHR indicates the mode conversion from O-mode to X-mode.

the amplitude and phase of electric and electromagnetic field with rf-probes and loop antennas, and showed several characteristics of the EBW via spatial profiles of amplitude. However, since they did not measured the wavelength of the microwaves and EBWs, comparisons theory and experiments in terms of dispersion relations cannot be distinguished.

1.4 Outline of This Research

This work is concerned with waves in dipole confinement plasma and an

experimental verification of Electron Bernstein Waves in the internal coil device Mini-RT is carried out. In fusion plasma experimental devices, most of Experimental verifications of EBWs have been fulfilled with indirect measurements, while detailed direct measurements of them are not necessarily complete. In order to research the mode conversion process of electromagnetic mode wave to the Electron Bernstein Waves, the propagation of waves in internal coil torus plasmas is investigated by direct measurement with several kinds of probes. Three conversion scenarios, details are described in Ch.2, are well known and the most suitable method depends on the plasma coordination. The aim of this work is to verify experimentally with all the three excitation methods of EBWs in the internal coil torus plasma.

The architecture of this thesis is the following. In chapter 2, basic physics of waves in plasma is described. Then, the experimental device, the Mini-RT is overviewed in chapter 3. A numerical analysis with ray tracing and with FDTD code is described in chapter 4. After that, in chapter 5, diagnostic microwave systems are described. Chapter 6 shows the experimental results, and they are discussed in chapter 7. Finally, the conclusion of this research is declared in chapter 8.

Chapter 2
Waves in Plasma

RF heating is a part of plasma heating methods and waves in plasma have several characteristics by interaction with charged particles. In this chapter, behaviors of waves in plasma are described, and the description is started with a simple approximate model and is expanded to more general plasma model.

2.1 Basic Equations

Waves in plasmas are described by Maxwell equations,

$$\nabla \cdot \boldsymbol{E} = \frac{\rho}{\epsilon_0} \tag{2.1}$$

$$\nabla \cdot \boldsymbol{B} = 0 \tag{2.2}$$

$$\nabla \times \boldsymbol{E} = -\frac{\partial \boldsymbol{B}}{\partial t} \tag{2.3}$$

$$\nabla \times \boldsymbol{B} = \frac{1}{c^2}\frac{\partial \boldsymbol{E}}{\partial t} + \mu_0 \boldsymbol{j}. \tag{2.4}$$

Charge density ρ and current density $\boldsymbol{j}$ which are made by charged particles in plasmas are determined by their distribution function,

$$\rho = \sum_s q_s \int d^3v\, f_s \tag{2.5}$$

$$\boldsymbol{j} = \sum_s q_s \int d^3v f_s \boldsymbol{v} \tag{2.6}$$

where f_s and q_s denote the distribution function and charge of "s" respectively and subscript s denotes ion's specie. The time evolution of the distribution function obeys the Vlasov equation [26],

$$\frac{\partial f_s}{\partial t} + \boldsymbol{v} \cdot \boldsymbol{\nabla}_{\boldsymbol{r}} f_s + \frac{q_s}{m_s}(\boldsymbol{E} + \boldsymbol{v} \times \boldsymbol{B}) \cdot \boldsymbol{\nabla}_{\boldsymbol{v}} f_s = 0, \tag{2.7}$$

where m_s denotes mass of s. Since the plasma is a dispersive medium, the conductivity, relationship between electric field and current density, is written as a tensor

$$\boldsymbol{j} = \sum_s \overleftrightarrow{\sigma_s} \cdot \boldsymbol{E}, \tag{2.8}$$

and the electric displacement vector $\boldsymbol{D}$ is defined as

$$\boldsymbol{D} \equiv \epsilon_0 \boldsymbol{E} + \boldsymbol{P}, \tag{2.9}$$

where $\boldsymbol{P}$ is a polarization vector, which is defined by induced current density

$$\boldsymbol{j} = \frac{\partial \boldsymbol{P}}{\partial t}. \tag{2.10}$$

By assuming perturbed values vary as $\exp[i(\boldsymbol{k} \cdot \boldsymbol{r} - \omega t)]$, the relationship between conductivity and dielectric tensor can be written as

$$\boldsymbol{D} = \overleftrightarrow{\epsilon} \cdot \boldsymbol{E} = \left(\epsilon_0 \overleftrightarrow{I} + \frac{i}{\omega} \sum_s \overleftrightarrow{\sigma_s}\right) \cdot \boldsymbol{E} \equiv \epsilon_0 \left(\overleftrightarrow{I} + \sum_s \overleftrightarrow{\chi_s}\right) \cdot \boldsymbol{E}, \tag{2.11}$$

where $\overleftrightarrow{\epsilon}, \overleftrightarrow{\chi}$ and $\overleftrightarrow{I}$ are the dielectric tensor, the susceptibility tensor and the unit tensor, respectively.

2.2 Waves in Cold Plasma

Cold plasma model assumes homogeneous plasma whose temperature is zero in equable magnetic field, i.e. electrons and ions rest in non disturbance state and Larmor radius is much shorter than wavelength.

2.2.1 Dispersion Relation of Cold Plasma Waves

In cold plasma approximation, Eqs. (2.5), (2.6) and (2.7) are simplified as follows;

$$\rho = \sum_s q_s n_s \tag{2.12}$$

$$\boldsymbol{j} = \sum_s n_s q_s \boldsymbol{u_s} \tag{2.13}$$

$$\frac{d\boldsymbol{u}_s}{dt} = \frac{q_s}{m_s}(\boldsymbol{E} + \boldsymbol{u_s} \times \boldsymbol{B}), \tag{2.14}$$

where n_s and $\boldsymbol{u_s}$ denote density and macroscopic average velocity of s respectively. Assuming the steady magnetic field $\boldsymbol{B_0} = B_0\hat{\boldsymbol{z}}$ and electric field $\boldsymbol{E_0} = 0$, we can get the dielectric tenser from Eqs. (2.8), (2.11), (2.13), (2.14);

$$\overleftrightarrow{\epsilon} = \epsilon_0 \begin{pmatrix} S & -iD & 0 \\ iD & S & 0 \\ 0 & 0 & P \end{pmatrix}. \tag{2.15}$$

The parameters S, D and P were introduced by H. T. Stix in 1962 [27]. They are defined as follows

$$S = \frac{1}{2}(R + L) = 1 - \sum_s \frac{\omega_{ps}^2}{\omega^2 - \Omega_s^2} \tag{2.16}$$

$$D = \frac{1}{2}(R - L) = \sum_s \frac{\Omega_s}{\omega} \frac{\omega_{ps}^2}{\omega^2 - \Omega_s^2} \tag{2.17}$$

$$P = 1 - \sum_s \frac{\omega_{ps}^2}{\omega^2} \tag{2.18}$$

$$R = 1 - \sum_s \frac{\omega_{ps}^2}{\omega(\omega + \Omega_s)} \tag{2.19}$$

$$L = 1 - \sum_s \frac{\omega_{ps}^2}{\omega(\omega - \Omega_s)}, \tag{2.20}$$

where plasma frequency ω_{ps} and cyclotron frequency Ω_s are defined as

$$\omega_{ps}^2 = \frac{n_s q_s^2}{\epsilon_0 m_s} \tag{2.21}$$

$$\Omega_s = \frac{q_s B_0}{m_s}. \tag{2.22}$$

The parameters, R (right), L (left), P (plasma), S (sum) and D (difference) are also referred to as "Stix parameters".

We are assuming that perturbed values vary as $\exp[i(\boldsymbol{k} \cdot \boldsymbol{r} - \omega t)]$, and Eqs. (2.3) and (2.4) are

$$i\boldsymbol{k} \times \boldsymbol{E} = i\omega \boldsymbol{B} \tag{2.23}$$

$$i\boldsymbol{k} \times \boldsymbol{B} = -i\omega\mu_0 \boldsymbol{D} \tag{2.24}$$

Dispersion relation can be obtained from dielectric tensor, by substituting Eqs. (2.11), (2.15), (2.23) into (2.24) then

$$\boldsymbol{k}\times\boldsymbol{k}\times\boldsymbol{E}+\left(\overleftrightarrow{I}+\sum_{s}\overleftrightarrow{\chi_s}\right)\cdot\boldsymbol{E}=0. \tag{2.25}$$

By introducing refractive index vector $\boldsymbol{N}$ and specific dielectric tensor $\overleftrightarrow{K}$ be as $\boldsymbol{N}=c\boldsymbol{k}/\omega$ and $\overleftrightarrow{K}=\overleftrightarrow{I}+\sum_s\overleftrightarrow{\chi_s}$, then (2.25) becomes

$$\boldsymbol{N}\times\boldsymbol{N}\times\boldsymbol{E}+\overleftrightarrow{K}\cdot\boldsymbol{E}=0. \tag{2.26}$$

Assuming that $\boldsymbol{N}$ is on the z-x plane and that θ is defined as the angle between wave number vector $\boldsymbol{k}$ and static magnetic field $\boldsymbol{B_0}$, i.e.

$$\boldsymbol{N}=\left(N_x,N_y,N_z\right)=(N\sin\theta\,,0,N\cos\theta), \tag{2.27}$$

Eq. (2.25) is written as follows

$$\begin{pmatrix}S-N^2\cos^2\theta & -iD & N^2\cos\theta\sin\theta\\ iD & S-N^2 & 0\\ N^2\cos\theta\sin\theta & 0 & P-N^2\sin^2\theta\end{pmatrix}\cdot\begin{pmatrix}E_x\\E_y\\E_z\end{pmatrix}\equiv\boldsymbol{\Lambda_c}\cdot\boldsymbol{E}=0. \tag{2.28}$$

Then determinant of $\boldsymbol{\Lambda_c}$ should be 0 to have nontrivial solutions of $\boldsymbol{E}$,

$$\det\boldsymbol{\Lambda_c}=AN^2-BN+C=0. \tag{2.29}$$

This is so called the dispersion relation of cold plasma, and the parameters A,B and C are

$$A=S\sin^2\theta+P\cos^2\theta \tag{2.30}$$

$$B=RL\sin^2\theta+PS(1+\cos^2\theta) \tag{2.31}$$

$$C=RLP, \tag{2.32}$$

respectively. There are two solutions of Eq. (2.29) involving imaginary number;

$$N^2=\frac{B\pm F}{2A}, \tag{2.33}$$

where F is

$$F^2=(RL-PA)^2\sin^4\theta+4P^2D^2\cos^2\theta. \tag{2.34}$$

2.2.2 Cutoff and Resonance

The solution N is determined by some plasma parameters. The point at $N=0$ is called the cutoff, where the wave is reflected and at $N=\infty$ is done the resonance, where absorption occurs, in particular.

For example, if propagation angle θ is equal to 0,

$$P=0,N^2=R,L. \tag{2.35}$$

The first solution $P = 0$ corresponds to the so called "plasma oscillations", where the charged particles oscillate for the parallel direction to the magnetic field around their equilibrium position. Since the plasma oscillations have no wave numbers, these oscillations cannot propagate in the plasma. The two other solutions $N^2 = R$ and $N^2 = L$ are dubbed as R- and L-wave, after their polarizations. The R (L)-wave is a clockwise (counterclockwise) circular polarized wave. Since the R (L)-wave has the same direction of rotation with electron (ion) cyclotron, the wave can be absorbed by the charged particles at the point of $R\ (L) = \infty$.

Then if θ is equal to $\pi/2$, the solutions of Eq. (2.27) become

$$N^2 = P, \frac{RL}{S}. \tag{2.36}$$

The first solution $N^2 = P$ is a mode whose direction of electric filed vector is parallel to $\boldsymbol{B_0}$ and is referred to as O-wave (Ordinary). This wave cannot be absorbed in this approximation and has a cutoff at the plasma frequency. On the other hand, the second solution $N^2 = RL/S$ is referred to as X-wave (eXtraordinary), which has either clockwise or counterclockwise elliptical polarization in the x-y plane. The cutoff occurs at $R = 0$ or $L = 0$ and the wave absorption does at $S = 0$ which is so called hybrid resonance. Assuming single ion plasma, there are two resonances, the Upper Hybrid Resonance (UHR) and the Lower Hybrid Resonance (LHR). They occur at

$$\omega_{UH}^2 = \omega_{pe}^2 + \Omega_e^2 \qquad \text{(UHR)}, \tag{2.37}$$

$$\frac{1}{\omega_{LH}^2} = \frac{1}{\Omega_i^2 + \omega_{pi}^2} + \frac{1}{|\Omega_i \Omega_e|} \qquad \text{(LHR)}. \tag{2.38}$$

2.3 Waves in Hot Plasma

2.3.1 Dielectric Tensor of Hot Plasma

In cold plasma, electrons and ions are regarded as motionless in the unperturbed state. In hot plasma, however, charged particles have a spiral motion

around the magnetic line even in the unperturbed state. To evaluate the time development of perturbed distribution function, Vlasov equation is integrated along the unperturbed orbits [28]. According to Ref. [29], assuming the isotropic non-drift maxwellian plasma, i.e. parallel and perpendicular temperature same value ($T_{\parallel s} = T_{\perp s} = T_s$) and there is no flow, the susceptibility tensor $\overleftrightarrow{\chi}$ is

$$\overleftrightarrow{\chi} = \begin{pmatrix} K_1 + \sin^2\psi K_0 & K_2 - \cos\psi K_0 & \cos\psi K_4 + \sin\psi K_5 \\ -K_2 - \cos\psi K_0 & K_1 + \cos^2\psi K_0 & \sin\psi K_4 - \cos\psi K_5 \\ \cos\psi K_4 - \sin\psi K_5 & \sin\psi K_4 + \cos\psi K_5 & K_3 \end{pmatrix}, \tag{2.39}$$

where the wave number vector $\boldsymbol{k} = (k_\perp \cos\psi, k_\perp \sin\psi, k_z)$. The parameters K_0-K_5 are defined as follows;

$$K_0 = 2\sum_s \frac{\omega_{ps}^2 e^{-\lambda_s}}{\omega k_z v_{sT}} \sum_{l=-\infty}^{\infty} \lambda_s \big(I_l(\lambda_s) - I'_l(\lambda_s)\big) Z(\zeta_{ls}) \tag{2.31}$$

$$K_1 = \sum_s \frac{\omega_{ps}^2 e^{-\lambda_s}}{\omega k_z v_{sT}} \sum_{l=-\infty}^{\infty} \frac{l^2 I_l(\lambda_s)}{\lambda_s} Z(\zeta_{ls}) \tag{2.32}$$

$$K_2 = i\sum_s \frac{\epsilon_s \omega_{ps}^2 e^{-\lambda_s}}{\omega k_z v_{sT}} \sum_{l=-\infty}^{\infty} l\big(I_l(\lambda_s) - I'_l(\lambda_s)\big) Z(\zeta_{ls}) \tag{2.33}$$

$$K_3 = -\sum_s \frac{\omega_{ps}^2 e^{-\lambda_s}}{\omega k_z v_{sT}} \sum_{l=-\infty}^{\infty} I_l(\lambda_s) \zeta_{ls} Z'(\zeta_{ls}) \tag{2.34}$$

$$K_4 = \sum_s \frac{k_\perp \omega_{ps}^2 e^{-\lambda_s}}{2\omega k_z \Omega_s} \sum_{l=-\infty}^{\infty} \frac{l I_l(\lambda_s)}{\lambda_s} Z'(\zeta_{sl}) \tag{2.35}$$

$$K_5 = i\sum_s \frac{\epsilon_s k_\perp \omega_{ps}^2 e^{-\lambda_s}}{2\omega k_z \Omega_s} \sum_{l=-\infty}^{\infty} \big(I_l(\lambda_s) - I'_l(\lambda_s)\big) Z'(\zeta_{ls}), \tag{2.36}$$

where $v_{sT} = \sqrt{2\kappa T_s/m_s}$, $\lambda_s = (1/2)k_\perp^2 \rho_s^2$, $\rho_s = v_{sT}/\Omega_s$, $\zeta_{ls} = (\omega + l\Omega_s)/k_z v_{sT}$, $\epsilon_s = q_s/|q_s|$, $I_l(\lambda_s)$ is the l th modified Bessel function of the first kind and $Z(\zeta_{ls})$ is the plasma dispersion function, respectively. In addition, the superscript " ' " means total differentiation of the function.

2.3.2 Electron Bernstein wave

The Electron Bernstein Wave (EBW) is an electrostatic mode, which is longitudinal polarized, and propagates nearly perpendicular to the magnetic field. The electron cyclotron motion plays an important role in the propagation of the EBW and its wavelength is the order of the Larmor radius. Figure 2.1 shows the

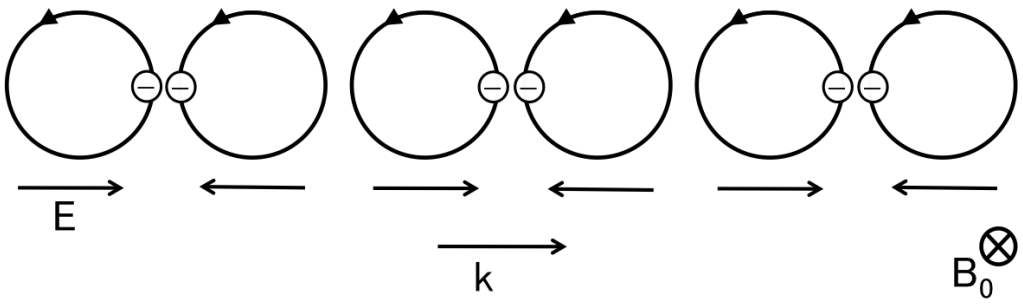

Figure 2.1: Schematic description of the EBW propagation

The corrective electron cyclotron motions create periodic charge accumulation. schematic description of the EBW propagation. Some characteristics of the EBW are found in its dispersion relation with electrostatic approximation. In this approximation, electric field is written with scalar potential ϕ, i.e. $\boldsymbol{E} = -\nabla\phi$. By substituting this expression into $\nabla \cdot \boldsymbol{D} = 0$, we obtain the following

$$\begin{aligned} &\boldsymbol{k} \cdot \overleftrightarrow{\epsilon} \cdot \boldsymbol{k} \\ &= k_x^2\epsilon_{\mathrm{xx}} + k_y^2\epsilon_{yy} + k_z^2\epsilon_{zz} + k_x k_y\left(\epsilon_{xy} + \epsilon_{yx}\right) + k_x k_z(\epsilon_{xz} + \epsilon_{zx}) \\ &\qquad + k_y k_z\left(\epsilon_{yz} + \epsilon_{zy}\right) = 0. \end{aligned} \tag{2.37}$$

By setting the axis so as to $k_x = k_\perp, k_y = 0, k_z = k_\parallel$, Eq. (2.37) is reduced to

$$k_\perp^2\epsilon_{xx} + 2k_\perp k_\parallel\epsilon_{xz} + k_\parallel^2\epsilon_{zz} = 0. \tag{2.38}$$

Ignoring the contributions of ions for simplification, the elements of dielectric tensor in Eq. (3.38) is written as follows

$$\epsilon_{xx} = 1 + \frac{\omega_{pe}^2 e^{-\lambda}}{\omega k_\parallel v_{th}} \sum_{l=-\infty}^{\infty} \frac{l^2 I_l(\lambda)}{\lambda} Z(\zeta_l) \tag{2.39}$$

$$\epsilon_{xz} = \frac{k_\perp \omega_{pe}^2 e^{-\lambda}}{2\omega k_\parallel v_{th}} \sum_{l=-\infty}^{\infty} \frac{l I_l(\lambda)}{\lambda} Z'(\zeta_l) \tag{2.40}$$

$$\epsilon_{zz} = 1 - \frac{\omega_{pe}^2 e^{-\lambda}}{\omega k_\parallel v_{th}} \sum_{l=-\infty}^{\infty} I_l(\lambda)\zeta_l Z'(\zeta_l). \tag{2.41}$$

By substituting Eqs. (2.39) – (2.41) into (2.38) and using a Bessel identity, the dispersion relation of the EBW is obtained;

$$1 + 2\left(\frac{\omega_{pe}^2}{\left(k_\parallel^2 + k_\perp^2\right)v_{th}^2}\right)\left[1 + \frac{\omega}{k_\parallel v_{th}} \sum_{l=-\infty}^{\infty} Z(\zeta_l) e^{-\lambda} I_l(\lambda)\right] = 0. \tag{2.42}$$

Some characteristics such as resonance and cutoff can be shown by asymptotic expansion of the plasma dispersion function and the modified Bessel function as a limiting case of the wave number vector. In the case of perpendicular

propagation, the parallel component of the wave number vector $k_{\parallel} \to 0$, Eq. (2.38) is reduced to

$$\epsilon_{xx} = 0. \tag{2.43}$$

In addition, in the case of $\zeta_l > 1$, where the parameters are not too close to the Electron Cyclotron Resonance (ECR) harmonics, the plasma dispersion function Z can be expanded as follows;

$$Z(\zeta_l) = -\frac{1}{\zeta_l} - \frac{1}{2\zeta_l^3} - \cdots. \tag{2.44}$$

Then, the dispersion relation of the EBW is

$$1 - \frac{2\omega_{pe}^2 e^{-\lambda}}{\Omega_e^2 \lambda} \sum_{l=1}^{\infty} \frac{l^2 I_l(\lambda)}{q^2 - l^2} = 0, \tag{2.45}$$

where $q \equiv \omega / \Omega_e$.

Considering the case of cutoff, $k_{\perp}$ goes to be 0, and for small variable λ the product of the modified Bessel function and exponential function can be expanded by asymptotic form with respect to λ [28] [30]

$$e^{-\lambda} I_n(\lambda) = \frac{1}{n!}\left(\frac{\lambda}{2}\right)^n \left[1 - \lambda + \left(\frac{\lambda}{2}\right)^2 \left(2 + \frac{1}{n+1}\right) + \cdots\right]. \tag{2.46}$$

Therefore, the dispersion relation near the cutoff can be expressed as

$$1 - \frac{\omega_{pe}^2}{\Omega_e^2}\left[\frac{1}{q^2 - 1^2} + \frac{1 \cdot 3\lambda}{(q^2 - 1^2)(q^2 - 2^2)} + \frac{1 \cdot 3 \cdot 5\lambda^2}{(q^2 - 1^2)(q^2 - 2^2)(q^2 - 3^2)} + \cdots\right] = 0. \tag{2.47}$$

The condition of cutoff obtained from Eq. (2.47) is

$$\omega = \omega_{UH} \tag{2.48}$$

$$\omega = n|\Omega_e| \quad n = 2,3, \ldots . \tag{2.49}$$

On the other hand, in the case of resonance $k_{\perp}$ goes to be ∞, and for large λ

$$e^{-\lambda} I_n(\lambda) = \frac{1}{(2\pi\lambda)^{1/2}}\left[1 - \frac{4n^2 - 1^2}{1!\,8\lambda} + \frac{(4n^2 - 1^2)(4n^2 - 3^2)}{2!\,(8\lambda)^2} - \cdots\right]. \tag{2.50}$$

Substituting Eq. (2.50) into (2.45),

$$1 - \frac{2\omega_{pe}^2}{\sqrt{2\pi}\Omega_e^2 \lambda^{3/2}} \sum_{l=1}^{\infty} \frac{l^2}{q^2 - l^2}\left[1 - \frac{4l^2 - 1^2}{1!\,8\lambda} + \cdots\right] = 0. \tag{2.51}$$

Thus, the condition of resonance is

$$\omega = n|\Omega_e| \quad n = 1,2, \ldots . \tag{2.52}$$

Therefore, cutoff and resonance occur at any harmonic ECR layers, and

only exceptional instance is the cutoff at the UHR layer. The validity of electrostatic approximation is vanished and the EBW has a marginal electromagnetic component near the cutoff region. On the other hand, the resonance of the X mode occurs at the UHR layer, where the refractive index of the X waves becomes large, the wavelength of them becomes much shorter and longitudinal electric filed dominates. Therefore, the X waves and the EBWs merge and mode conversion occurs at the UHR layer. In order to excite EBWs and to heat plasma with them, X waves reach the UHR layer. The dispersion relation of the EBWs as the solution of Eq. (2.43) is shown in Fig. 2.2. The parameter in this figure is normalized electron density ω_{pe}/Ω_e. In addition to the condition of cutoff and resonance, dispersion relation curve gives the characteristics of the group velocity. Since the group velocity $\partial\omega/\partial k$

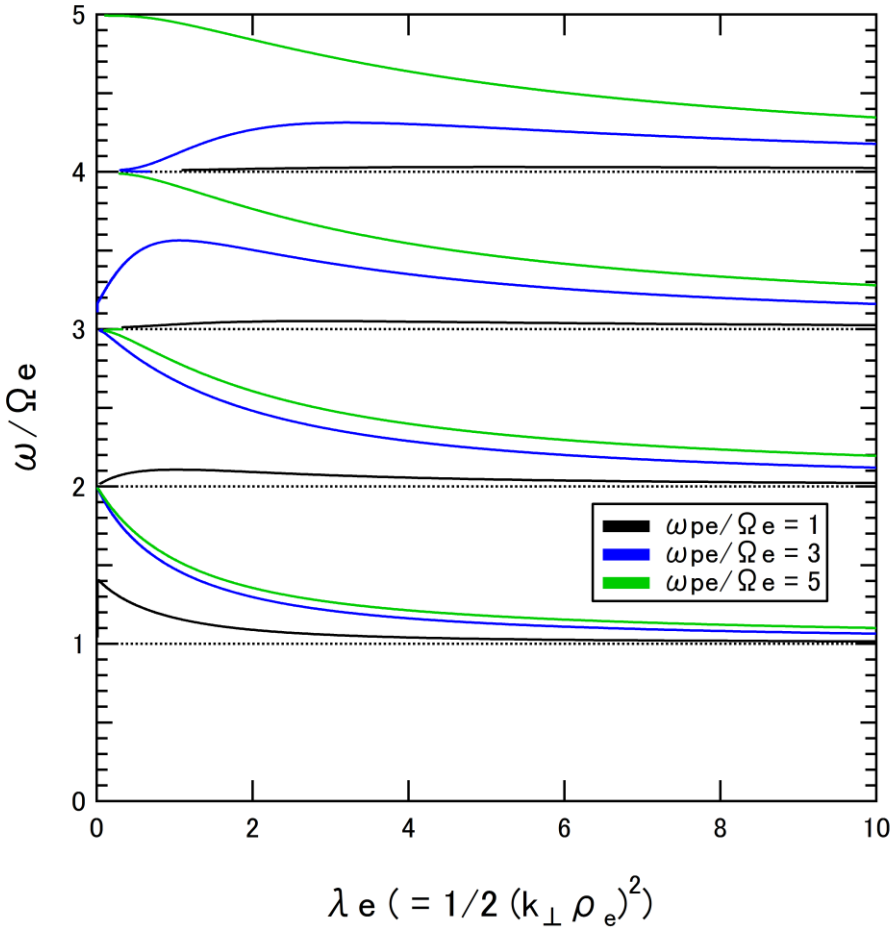

Figure 2.2: Dispersion relation of the EBW for perpendicular propagation at different values of parameter ω_{pe}/Ω_e

appears as the slope of a tangent, one can find the EBWs are backward wave except for the region near the cutoff.

2.4 Excitation of EBW

As already mentioned, since the EBW cannot propagate in vacuum, it is necessary to convert wave from electromagnetic mode into electrostatic mode in the plasma. This mode conversion requires an access to the UHR of the X waves. Three excitation scenarios of the EBWs are well known, i.e.

1) Perpendicular injection of X waves from high field side (SX-B conversion),
2) Perpendicular injection of X waves from low field side (FX-SX-B conversion),
3) Oblique injection of O waves from low field side (O-X-B conversion).

In this section, each schemes of excitation are described with the dispersion relation and some schematic wave trajectories.

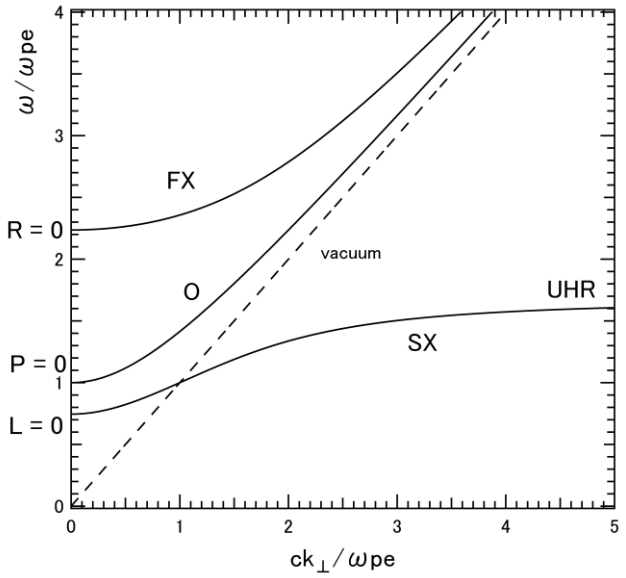

Figure 2.3: The dispersion relation of perpendicular propagation in the cold plasma
The ratio between the frequency of incident wave and electron cyclotron frequency is fixed as $\omega/\Omega_e = 1.25$.

2.4.1 SX-B Conversion

The cold plasma dispersion relation for perpendicular propagation mode is shown in Fig. 2.3. This figure shows O mode, Fast X (FX) mode and Sow X (SX) mode, and SX has a branch connecting the UHR. Thus, if the SX waves are injected into the plasma, they can be converted into the EBW. The CMA (Clemmow-Mullaly-Allis) diagram [31], which is shown in Fig. 2.4 [32], describes properties of the

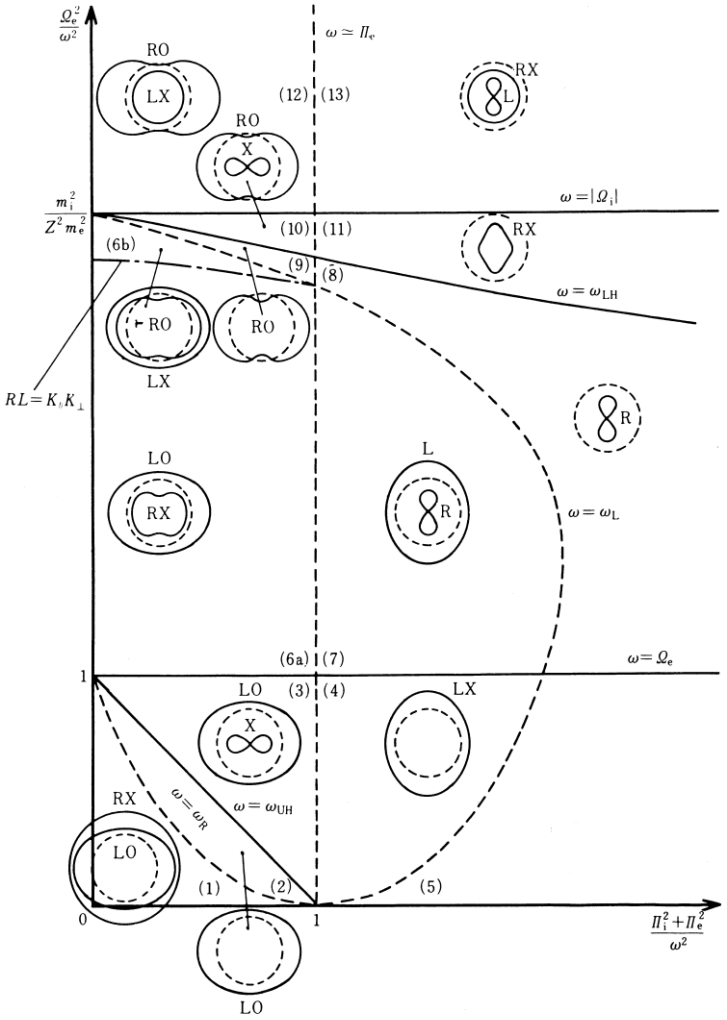

Figure 2.4: CMA diagram

This figure is quotation from Ref. [32].

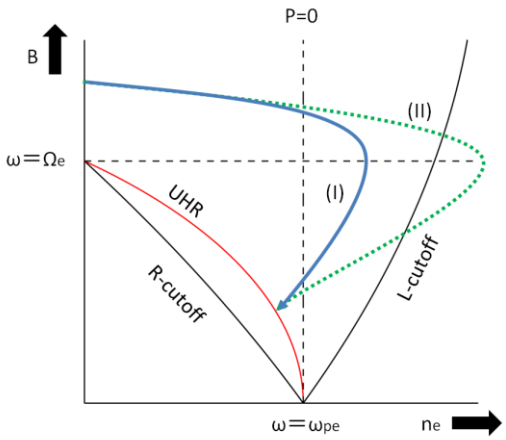

(a)SX-B conversion

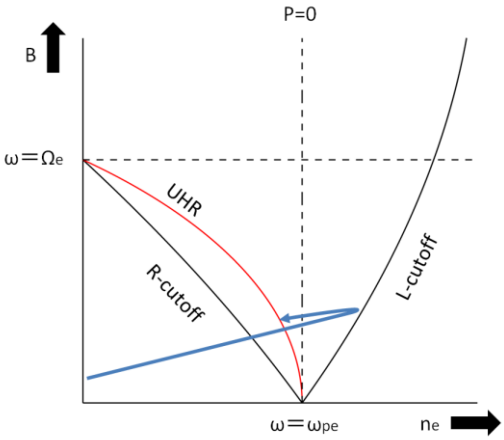

(b) FX-SX-B conversion

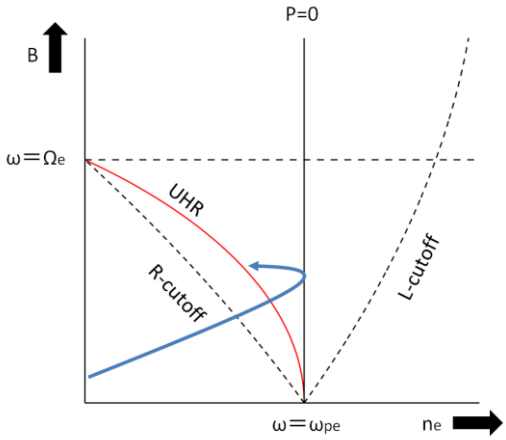

(c) O-X-B conversion

Figure 2.5: Wave trajectories on the CMA diagram
The UHR layers are drown as red lines in the diagram and blue lines show the proper trajectories for the EBW excitation in each scenario.

waves in a very intuitive way. In this diagram, horizontal axis corresponds to the square of a plasma frequency, which is proportional to the density, normalized by frequency of the incident wave, and vertical does to the electron cyclotron frequency, which is proportional to the strength of the magnetic field, normalized similarly. For example, if the wave injected from outside of the plasma, the initial position of the wave on the CMA diagram is a spot on the vertical axis. Therefore, to inject SX wave from the outside of the plasma, the initial position needs to be on $|\Omega_e|/\omega > 1$ region, and this condition corresponds to injection from high field side. Figure 2.5 (a)-(I), the blue line shows the schematic trajectory on the CMA diagram of SX-B conversion. Launched SX wave propagates from high field side to low field side and access the UHR directly. In this scenario, injected wave can reach the UHR without

passing the evanescent region.

The SX-B conversion is a straightforward scheme of an access to the UHR of the X wave. However, the plasma density has to be limited in order that wave trajectory on the SX-B conversion would not cross the cutoff line in the diagram. In Fig.2.5 (a)-(II), the dashed green line, the wave trajectory cross the L-cutoff line, so that the wave reflects at the cutoff and cannot access to the UHR layer. In addition, the SX-B conversion has some technical difficulties, because higher magnetic field side is located on the center of vacuum vessel in many torus plasma experimental devices. The internal coil device Mini-RT, which is treated in this research, is no exception, too. Thus in the SX-B scenario, wave launcher system should be in the center of the vacuum vessel where some complicated mechanisms exist. The detail of excitation system and antennas for SX-B conversion in the Mini-RT is described in Chapter 5.

2.4.2 FX-SX-B Conversion

Next, the perpendicular injection of the X wave from low field side, FX-SX-B conversion is mentioned. This conversion scenario is a method that makes the incident FX wave tunnel by reducing the thickness of the evanescent region between R-cutoff and the UHR. Figure 2.5 (b) shows FX-SX-B conversion trajectory on the diagram. FX wave is injected from low field side to high field side and propagate to the R-cutoff line, and then, if the width of evanescent region is much smaller than the incident wavelength, the tunneling of the FX wave occurs. The incident FX wave is converted into the SX wave and the wave reaches the L-cutoff and the UHR. The reflected SX wave at L-cutoff also accesses to the UHR. After that, the EBW is excited as well as the SX-B conversion. The thickness of the evanescent region between the R-cutoff and the UHR depends on the density gradient and magnetic field gradient. The steeper the gradient of density and magnetic field is, the thinner the evanescent region becomes. K.G. Budden investigated mode conversion efficiency by evaluating the tunneling and reflecting wave with the distance of the evanescent region normalized by the wavelength in

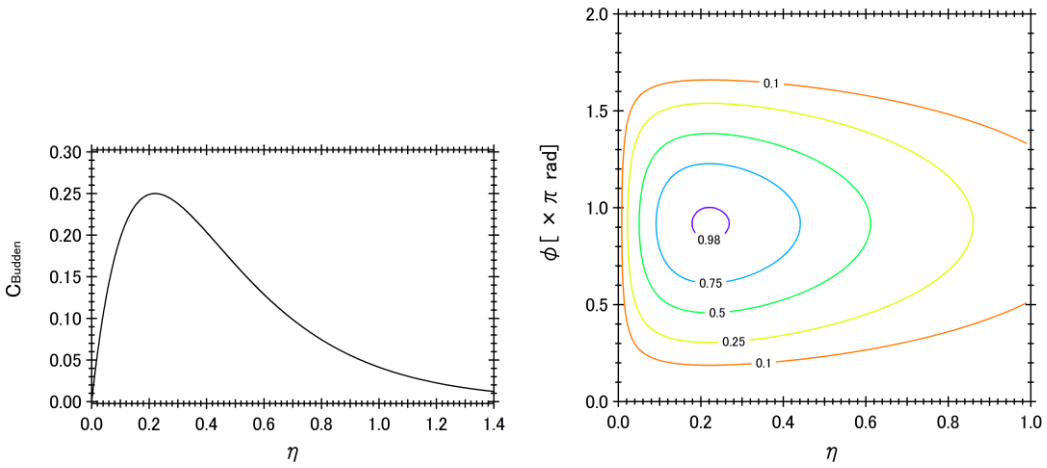

(a) Budden's model (b)Ram's model

Figure 2.6: Mode conversion efficiency as a function of η

(b) shows contours of constant conversion efficiency as a function of η and ϕ

vacuum [33]. He constructed a mode of refractive index at the vicinity of the UHR, and analytical solution is obtained. It is assumed that the incident wave propagates along the x direction and uniformity in the y direction. Then, let the tunneling parameter η introduced as follows

$$\eta = k_0 \Delta x, \tag{2.53}$$

where k_0 is a wave number vector at infinity and Δx is the distance between R-cutoff and the UHR. The reflection coefficient R was evaluated by the ratio of the amplitude of the incident wave and that of the reflected wave.

$$|R| = 1 - e^{-\pi\eta} \tag{2.54}$$

Similarly, the transmission coefficient T was obtained from the ratio of the amplitude of the incident wave and that of the transmission wave.

$$|T| = e^{-\pi\eta/2} \tag{2.55}$$

Then, the conversion efficiency $\mathrm{C_{Budden}}$ is written as

$$C_{Budden} = 1 - |R^2| - |T^2| = e^{-\pi\eta}(1 - e^{-\pi\eta}). \tag{2.56}$$

Therefore, the maximum mode conversion efficiency with the Budden's model is 1/4 at $\eta = (\ln 2)/\pi \approx 0.22$.

A. K. Ram constructed a more detailed model about the mode conversion efficiency [34]. His model contains the influence of the reflected wave at L-cutoff also [35]. In this model, the mode conversion efficiency is obtained as follows

$$C_{Ram} = 4\cos^2\left(\frac{\phi}{2} + \theta\right) C_{Budden}, \tag{2.57}$$

whre θ is the phase of $\Gamma(-i\eta/2)$ and ϕ is the phase difference between the SX wave propagating toward the L-cutoff and the reflected component propagating toward the UHR. The tunneling parameter η is estimated by using the gradient scale length of the plasma density and magnetic field.

$$\eta = \frac{\Omega_e L_n}{c} \frac{\alpha}{\sqrt{\alpha^2 + 2(L_n/L_B)}} \left(\frac{\sqrt{1+\alpha^2} - 1}{\alpha^2 + (L_n/L_B)\sqrt{1+\alpha^2}} \right)^{1/2}, \tag{2.58}$$

where

$$\alpha \equiv \left[\frac{\omega_{pe}}{\Omega_e}\right]_{UHR} \tag{2.59}$$

$$L_n \equiv \left[\frac{n}{|dn/dx|}\right]_{UHR} \tag{2.60}$$

$$L_B \equiv \left[\frac{B}{|dB/dx|}\right]_{UHR}, \tag{2.61}$$

respectively.

2.4.3. O-X-B Conversion

The incident wave trajectory of O-X-B conversion is described in Fig.2.5 (c). As shown in Fig.2.3, the branch of O wave and SX wave separated off between P-cutoff and L-cutoff in perpendicular propagation mode. However, if the incident wave has a parallel propagation component, the distance of evanescent region becomes thinner. From Eq. (2.29) we can obtain the perpendicular refractive index which includes parallel component as a parameter, i.e.

$$N_\perp^2 = \frac{J \pm \sqrt{J^2 - 4SK}}{2S} - N_\parallel^2, \tag{2.62}$$

where

$$J = SP + RL + SN_\parallel^2 - PN_\parallel^2 \tag{2.63}$$

$$K = RL\left(P + N_\parallel^2\right) - SPN_\parallel^2. \tag{2.64}$$

Figure 2.7 shows the perpendicular dispersion relation in the case of three constant

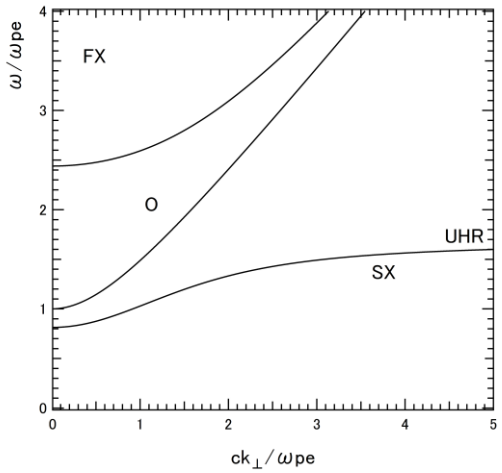

(a) $0 < N_{\parallel} < N_{\parallel opt}$

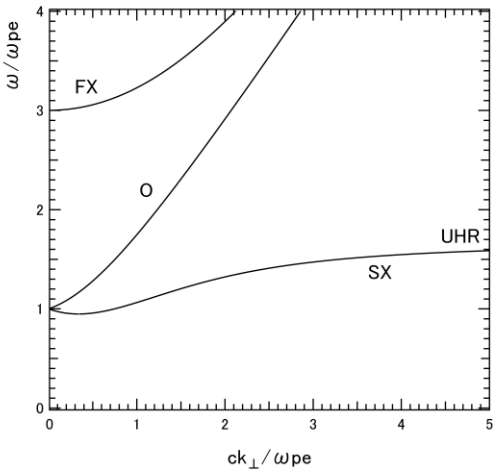

(b) $N_{\parallel} = N_{\parallel opt}$

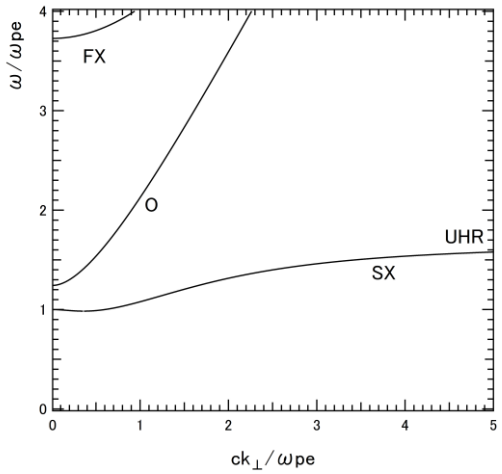

(c) $N_{\parallel} > N_{\parallel opt}$

Figure 2.7: Dispersion relations of the perpendicular component

The case of (b) shows the connection of the branch, while (a) and (c) the branch of O wave and that of X wave are displaced between the cutoffs.

values of parallel refractive index. The evanescent region becomes thinner with increasing the parallel component (Fig. 2.7 (a)), and the branch of O wave and that of SX wave connects when the parallel refractive index becomes a certain appropriate value (Fig. 2.7 (b)). The additional parallel component separates the branch of O and X waves again (Fig. 2.7 (c)). Therefore in the case of optimal parallel component, injected O wave is converted into SX wave and the SX wave is similarly done into the EBW. This optimal value of parallel component is obtained, by assuming the refractive index of the X mode and that of the O mode have the same value at the P-cutoff. Thus

$$N_{\parallel opt}^2 = L \tag{2.65}$$

Assuming that the wave propagation along the magnetic field varies little in its

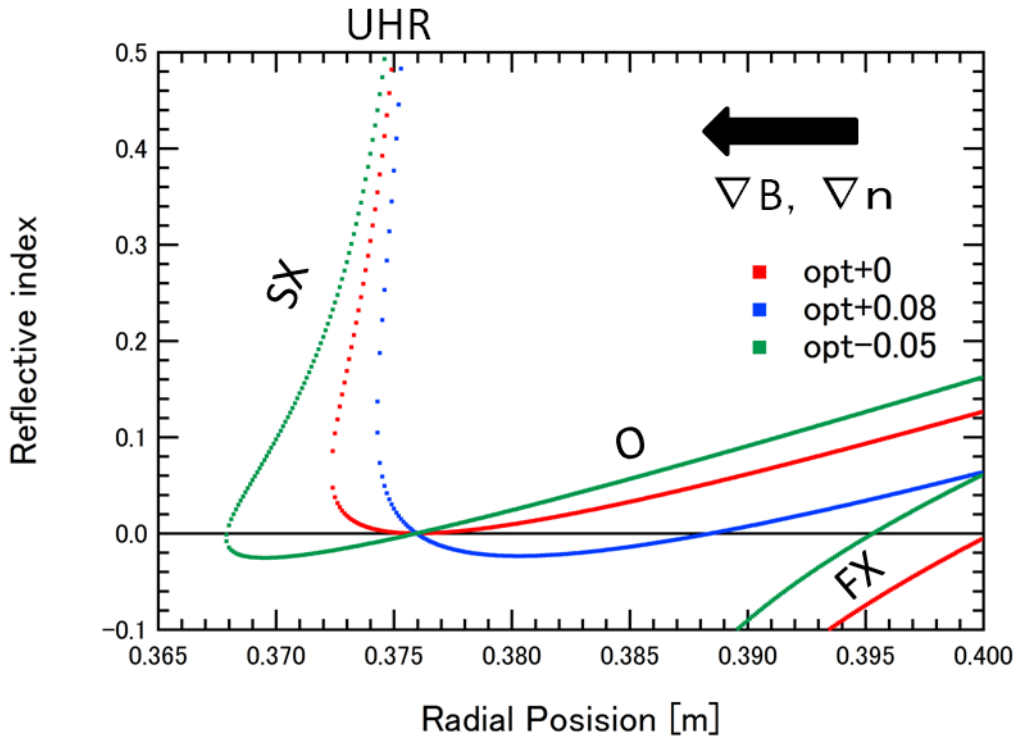

Figure 2.8: Perpendicular refractive index profile

The O wave is injected form right-hand side, which is low density and low magnetic field side. The plasma parameters are assumed as typical parameters in the Mimi-RT. The optimal injection condition, the red line in this figure, only has no evanescent region.

parallel component of the wave number vector $k_{\parallel}$, the optimum injection angle of the O wave to the plasma is obtained as follows;

$$\theta_{opt} = \cos^{-1}\sqrt{\frac{\Omega_e}{\omega + \Omega_e}}. \tag{2.66}$$

Figure 2.8 shows the refractive index profiles of O wave injection with typical parameters in the Mini-RT for optimal and slightly non-optimal oblique injection. To perfectly convert the injected O wave into the SX wave, the injection angle leaves no margin, but waves can also tunnel through the evanescent region with reflection and dumping. The conversion efficiency of O-X conversion was calculated with several model of wave propagation [36] [21] [37]. F. R. Hansen showed the Mjølhus's formula [38] to be the best approximation to the exact result of conversion efficiency

in a numerical study [39]. The formula is

$$T = \exp\left\{-\pi k_0 L_n \left(\frac{\Omega_e}{2\omega}\right)^{1/2} \left[2\left(1+\frac{\Omega_e}{\omega}\right)\left(N_z^2 - N_{zopt}^2\right)^2 + N_y^2\right]\right\}. \tag{2.67}$$

We are assuming that $N_z = N_\parallel$ and $N_y = 0$, so that the conversion efficiency can be described as normal distribution whose median becomes $N_{\parallel opt}$. Then,

$$T = \exp\left\{-\pi k_0 L_n \left(\frac{\Omega_e}{2\omega}\right)^{1/2} \left[2\left(1+\frac{\Omega_e}{\omega}\right)\left(N_\parallel^2 - N_{\parallel opt}^2\right)^2\right]\right\}. \tag{2.68}$$

Since the variance of this normal distribution is proportional to $1/k_0 L_n$, a small $k_0 L_n$, which means low frequency of the incident wave and steep gradient of the density profile, gives high conversion efficiency in broad range of $N_\parallel$. Here note that this conversion efficiency is only applicable in the O-X conversion. The SX wave converted from incident O wave propagates toward the UHR and couples to the EBW. However, if the evanescent region between the UHR and R-cutoff is adequately thin, this case is corresponds to small $k_0 L_n$, the tunneling incident occurs and the FX wave propagates toward the outer region. This is one reason why the SX-FX-B conversion and O-X-B conversion don't go together for the same plasma. Thus, high efficiency of the total O-X-B conversion requires both large $k_0 L_n$ and accurate injection.

Chapter 3
The Internal Coil Device Mini-RT

3.1 The Mini-RT Device

The Jupiter is a planet which has the magnetosphere. Plasmas which are mainly supplied by the Jovian satellite such as the Jupiter I, Io, are confined in the magnetosphere [40]. The rotary motion of them excels in a large domain within the range of the magnetism. Relaxation plays an important role in plasma dynamics. S. M. Mahajan and Z. Yoshida have developed a relaxation state based on two-fluid plasma theory [5]. To explore the relaxation phenomena, torus devices with a superconductor coil called Superconductor-Ring Trap (S-RT) was constructed [41]

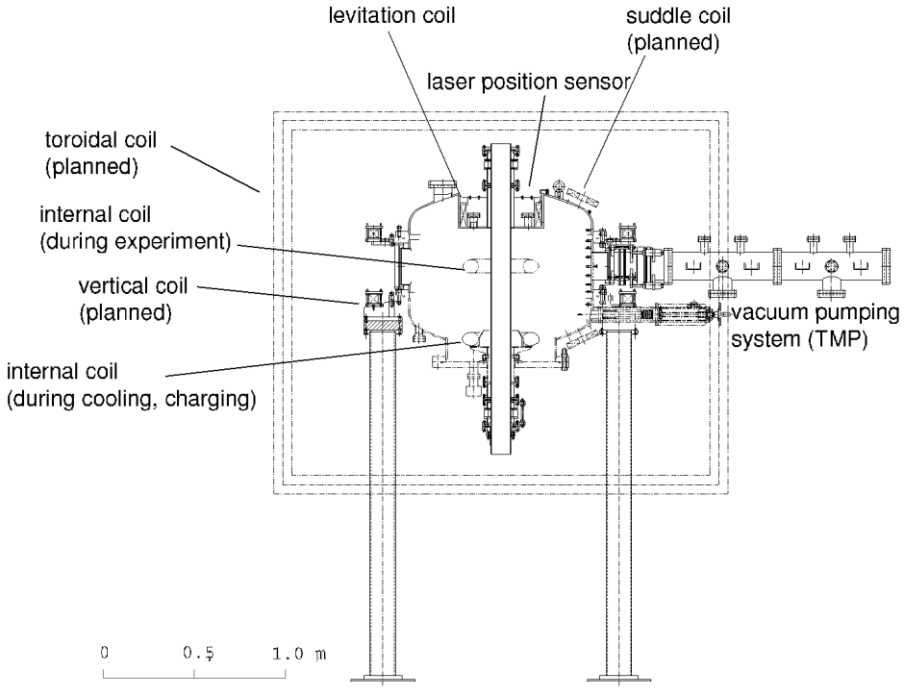

Figure 3.1: Schematic cross section of the Mini-RT device

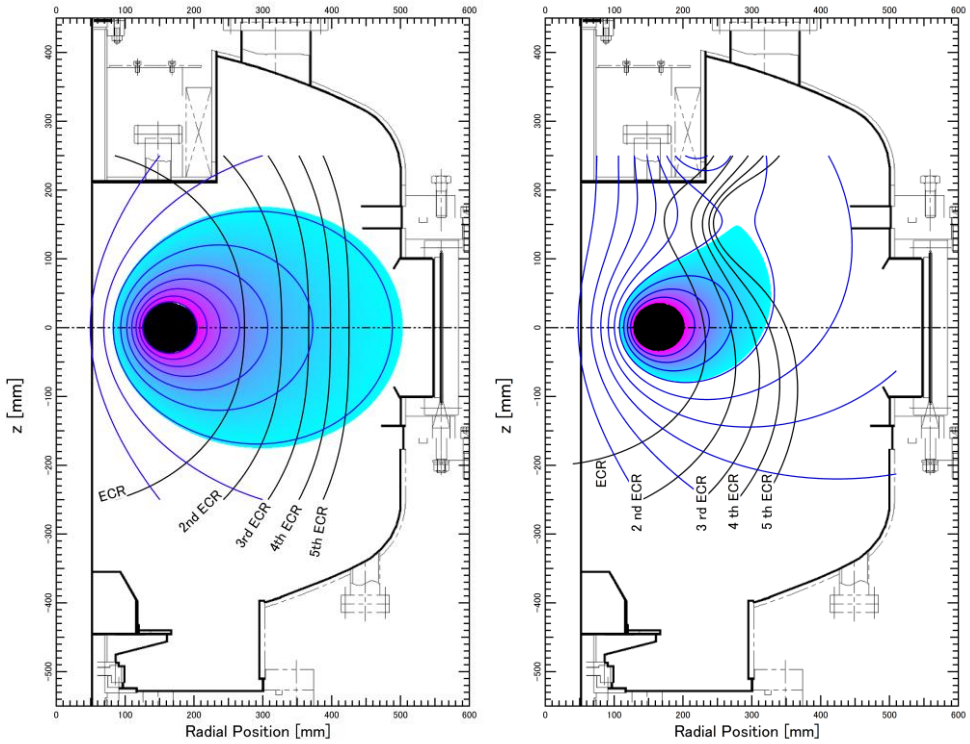

Figure 3.2: Configurations of the device

(a) simple dipole configuration (b) regular configuration

[42].

3.1.1 Overview

Figure 3.1 shows schematic view of the cross section of the Mini-RT device. The diameter of the vacuum vessel is 1.0 m, and its height is 0.7 m, respectively. The device has two coils; one is an internal coil constructed with a high temperature superconductor (HTS) and the other is levitation coil done with copper. Magnetic configurations are determined by magnetomotive force of these two coils. In other words, one can change the plasma confinement region easily with applying levitation coil current. Figure 3.2 shows two types of configuration. In the case of (a), with no levitation coil current, the configuration becomes simple dipole configuration, where confinement region of plasmas is limited by vacuum vessel

wall, on the other hand, in the case of (b), with applying levitation coil current, plasmas are confined in the last closed magnetic flux surface.

3.1.2 Coils in the Device

The internal coil in the Mini-RT device is cooled by helium gas with two GM refrigerators and is directly charged with persistent current. Figure 3.3 shows a

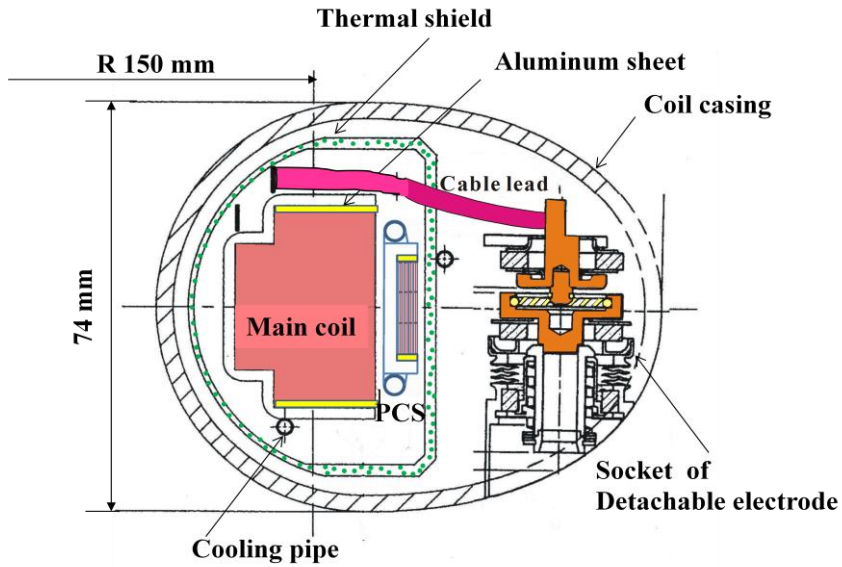

Figure 3.3: Schematic cross section of internal coil

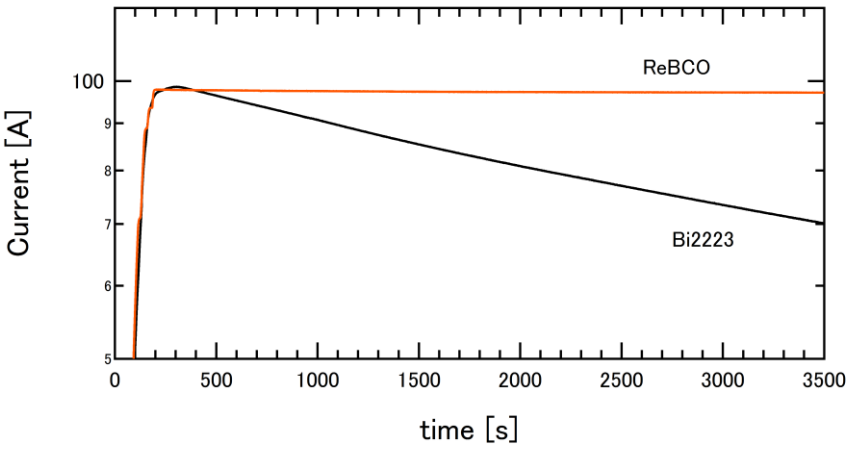

Figure 3.4: Comparison of current decay between Bi2223 and REBCO

cross section of the coil. The internal coil had been wound with BSCCO tapes and was replaced with the new one wound with the REBCO tapes [43]. Table 3.1 shows a comparison between the old and new internal coil [44]. Replacing the HTS tape results in extension of time constant of current decay. A comparison between them is shown in Fig. 3.4.

Table 3.1: Specifications of the main coil wound with the BSCCO and REBCO tape

	BSCCO coil	REBCO coil
Fabrication year	2003	2013
Major radius	150 mm	149.3 mm
Minor radius	16.15 mm	16.04 mm
Total coil current	50.0 kA-turns	55.2 kA-turns
Vendor	Sumitomo	Fujikura
Cross section of a tape Width Thickness	 4.4 mm 0.39 mm	 4.36 mm 0.272 – 0.281 mm
Stabilizer	Silver ratio = 1.57	Copper laminate 0.1 mm
Critical current (77K)	~ 100 A	216 – 223 A
Critical temperature	~ 113 K	92 K
Operation current	116.82 A	100 A
Current density	64.95 A/mm^2	68.30 A/mm^2
Total tape length	403.4 m	517 m
Winding / bonding	Layer winding / epoxy resin	
Coil inductance	0.0876 H	0.144 H
Stored magnetic energy	0.598 kJ	0.720 kJ
Magnetic field strength B_r: radial component B_z: perpendicular component	 0.6043 T 0.7944 T	 0.656 T 0.841 T

3.2 Plasma Production

Plasmas in the Mini-RT are produced and heated by Electron Cyclotron Heating (ECH) with continuous microwaves at 2.45 GHz and 1.0 - 2.5 kW. Figure 3.5 shows the diagram of plasma production. The mode of the microwaves is selected by applying straight waveguide or twisted waveguide. A straight waveguide is used for O wave injection and a twisted waveguide is for X wave injection. In this research, the O mode waves were injected. The produced plasma is maintained for 7 seconds by keeping injection of continuous microwaves. The cutoff density for 2.45 GHz is $7.4 \times 10^{16} \mathrm{m}^{-3}$. Filler gas is hydrogen and typical pressure of it is 10^{-3} - 10^{-1} Pa with base pressure of 10^{-5} Pa.

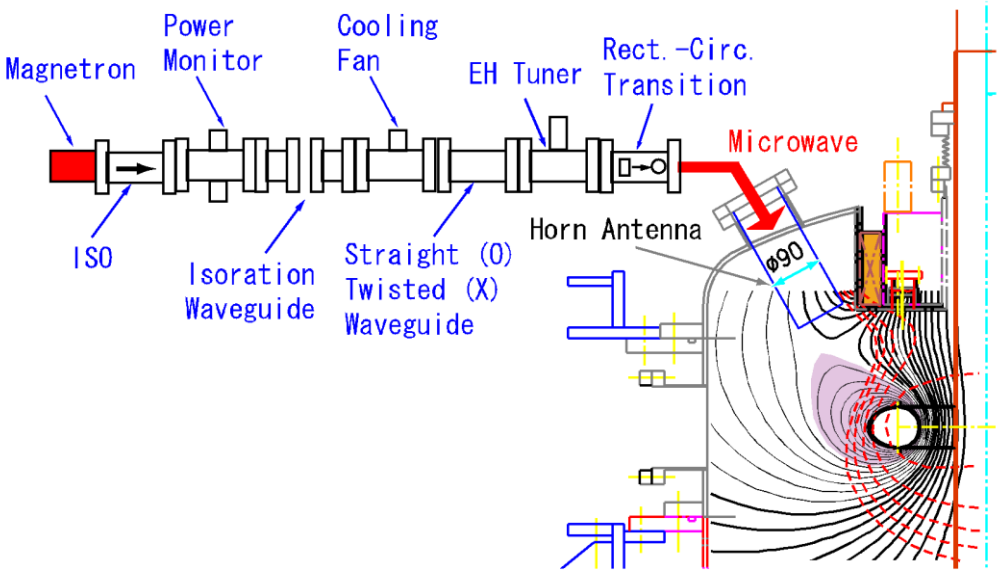

Figure 3.5: Schematic diagram of the plasma production system

Chapter 4
Numerical Analysis

As mentioned in Ch.2, the EBW excitation requires that X-mode microwaves reach the UHR layer and three ways of accessibility are well known, i.e. FX-SX-B, SX-B and O-X-B conversion methods. The mode conversion efficiency depends on the propagation characteristics of electromagnetic waves in Electron Cyclotron Range of Frequencies (ECRF) such as tunneling, cutoff, O-X mode band. In this chapter, two approaches for description of wave propagation in plasma are mentioned. One approach is the geometrical optical approximation known as ray tracing, and the second one is so called full-wave solution that Maxwell equations are directly solved.

4.1 Ray Tracing method

If the wavelength of the incident wave is sufficiently smaller than the typical scale length of plasma parameters, the effectiveness of geometrical optical approximation is guaranteed and the wave is described as a ray. Since the wavelength of EBW is the order of Larmor radius, the ray tracing method is useful for describing the wave trajectory. However, in the Mini-RT device whose major radius is 500 mm, this approximation for the electromagnetic mode whose frequency is the order of GHz and whose wave length is the order of ~ cm, is no longer valid. In addition, the ray doesn't have the tunneling incident effect, so it can only propagate in the region where the dispersion curve connects in real number space, which corresponds to the case of $N_{\parallel} = N_{\parallel opt}$. In this section, to estimate O-X-B conversion process in the Mini-RT briefly, wave trajectories of incident

microwaves from the top of the vacuum vessel are described with the ray tracing method by using force assumption of geometrical optics.

The direction of the energy flow of the wave is given by group velocity $\boldsymbol{v}_g = \partial\omega / \partial\boldsymbol{k}$, and then angular frequency ω and wave number vector $\boldsymbol{k}$ have to satisfy the dispersion relation $D(\omega, \boldsymbol{k}, \boldsymbol{r}, t) = 0$ according to varying of the time and the coordinate of the ray. Assuming that the dispersion function D includes no loses, the angular frequency ω can be written as $\omega = \omega(\boldsymbol{r}, \boldsymbol{k}, t)$. Then, time developments are given [28] by

$$\boldsymbol{v}_g = \frac{d\boldsymbol{r}}{dt} = -\left(\frac{\partial D}{\partial \boldsymbol{k}} \Big/ \frac{\partial D}{\partial \omega} \right), \qquad \frac{d\boldsymbol{k}}{dt} = \frac{\partial D}{\partial \boldsymbol{r}} \Big/ \frac{\partial D}{\partial \omega}, \qquad \frac{d\omega}{dt} = \frac{\partial D}{\partial t} \Big/ \frac{\partial D}{\partial \omega} \tag{4.1}$$

The dispersion function of the injected O wave and the X wave and of the excited EBW was obtained in Ch.2 as Eqs. (2.62) and (2.42). Then, we can describe the wave trajectories in the plasma by integration of Eq. (4.1). The ray tracing method is able

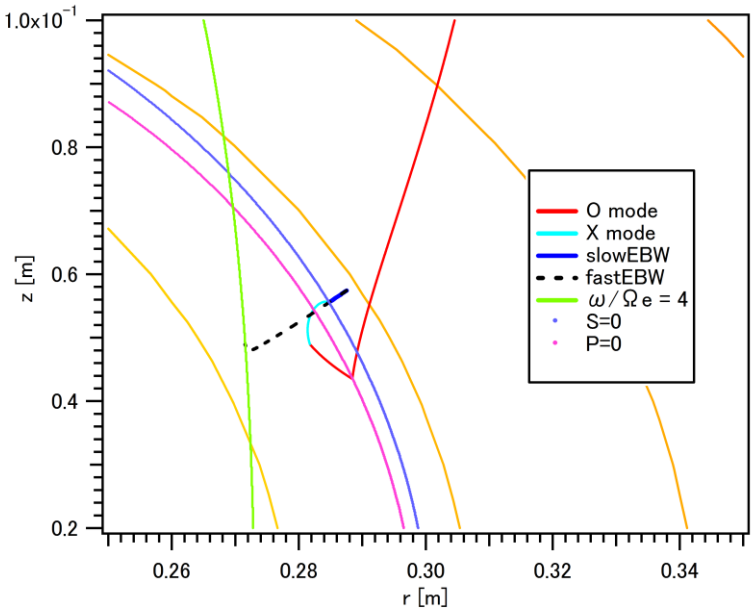

Figure 4.1: O-X-B conversion trajectory in the Mini-RT

The O wave is injected from the top of the vacuum vessel and couples to the X wave at P-cutoff. The EBW excited at the UHR propagates toward the core plasma region and is damped down at the 4th ECR by resonance absorption.

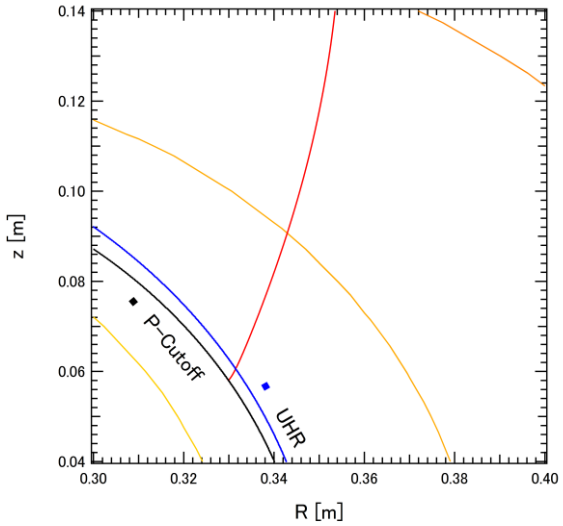

Figure 4.2: Non-optimal injection

The injected O wave is reflected at P-cutoff line and cannot propagate into core region nor be absorbed.

us to obtain other wave properties such as damping, reflect and energy absorption in addition to the chase of wave trajectories.

Ray tracing calculations are carried out to show the possibility of the O-X-B conversion in the internal coil device Mini-RT. This device has purely poloidal magnetic field, so the plasma can be regard as identical for toroidal way. Therefore this calculation is carried out only in the poloidal cross section. The plasma parameters are assumed as a function of magnetic surface which is produced by internal superconductor coil, and are located two dimensionally. The frequency of injected microwave is 1.0 GHz, and the density of the plasma at the core is about 5×10^{16} m^{-3}. The microwave is injected as a beam from the top of vacuum vessel so that the polarization of the wave can be the O mode wave. As described in Ch.2 in the O-X-B conversion parallel component of the wave is a cardinal factor. The Mini-RT device has closed magnetic lines in the poloidal cross section, so that the parallel component of the wave number vector has a periodic boundary condition along the field line. The poloidal mode number is determined by initial argument of the tangent between the field line and wave number vector. Figure 4.1 shows the wave trajectory whose mode is converted from O mode into the SX mode and the Bernstein mode, in the Mini-RT device. In the case of Fig. 4.1 the initial

injection angle which is determined at the last closed magnetic surface is 75.06°. The O wave is launched from the top of the vacuum vessel toward the center of the plasma. The wave propagates to the P-cutoff line (shown as the rose line) and then the mode is converted into the SX mode and the wave propagates to the higher density region. After the slightly rollback, the SX wave reach the UHR layer (shown as the light blue line) and is converted into the EBW. The EBW propagates toward the core of the plasma and absorbed at the ECR layer (the 4th ECR is shown as the green line). This is the optimal case of the O-X-B conversion. If the initial injection angle moves a little over, the branch of the O wave and that of the SX wave cannot be connected. Figure 4.2 shows the case of non-optimum. The injected O wave is reflected at P-cutoff line and cannot propagate to higher density region. These results are too sensitive because the conversion efficiency curve has broadening shape. This is a bound of the ray tracing method. In addition, the assumption of parallel mode conservation could well have error factors attributed to the collapse of the approximation of geometrical optics.

4.2 FDTD method

As mentioned above, geometrical optics is applicable only in the media whose scale length of the refractive index is much longer than the incident wavelength. The plasma in the Mini-RT which is treated in this research has the scale about the order of 10 cm, so the geometrical optics is not applicable for the 1GHz microwaves. Therefore, in order to analyze wave propagation in the Mini-RT plasma, it is necessary to directly solve the Maxwell equations.

4.2.1 Basic Concept of FDTD

The Finite-Difference Time-Domain (FDTD) scheme is an explicit method [45] [46] for the Maxwell equations that are shown in Eqs. (2.3) and (2.4). This is a popular technique to calculate the propagation of the electromagnetic wave in

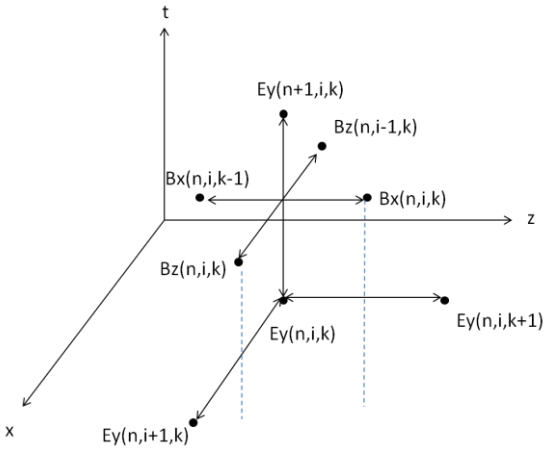

Figure 4.3: Illustration of the location of electric and magnetic component. The spatial and temporal derivatives of each component by finite difference coincide in an equation.

inhomogeneous media like as magnetized plasma [47] [48]. The finite-difference method enables us to visualize the spatial wave pattern in detail, and the time-domain method does us to obtain time evolution of the propagation and the mode conversion processes. According to Yee's FDTD algorithm [49] magnetic and electric field components are located between a pair of the other component in each time step. In Yee cell, since the electric and magnetic fields are present with shifted by a half step with each other, the boundary conditions are set only for the electric field at the interface. The FDTD method adopts the central difference and the temporal derivatives of $\boldsymbol{E}$ and $\boldsymbol{B}$ by finite differences can be written as follows;

$$\left.\frac{\partial \boldsymbol{E}}{\partial t}\right|_{\left(1-\frac{1}{2}\right)n\Delta t} = \frac{\boldsymbol{E}^{n} - \boldsymbol{E}^{n-1}}{\Delta t} \tag{4.2}$$

$$\left.\frac{\partial \boldsymbol{B}}{\partial t}\right|_{n\Delta t} = \frac{\boldsymbol{B}^{n+\frac{1}{2}} - \boldsymbol{B}^{n-\frac{1}{2}}}{\Delta t}, \tag{4.3}$$

where Δt is the time increment and the superscript n is the time index, i.e. $F(t) = F(n\Delta t) = F^{n}$. Then the Maxwell equations with this notation result in following equations;

$$\frac{\boldsymbol{E}^{n} - \boldsymbol{E}^{n-1}}{\Delta t} = c^{2}\nabla \times \boldsymbol{B}^{n-\frac{1}{2}} - \frac{1}{\epsilon_{0}}\boldsymbol{j}^{n-\frac{1}{2}} \tag{4.4}$$

$$\frac{\boldsymbol{B}^{n+\frac{1}{2}} - \boldsymbol{B}^{n-\frac{1}{2}}}{\Delta t} = -\nabla \times \boldsymbol{E}^{n}. \tag{4.5}$$

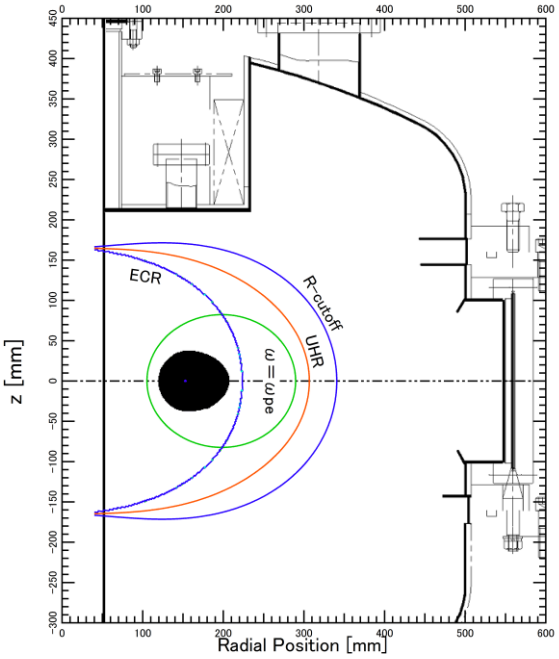

Figure 4.4: The cross section of the Mini-RT device

The cutoff and resonance lines are described for 1.0HGz microwave in typical profile of hydrogen plasma which is produced by 2.45 GHz microwave.

The response of the plasma appears in the current density $\boldsymbol{j}$ as the motions for electrons and ions. In cold plasma approximation, the motions of the charged particles are described by Eq. (2.14). Assuming that the plasma is one species of hydrogen and the velocity of ions is much smaller than that of electrons, the first order of the current density due to the cold plasma is written as

$$\frac{\partial \boldsymbol{j_1}}{\partial t} = \epsilon_0 \omega_{pe}^2 \boldsymbol{E} - \frac{e}{m_e} \boldsymbol{j_1} \times \boldsymbol{B_0} - \nu \boldsymbol{j_1}, \tag{4.6}$$

where ν is the collisional frequency. The $\nu \boldsymbol{j_1}$ term is responsible for collisional damping of the wave. In the cold plasma model, the propagation of the EBW and the mode conversion which occurs at the UHR cannot be described, but tunneling and the cutoff is able to be. Therefore, this model is fruitful for analysis of the wave propagation and accessibility to the resonance or cutoff in a plasma device.

4.2.2 Two-dimensional Calculation

As described, the Mini-RT device has purely poloidal magnetic field. Thus,

the wave analyses of the cross section of the Mini-RT are conducted as to be isotropic in the toroidal direction. Thus parameters are independent of the y direction. Thus, $\partial/\partial y \to 0$ and an arbitrary function of space and time can be written as $F(t,x,y,z) \to F(n\Delta t, i\Delta x, k\Delta z) = F^n(i,k)$. Figure 4.3 shows the two dimensional coordinate system and the grid positions of E and B components, where each E component is located between a pair of B components and vice versa. The current density $\boldsymbol{j}$ exists with E component simultaneously, and is located at the same point of B component in order not to conflict with constitutive equations. By solving Eqs. (4.5), (4.5) and (4.6), one gets

$$B_x^n(i,k) = \frac{\Delta t}{\Delta z}\Big(E_y^n(i,k+1) - E_y^n(i,k)\Big) + B_x^{n-1}(i,k) \tag{4.7}$$

$$B_y^n(i,k) = -\Delta t\left(\frac{E_{x^n}(i,k+1) - E_x^n(i,k)}{\Delta z} - \frac{E_z^n(i+1,k) - E_z^n(i,k)}{\Delta x}\right) + B_y^{n-1}(i,k) \tag{4.8}$$

$$B_z^n(i,k) = -\frac{\Delta t}{\Delta x}\Big(E_y^n(i+1,k) - E_y^n(i,k)\Big) + B_z^{n-1}(i,k) \tag{4.9}$$

$$E_x^{n+1}(i,k) = -\frac{c^2\Delta t}{\Delta z}\Big(B_y^n(i,k) - B_y^n(i,k-1)\Big) - \frac{\Delta t}{\epsilon_0} j_{1x}^n(i,k) + E_x^n(i,k) \tag{4.10}$$

$$E_y^{n+1}(i,k) = c^2\Delta t\left(\frac{B_x^n(i,k) - B_x^n(i,k-1)}{\Delta z} - \frac{B_z^n(i,k) - B_z^n(i-1,k)}{\Delta x}\right) - \frac{\Delta t}{\epsilon_0} j_{1y}^n(i,k) + E_y^n(i,k) \tag{4.11}$$

$$E_z^{n+1}(i,k) = \frac{c^2\Delta t}{\Delta x}\Big(B_y^n(i,k) - B_y^n(i-1,k)\Big) - \frac{\Delta t}{\epsilon_0} j_{1z}^n(i,k) + E_Z^n(i,k) \tag{4.12}$$

$$j_{1y}^n(i,k) = \frac{(1+\nu\Delta t)\gamma + \Delta t(\Omega_{ez}\alpha - \Omega_{ex}\beta)}{(1+\nu\Delta t)^2 + (\Omega_{ex}^2 + \Omega_{ez}^2)\Delta t^2} \tag{4.13}$$

$$j_{1x}^n(i,k) = \frac{1}{1+\nu\Delta t}\Big(\alpha - \Delta t\Omega_{ez}\, j_{1y}^n(i,k)\Big) \tag{4.14}$$

$$j_{1z}^n(i,k) = \frac{1}{1+\nu\Delta t}\Big(\beta + \Delta t\Omega_{ex}\, j_{1y}^n(i,k)\Big), \tag{4.15}$$

where

$$\Omega_{ex} = \frac{eB_{0x}}{m_e}$$
$$\Omega_{ez} = \frac{eB_{0z}}{m_e} \tag{4.16}$$

$$\alpha = j_{1x}^{n-1}(i,k) + \Delta t \epsilon_0 \omega_{pe}^2 E_x^n(i,k)$$
$$\beta = j_{1z}^{n-1}(i,k) + \Delta t \epsilon_0 \omega_{pe}^2 E_z^n(i,k) \tag{4.17}$$
$$\gamma = j_{1y}^{n-1}(i,k) + \Delta t \epsilon_0 \omega_{pe}^2 E_y^n(i,k).$$

Figure 4.4 shows the cross section of the Mini-RT device and characteristic location of cutoff and resonance for 1.0 GHz microwave in typical plasma parameters. It is assumed that injected microwaves are radiated from the antenna which is placed at the internal coil level and excites an electric field in the toroidal direction, which corresponds to X wave injection. The source of the microwave is regarded as a spot source and microwaves are spread as spherical waves, so that injected wave results in perpendicular X wave injection in a slab of internal coil level. 1.0 GHz microwaves are supplied continually with modulated end to gentle.

The grid size and the time increment have to be chosen with care for numerical dispersion and stability. The grid size has to be much smaller than the wavelength in order not to change the wave properties significantly. In this work $\delta = \Delta x = \Delta z = 1$ mm is chosen. According to Ref. [50], it is possible to compute in a stable manner in the numerical dispersion of about 5 % or less in the refractive index N within a range of $0.18 \leq N^2 \leq 3600$. In addition, time increment also has some restriction to ensure the stability of the time-stepping algorithm [51]. This condition is referred to as Courant-Friedrichs-Lewy (CFL) condition [52];

$$c\Delta t \leq \left(\frac{1}{\Delta x^2} + \frac{1}{\Delta y^2} + \frac{1}{\Delta z^2}\right)^{-\frac{1}{2}}, \tag{4.18}$$

where c is the speed of light. On 2d grid with equal grid sizes δ, Eq. (4.18) is reduced to

$$\sqrt{2}c\frac{\Delta t}{\delta} \leq 1. \tag{4.19}$$

The time increment of this work is 1 ps. Then the left hand of Eq. (4.19) corresponds to 0.42 which satisfies the CFL condition.

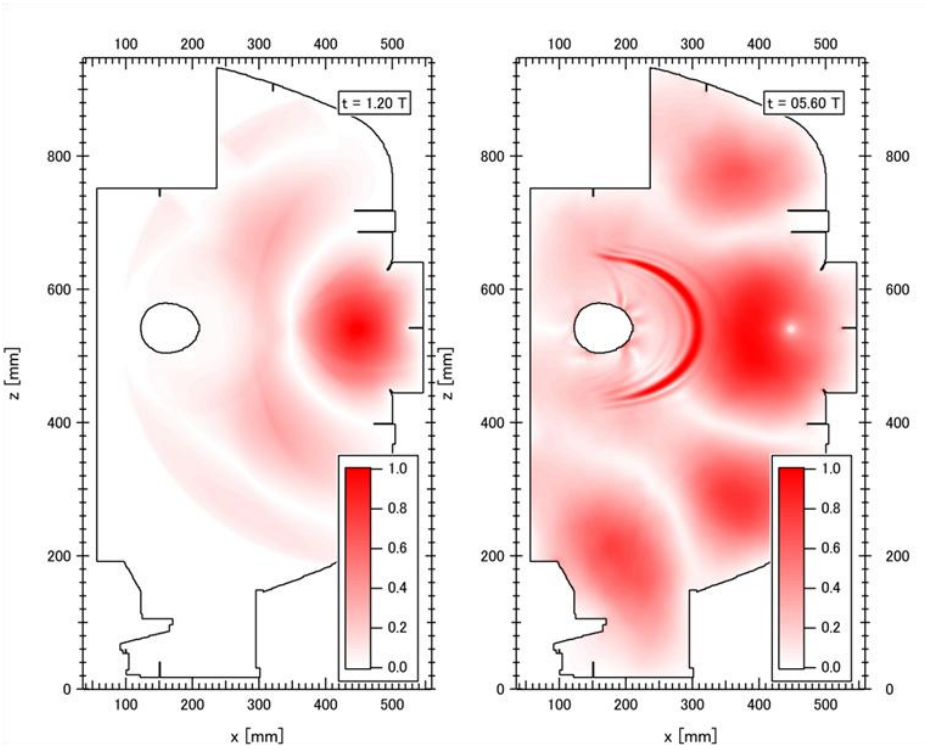

(a) t = 1.2 oscillation periods (b) t = 5.6 oscillation periods

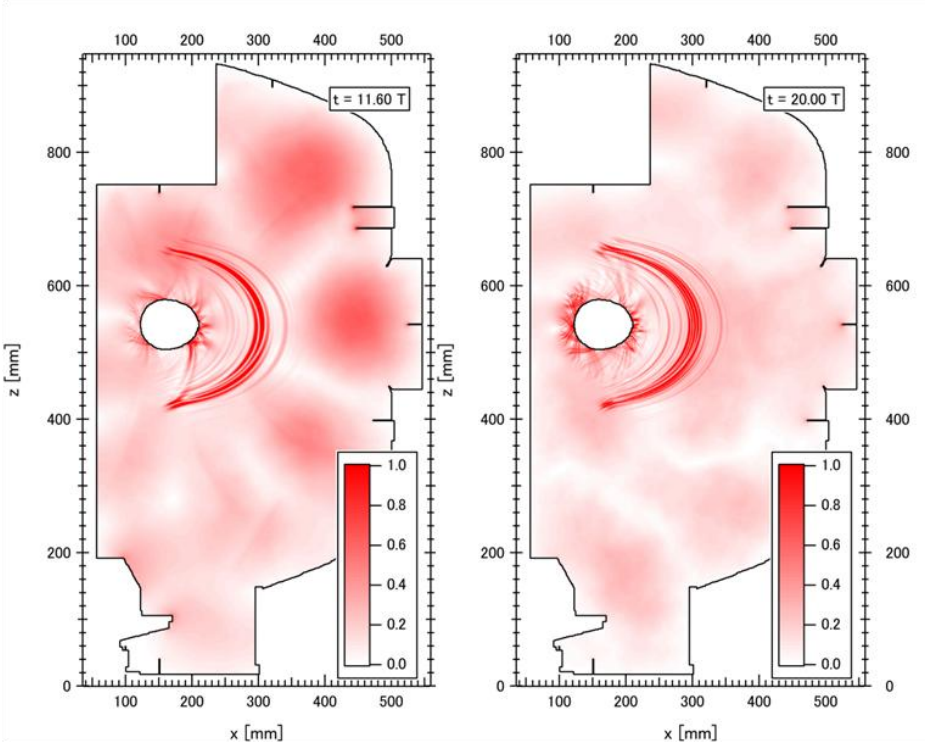

(c) t = 11.6 oscillation periods (d) t = 20.0 oscillation periods

Figure 4.5: Time evolution of electric field intensity pattern

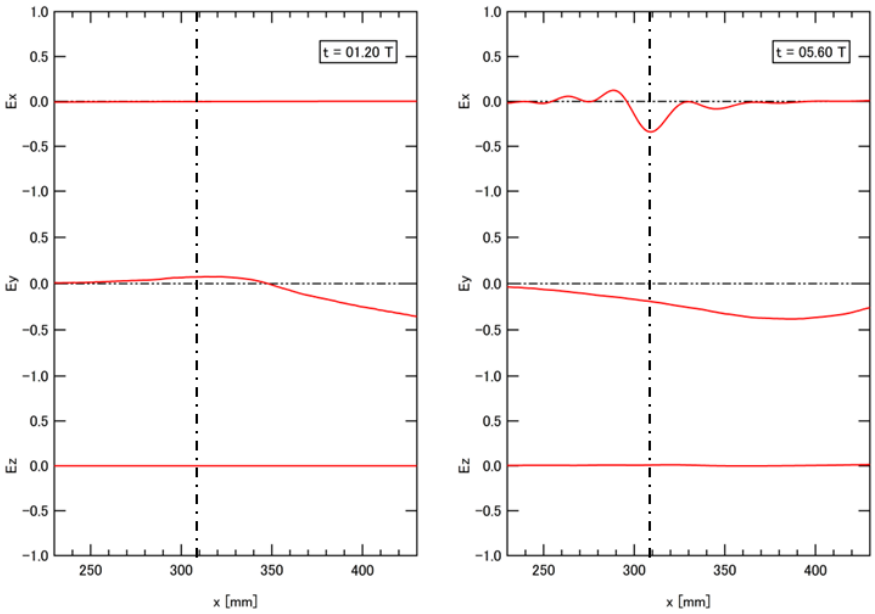

(a) t = 1.2 oscillation periods (b) t = 5.6 oscillation periods

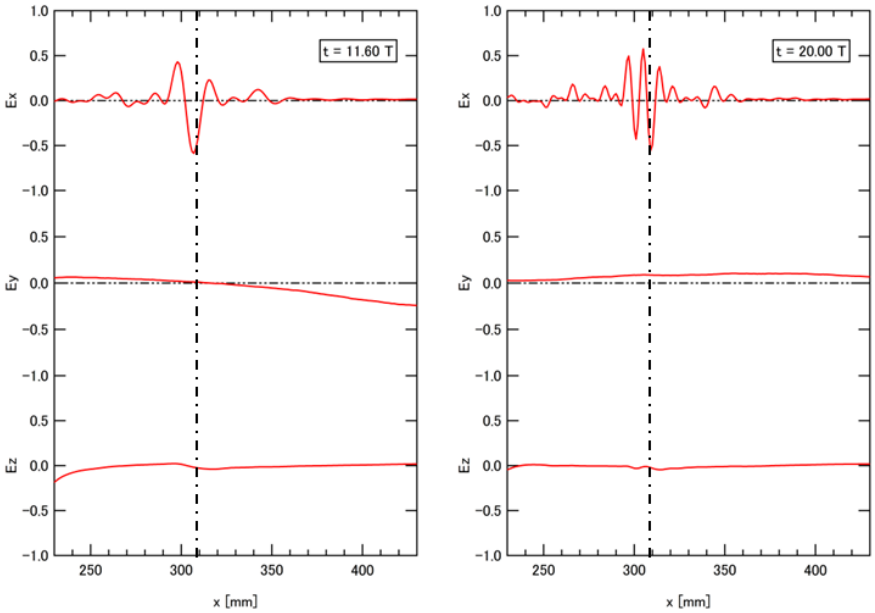

(c) t = 11.6 oscillation periods (d) t = 20.0 oscillation periods

Figure 4.6: Time evolution of the electric filed profiles

The UHR is located about x = 310 mm (shown as dot-dash lines). The short wavelength mode is excited for a few oscillation periods and its wavelength becomes shorter about 10 mm after 20 oscillation periods.

The boundary conditions to the electric field are set as a perfect conductor wall of vacuum vessel and the shield of internal coil, i.e. electric field parallel to the surface is set to zero at the grid points where the wall is located.

4.2.3 Wave Propagation in the Mini-RT

Figure 4.5 shows the time evolution of the wave pattern in the cross section of the Mini-RT. Since the X waves are injected from low field side, the FX-SX-B conversion is expected. The injected microwave at 1.0 GHz whose wavelength is 10 cm in vacuum, propagate toward the center of the vessel (Fig. 4.5 (a) at t = 1.2 oscillation periods). The wave is inundated with being reflected at cutoffs, vacuum vessel wall and internal coil, and reach the UHR layer after tunneling the evanescent region (Fig. 4.5 (b) at t = 5.6 oscillation periods). After a while, a short-wavelength-wave mode is excited at the UHR (Fig 4.5 (c) at t = 11.4 oscillation periods), and the wavelength of this mode becomes shorter (Fig. 4.5 (d) at t = 20.0 oscillation periods). Figure 4.6 shows the time evolution of wave pattern at the internal coil level. At first, the injected wave has only y-component of electric field corresponding to the X mode (Fig. 4.6 (a) at t = 1.2 oscillation periods). The UHR layer is located about x = 310 mm at z = 0 level and the longitudinal polarization component (x component of electric field) begins to be excited at the UHR (Fig. 4.6 (b) at t = 5.6 oscillation periods). Then, in the component of longitudinal polarization, the wavelength becomes shorter and the amplitude does larger (Fig 4.6 (c) at t = 11.4 oscillation periods). Finally, the wavelength attains about 10 mm near the UHR (Fig. 4.6 (d) at t = 20.0 oscillation periods). In this calculation, since the response of the plasmas is expressed by cold plasma approximation, the short-wavelength mode is corresponds to the UHR wave and stays near the UHR layer.

4.2.4 Mode Conversion into the EBW

Although the cold plasma model can exhibit basic characteristics

(polarization, resonance at the UHR, tunneling, cutoff and so on), to describe mode conversion to the EBW mode and its propagation, the thermal effect is need to be introduced. Thus, hot plasma formalism, described at Ch. 2, is substituted into the current density terms, i.e. Eq. (4.6) is written as follows;

$$\frac{\partial \boldsymbol{J}(\omega, \boldsymbol{k})}{\partial t} = -\omega^2 \epsilon_0 \overleftrightarrow{\chi}(\omega, \boldsymbol{k}) \boldsymbol{E}(\omega, k), \tag{4.20}$$

where $\overleftrightarrow{\chi}$ is a susceptibility tensor, described in Eq. (2.39). Here, we assumed that $\overleftrightarrow{\chi}$ can be divided into $\overleftrightarrow{\chi}_{hot}$ and $\overleftrightarrow{\chi}_{cold}$. Then, the first order of $\boldsymbol{D}$ corresponds to that of cold plasma, and the second order of $\boldsymbol{D}$ can be written as follows;

$$\boldsymbol{D_2}(\omega) = \epsilon_0 \big(\boldsymbol{E_2}(\omega) + \overleftrightarrow{\chi}_{cold}(\omega) \cdot \boldsymbol{E_2}(\omega) + \overleftrightarrow{\chi}_{hot} \cdot \boldsymbol{E_1}(\omega) \big). \tag{4.21}$$

Once here, with fixed the wave number $\boldsymbol{k}$, domain is converted from frequency to time. Note that the Fourier transform of the product is an integral convolution of the Fourier transform:

$$\mathcal{F}^{-1}\{f(\omega)g(\omega)\} = \int_{-\infty}^{t} f(\tau)g(t-\tau)d\tau = f * g. \tag{4.22}$$

Since the EBW is an electrostatic mode, $\boldsymbol{D}_2$ equals to zero, and the electric field of EBW can be written as

$$\boldsymbol{E}_2(t) + \overleftrightarrow{\chi}_{cold}(t) * \boldsymbol{E}_2(t) + \overleftrightarrow{\chi}_{hot}(t) * \boldsymbol{E}_1(t) = 0. \tag{4.23}$$

4.2.5 RC scheme

An temporal discretized convolution $(\chi * E)^n$ results in the following formula;

$$\begin{aligned} (\chi * E)^n &= \int_0^{n\Delta t} \chi(\tau) E(n\Delta t - \tau) d\tau \\ &= \sum_{m=0}^{n-1} E^{n-m} \int_{m\Delta t}^{(m+1)\Delta t} \chi(\tau) d\tau. \end{aligned} \tag{4.24}$$

If there is a following relationship between the mth integral and $(m+1)$th integral

$$\int_{(m+1)\Delta t}^{(m+2)\Delta t} \chi(\tau) d\tau = \alpha \int_{m\Delta t}^{(m+1)\Delta t} \chi(\tau) d\tau, \tag{4.25}$$

then the convolution can result in a recurrence formula;

$$
\begin{aligned}
(\chi * E)^n &= E^n \int_0^{\Delta t} \chi(\tau) d\tau + \sum_{m=1}^{n-1} E^{n-m} \int_{m\Delta t}^{(m+1)\Delta t} \chi(\tau) d\tau \\
&= E^n \int_0^{\Delta t} \chi(\tau) d\tau + \sum_{m'=0}^{n-2} E^{n-m'-1} \int_{(m'+1)\Delta t}^{(m'+2)\Delta t} \chi(\tau) d\tau \\
&= E^n \int_0^{\Delta t} \chi(\tau) d\tau + \alpha(\chi * E)^{n-1}.
\end{aligned} \tag{4.26}
$$

This scheme which makes convolution result in recurrence formula is called as Recursive Convolution (RC) scheme [45] [46].

Here, assuming that χ_{hot} has only diagonal components, we can solve Eq. (4.23) and represent E_2 as;

$$
E_2^n = \frac{\alpha(\chi_{cold} * E_2)^{n-1} + \chi_{hot} * E_1^n}{1 + \int_0^{\Delta t} \chi_{clod}(\tau) d\tau}. \tag{4.27}
$$

For perpendicular propagation to B_0, the xx component of the hot plasma susceptibility tensor is written as series expansion of k;

$$
\chi_{xx} = -\frac{\omega_{pe}^2}{\omega^2 - \Omega_e^2} - \frac{1 \cdot 3 \frac{v_{th}^2}{2} \omega_{pe}^2 k_\perp^2}{(\omega^2 - \Omega_e^2)(\omega^2 - (2\Omega_e)^2)} - \cdots, \tag{4.28}
$$

where the first term corresponds to that of the cold plasma susceptibility, so that the second term is set to be χ_{hot} in particular case where only the dominant first order term in Larmor radius expansion and perpendicular dispersion are considered in the plasma current [53] [54]. Since Eq. (4.28) has ω only in denominator, this is a proper form in Laplace transformation. Setting as $s = i(\omega + i\omega_i)$, Laplace transformation technique is useful and χ can be easily inverse Laplace transformed. The wave number vector is only numerator as $k_\perp^2$, so that inverse Fourier for k is written as follows;

$$
\mathcal{F}^{-1}\{-k_\perp^2 E(k,t)\} = \frac{\partial^2}{\partial x^2} E(x,t). \tag{4.29}
$$

4.2.6 1D FX-SX-B Conversion

To demonstrate FX-SX-B conversion, 1D model calculations are carried out in assumption of the Mini-RT typical parameters; electron density, temperature and external magnetic field. The injected microwaves are assumed to be 1.0 GHz and X

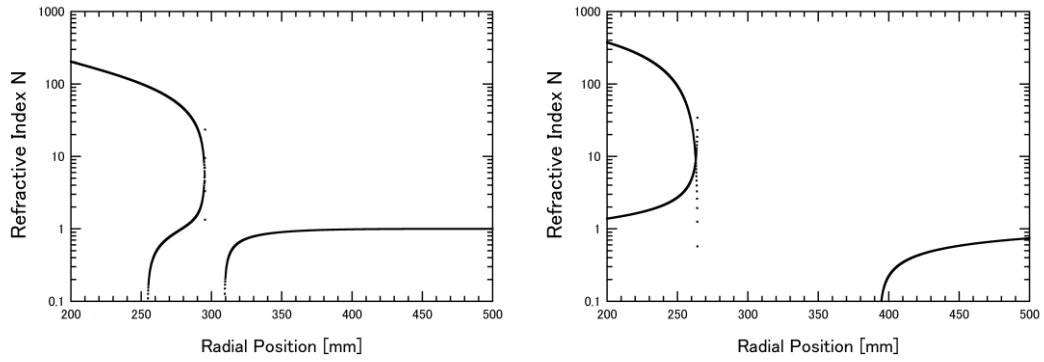

Figure 4.7: Assumed refractive index profiles

(a) Assumption of steep density gradient (b)Assumption of moderate density gradient

mode, and injected from low field side at z = 0 line. The wavelength of the EBW is estimated about 2 mm, so that the spatial grid size is set to be 0.1 mm. Two cases are assumed; one is steep density gradient profile, which corresponds to applying levitation coil current, and the other is moderate gradient. Figure 4.7 shows the refractive index profile in these assumptions, which is solved in wave number and angular frequency domain. In Fig.4.7 (a) the UHR is located at major radius R = 295 mm, where the EBW mode is excited, and R-cutoff is at R = 310 mm, while in the case of the Fig.4.7 (b) the UHR is located at 265 mm and R-cutoff is at 395 mm. Thus, in the case of Fig. 4.7 (a), tunneling parameter $k_0\Delta x = \eta$ is 0.05, and in the case of Fig. 4.7 (b), η becomes 2.7, where k_0 is wave number in vacuum and Δx is the distance between the UHR and R-cutoff.

A numerical result of 1D FX-SX-B conversion is shown in Fig.4.8 and Fig. 4.9. Figure 4.8 shows time evolution of electric fields and mode conversion process. The incident X wave has only Ey component at first (Fig. 4.8 (a)), and then Ex component corresponding to longitudinal polarization arises at the UHR (Fig. 4.8(b)). The wavelength of longitudinal component becomes shorter gradually, and begins to propagate toward higher density region (Fig. 4.8 (c)). Finally, the wavelength becomes about 3 mm, which corresponds to refractive index of 100, and gets to be steady state (Fig. 4.8 (d)). This temporal series of flow is showing the FX to SX conversion and SX to B-mode conversion.

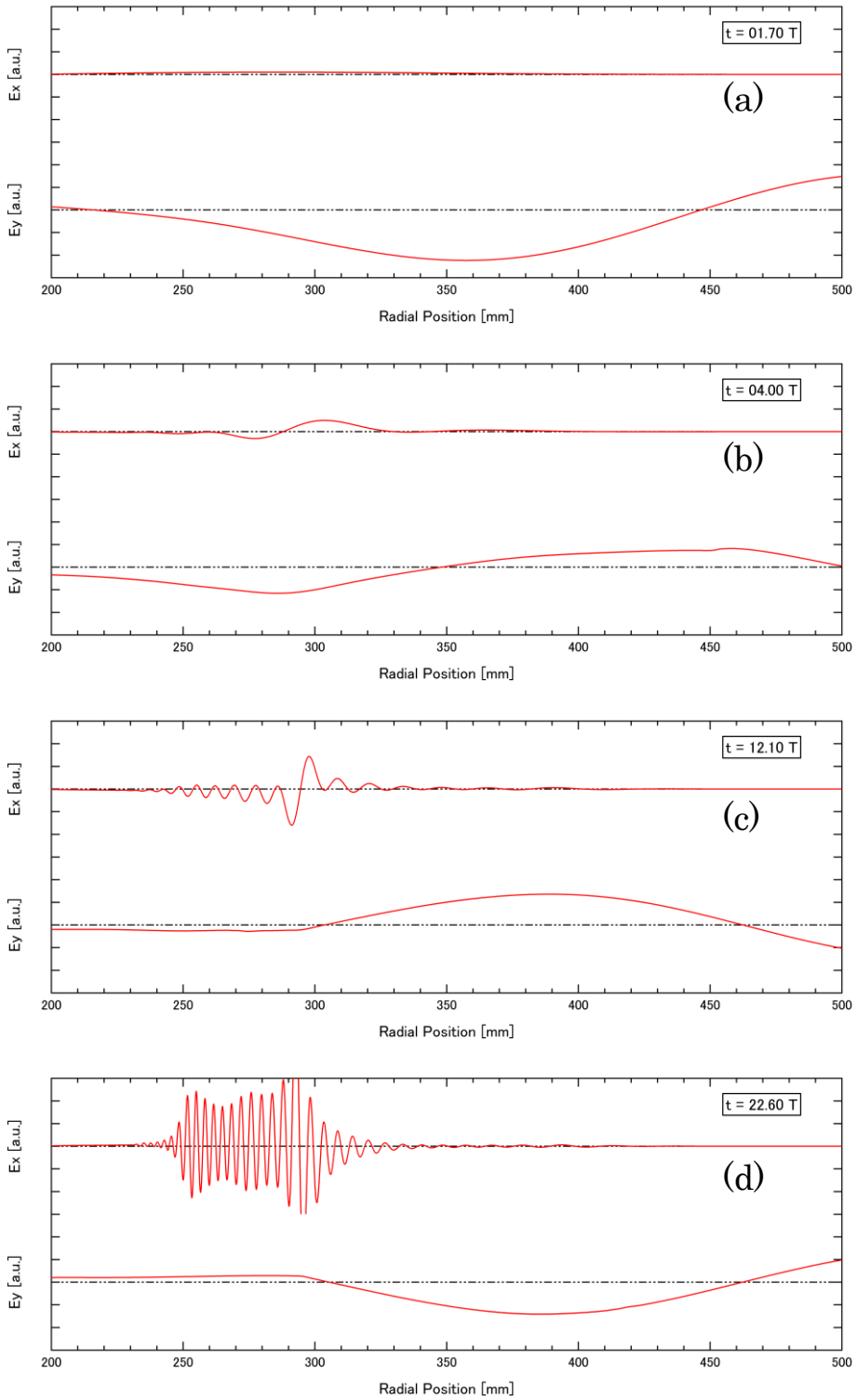

Figure 4.8: 1D simulation of the FX-SX-B conversion

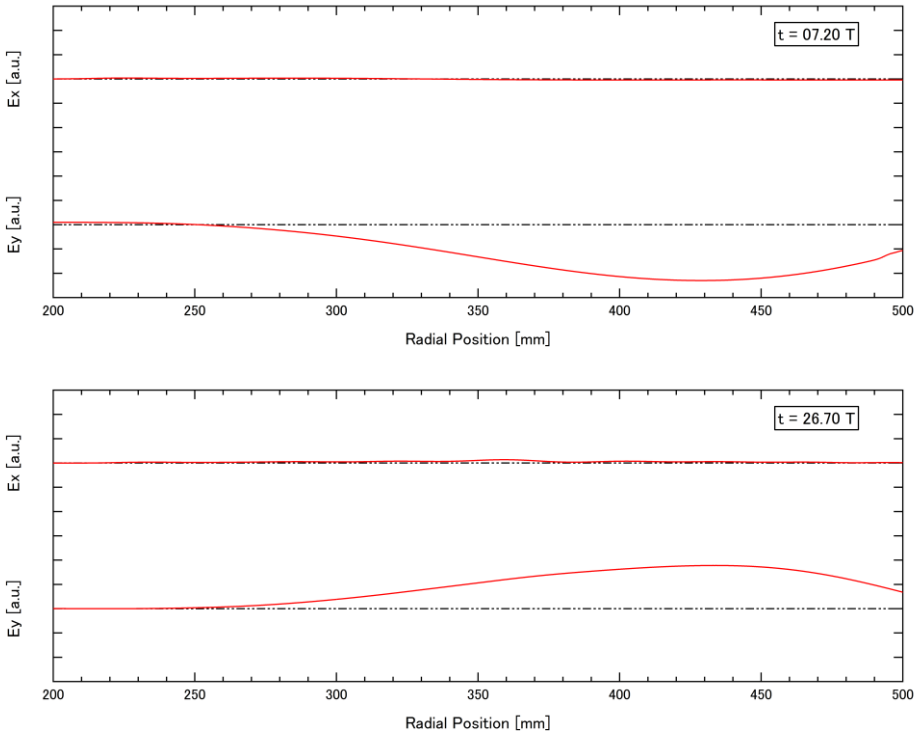

Figure 4.9: 1D simulation in the case of Fig.4.7 (b)

On the other hand, in the case of large η, the short-wavelength mode does not appear. Figure 4.9 shows time evolution of electric fields in the case of Fig. 4.7 (b). In this case, Ex component becomes long-wavelength mode which corresponds to the polarization of the FX mode in a low density plasma and in high density region (R < 300), both components of Ex and Ey are damped down.

It is demonstrated that the perpendicularly injected X mode from low field side is converted into the EBW mode with temporal evolution. However, this calculation adopts some approximation. The susceptibility tensor was expanded with small λ, so that this approximation loses its validity in the region of large N. In addition, ignoring high order term of λ make us lose the effect of high-harmonic ECR. This calculation only concern χ_{xx} component, but in order to exhibit oblique propagation and to be expanded for 2-dimensional calculation, the equations should be solve for 3×3 matrix.

4.3 Summary of Numerical Analyses

Two methods for numerical analysis have been described in this chapter. The ray tracing calculations have shown the wave trajectories with satisfying their dispersion relations and mode conversion scheme form injected O waves into the EBWs. Since the ray tracing method applied to the Mini-RT device, where the wavelength of incident 1.0 GHz microwave is comparable in the size to the major radius of the device, understandingly contains the force approximation of geometrical optics, the O-X-B conversion in the device should be investigated with full-wave calculations and plasma experiments. However, it is shown that microwaves injected from the top of the vacuum vessel have a possibility of EBW excitation via O-X-B conversion scenario in a certain optimal condition. Thus, these results may be some indicators for actual architectonics of microwave launching systems for EBW excitation by O-X-B conversion method.

The FDTD calculations, where Maxwell equations are directly solved, have shown spatial wave pattern with time evolution. On 2d grid in the Mini-RT, where the cold plasma model is applied, it has shown that injected fast-X waves propagate toward core plasma region and tunnel the evanescent region, and short-wavelength mode whose polarization has large longitudinal component is excited around the UHR layer. This short-wavelength mode is coupled to the EBW mode, so that the possibility of FX-SX-B conversion in the device has been shown including the excitation antenna, reflected waves and configuration. Furthermore, 1D grid model including warm plasma effect has shown FX-SX-B conversion with time evolution, and serves as a stepping stone to full-coverage analyses of the device including antennas and O-X-B conversion.

Chapter 5
Experimental Setup

5.1 Measurement System

As mentioned in Ch.3, plasmas are produced by 2.45 GHz microwaves in the internal coil device Mini-RT. In the device, waves at frequencies lower than 2.45GHz was injected to diagnose wave propagation in overdense plasmas; the plasma produced by 2.45 GHz microwaves acts as an overdense plasma with respect to lower frequency diagnostic waves. In this work, diagnostic waves at 1.0 ~ 1.6 GHz were injected from low field side and high field side. To examine the mode conversion of the waves from electromagnetic to electrostatic mode, the electromagnetic and electrostatic components were measured simultaneously by probing antennas inserted directly into the plasmas.

5.1.1 Interferometry System

Interferometry enables us to obtain a snapshot of the electric or magnetic field [55]. Several modes of the waves have been investigated with directly observation by using interferometry systems such as lock-in amplifier [56] [57]. The profiles of electromagnetic field appear as waveforms and give us some characteristics of the wave, i.e. wavelength, phase, amplitude. The characteristics of the EBW require high axial resolving power, i.e. the wavelength of the EBW is the order of Larmor radius, excitation occurs at limited region and the EBW is efficiently absorbed at any ECR layer. Interferometry combined to IQ demodulation gives us precise measurements and is immune to noises [52].

Figure 5.1 shows as schematic diagram of the diagnostic system in the

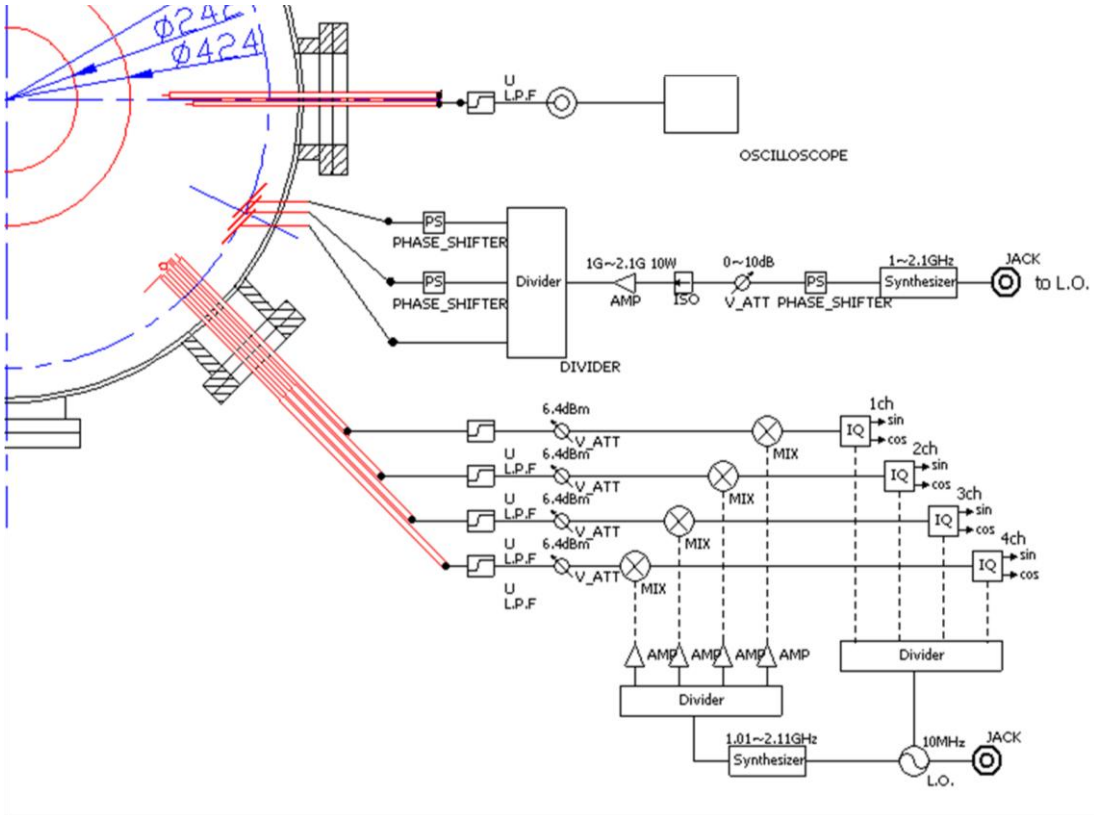

Figure 5.1: Schematic diagram of diagnostics

Mini-RT. The local oscillator generates microwaves at 10 MHz and they are split in three signals; one is reference signal for IQ demodulation, another is transmission wave, and the other is reference signal for heterodyne interferometer. A synthesizer on the transmission lice generates 1.0 - 2.1 GHz microwaves from 10 MHz microwaves sent to it. The transmission microwaves are phase-controlled by phase shifter and variable attenuator and amplifier adjust the injection power 1 – 10 W. To prevent the 2.45 GHz microwaves used for plasma production from affecting the diagnostic circuits, a band pass filter was installed in each line. Figure 5.2 shows the band pass filter in (a) and its frequency characteristics (b). The transmission microwaves are divided into three lines in order to control the propagation pattern of injection waves by phased array antenna, and are injected into the plasma. The injected waves are detected by probing antennas and are mixed with reference signals which are synthesized so that the difference of the frequency between the transmission and received wave is 10 MHz. The beats produced by heterodyne interferometry are sent to IQ demodulators and mixed with 10 MHz reference

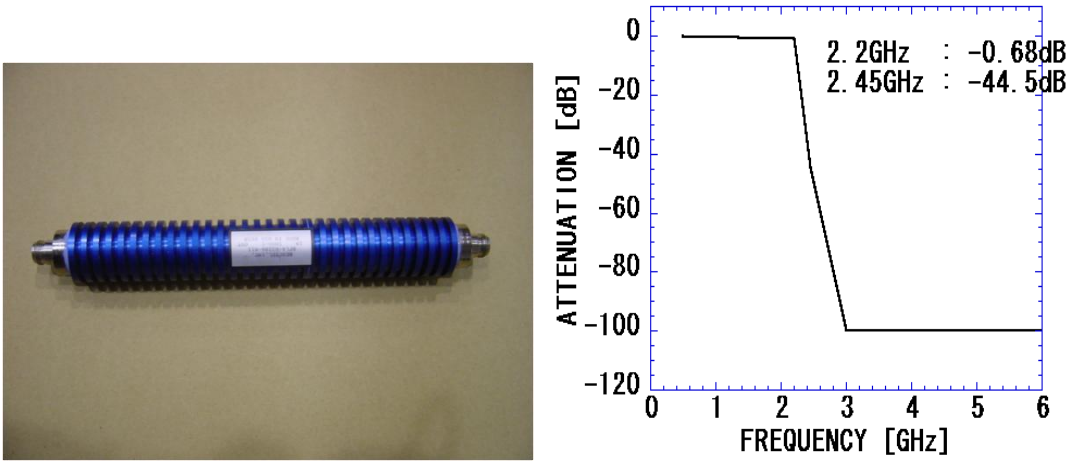

Figure 5.2: Band pass filter

(a)photograph of the filter (b) frequency characteristics

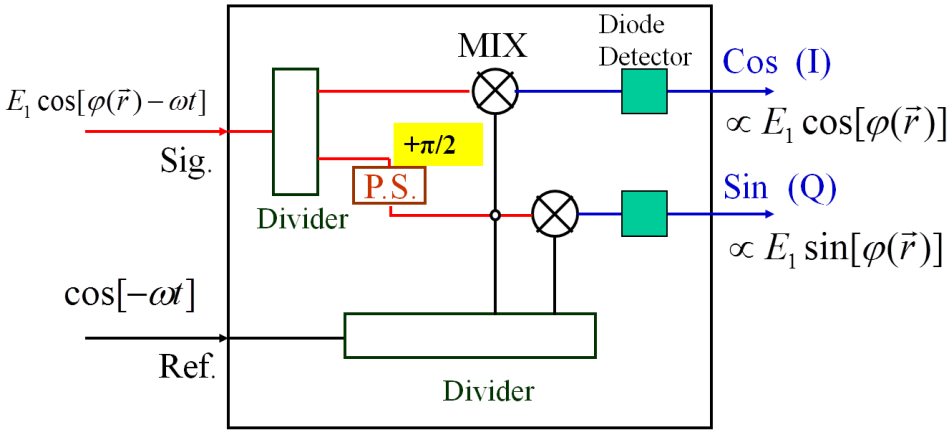

Figure 5.3: Schematic diagram of IQ demodulator

signals. The IQ demodulator output two time-independent signals. The outline of IQ demodulator is shown in Fig.5.3. The output signals have the information of amplitude and phase which depend on only the position of probing antennas.

5.2 EBW Excitation Antennas

As described in Ch.2, to excite the EBW the Slow X (SX) wave has to access to the Upper Hybrid Resonance (UHR) layer. The excitation antennas are directly

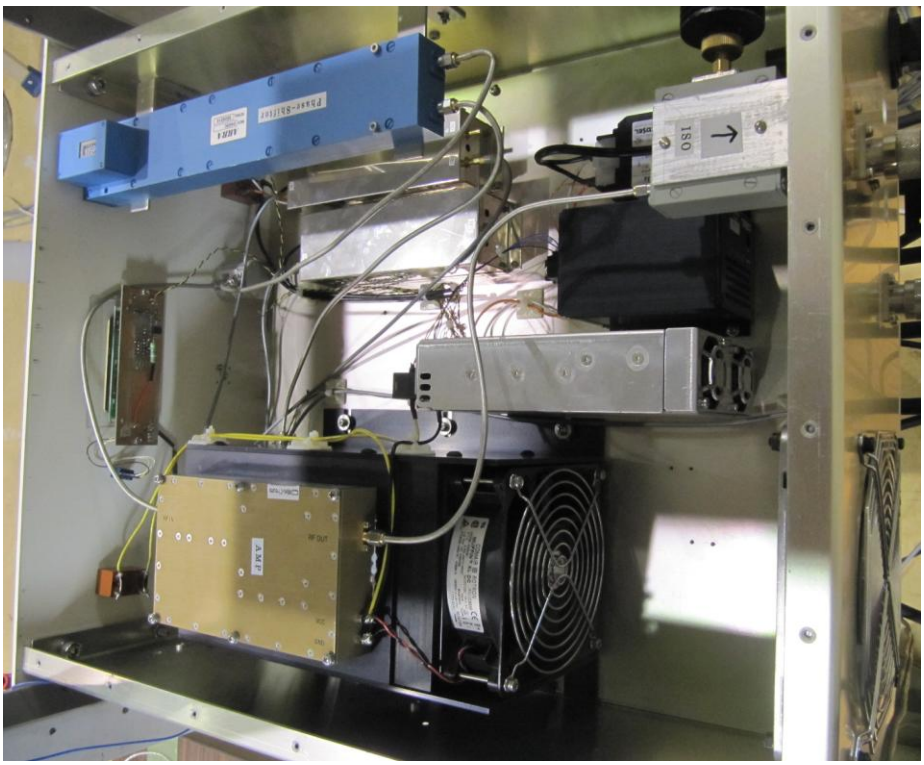

Figure 5.4: The photograph of receiver unit

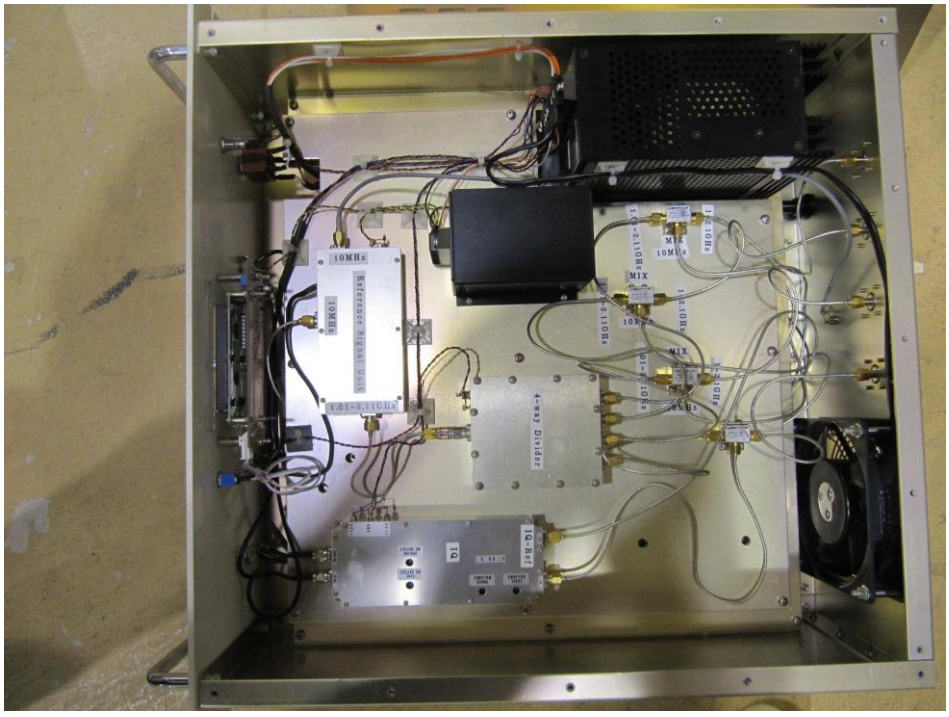

Figure 5.5: The photograph of transmission unit

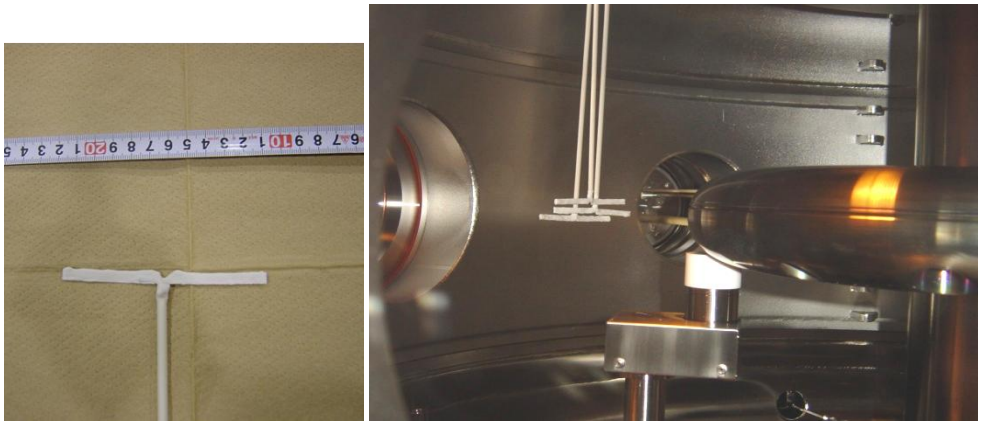

Figure 5.6: Excitation antennas for FX-SX-B conversion

located in the vacuum vessel. Thus, antennas have to be shielded from the charged particles. The mode of the incident waves is determined as initial conditions of electromagnetic oscillating direction. Since the internal coil device Mini-RT has pure poloidal magnetic field, the structure of the magnetic field is relatively simple, compared with other experimental torus plasma devices such as tokamaks and stellarators. Thus, it is easy to excite with aiming at the mode, just having to attend the radiation pattern of the antennas.

Dipole antennas are adopted for excitation antennas because of high polarization selectivity controlled by its direction of the elements with ease. Injection and received signals are transmitted in coaxial cables whose intrinsic impedance is 50 Ω. In vacuum vessel, antennas and semi-rigid coaxial cables are covered with ceramics Al_2O_3. Figure 5.6 shows pictures of excitation antenna. The length of the antenna is 100 mm, which corresponds to $\lambda/2 \sim \lambda/3$ for 1.0 ~ 1.5 GHz microwave.

5.2.1 for FX-SX-B Conversion

For FX-SX-B conversion, the excitation antennas have to be located at low field side, which is corresponding to the outer region in the vacuum vessel. The X wave excitation requires toroidal oscillation of electric field. An ideal single dipole antenna radiates microwaves isotropically in poloidal direction. However, actual

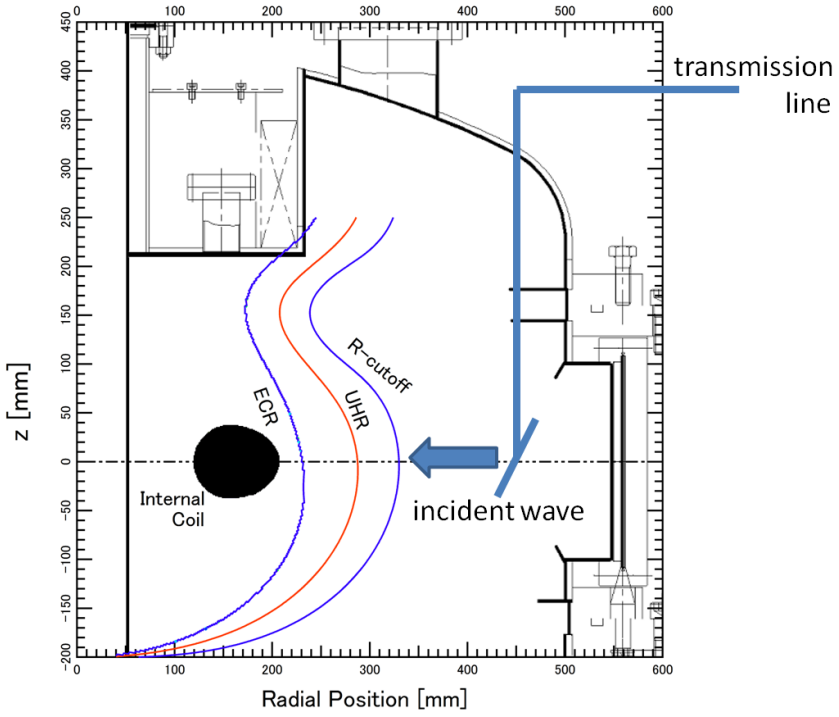

Figure 5.7: Schematic illustration of FX-SX-B conversion

antennas have the width of the elements, so that radiation pattern in poloidal cross section has directivity. To inject microwaves perpendicularly to magnetic field, arrayed dipole antenna is introduced for excitation antenna. A schematic overview of FX-SX-B conversion in poloidal cross section is shown in Fig.5.7. Excitation antennas for FX-SX-B conversion are located at R = 450 mm z = 0 level.

5.2.2 for O-X-B Conversion

As described in Ch.2, to excite the EBW efficiently via O-X-B conversion, accurate injection angle between wave number and magnetic field is required. The O wave corresponds to electric oscillation in poloidal cross section, so that excitation antennas for O-X-B conversion are located so as to align with magnetic field. Injection angle can be adjusted by shifting position of the antenna mechanically. Figure 5.8 shows the relation between injected waves and last closed magnetic surface which is determined by the wall of the vacuum vessel. The injection angle θ

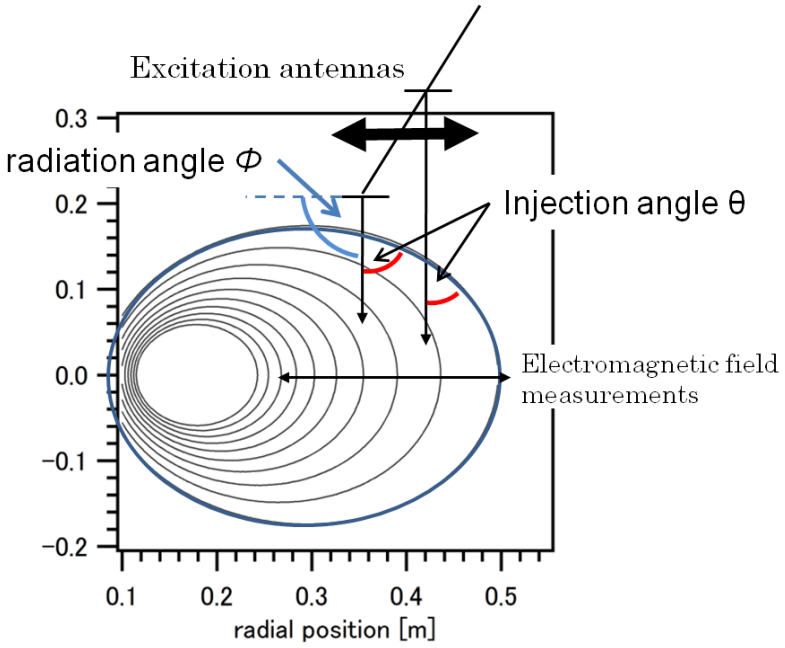

Figure 5.8: The definition of injection angle θ and radiation angle ϕ

is not strictly determined because of extent of microwave radiation. Both the width of main lobe and spatial length of the antenna elements should be narrow, but they do not go together. The more factors of array antenna make the radiation beam width narrow, while the total length of the antenna becomes longer. In this work, the array antenna of three factors is adopted. The radiation intensity of this antenna is approximately written as

$$K = \frac{I_0^2}{8\pi^2\epsilon_0 c}\frac{\cos^2\left(\frac{\pi}{2}\cos\phi\right)}{\sin^2\phi}\frac{\sin\left(\frac{7}{2}kd\cos\phi\right)}{\sin\left(\frac{1}{2}kd\cos\phi\right)}, \tag{5.1}$$

where I_0 and ϕ are amplitude of current profile on antenna elements and angle formed by the element. Figure 5.9 shows the radiation pattern of the antenna, and the radiation intensity of 90 % or more is in the range of ±12°. The distance between excitation antennas and the surface of the plasma is about 15 mm. Thus microwaves are injected mainly in the range of 63 mm on the plasma surface. The injection angle θ is extended as shown in Fig. 5.10.

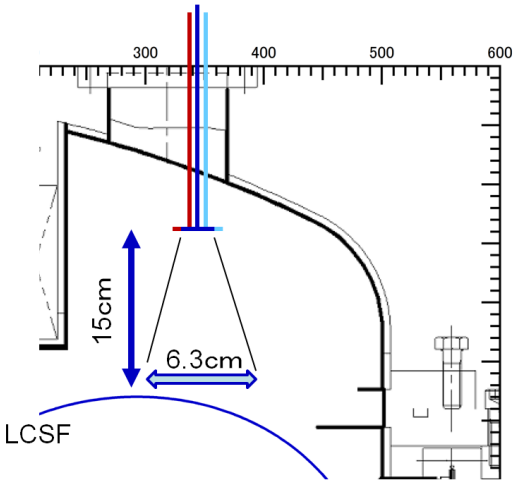

Figure 5.9: Schematic illustrate of propagation patterns

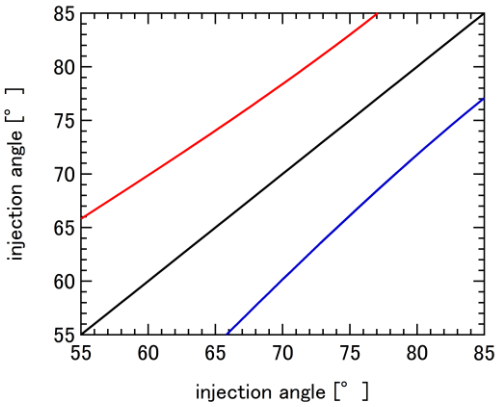

Figure 5.10: Relationship between θ and extended injection angle

5.2.3 for SX-B Conversion

The excitation antenna for SX-B conversion should be located at high field side of the plasma. In the Mini-RT device, high field side corresponds to the center of the vacuum vessel and near the superconductor magnetic coil. The transmission waves are sent in folded semi-rigid coaxial cable covered with Almena ceramic tube to the antenna. Since the antenna has to be located in the core plasma region, the antenna and transmission lines are contrived not to disturb the plasma and magnetic field if possible. Figure 5.11 shows the excitation antenna which is installed as shown in Fig. 5.12.

5.3 Probing Antennas

Inserting antennas enables the direct investigation of waves in plasma. Antennas detect some particular component depending on their characteristics. Thus, the structures and size of antennas let us measure components of the waves selectively.

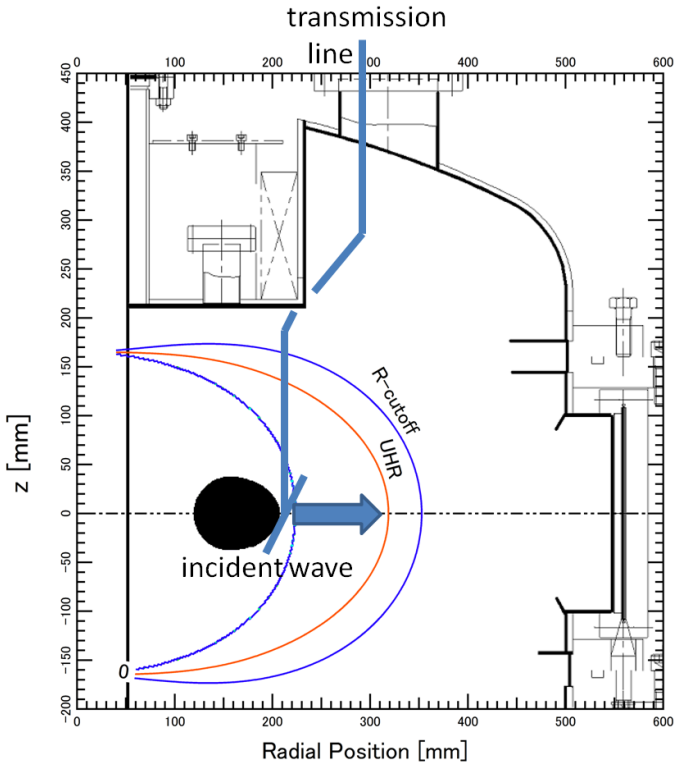

Figure 5.11: Schematic illustration for SX-B conversion

Figure 5.12: A photograph of installed SX-B antenna

5.3.1 Pole Antennas

In common with the excitation antennas, dipole antennas are adopted for probing antennas. The pole antenna emits induced voltage signals by detecting the electric field on its element. The element length should be adjusted to the wavelength of the mode, since the current profile on the antenna determines the signal amplitude. Thus 37.5 mm pole for X-mode and O-Mode waves and 2mm tip for EBWs are installed. The way of antennas corresponds to the electric component of the received waves. The antennas are covered with ceramic just like excitation antennas.

5.3.2 Loop Antennas

The loop antenna emits signals by changing the magnetic flux though its loops. There are several types of loop antennas and one of them shown in Fig. 5.13 is called a King probe [58]. This type probe is immune to noise and do not need baluns [59]. The outer sheath shield the inner signal line from external electric fields, and the generated voltage appears across the central sheath gap [60]. To avoid a lopsided voltage distribution along its loop, the loop used in this work is much smaller than the wavelength. The sheath depth of cupper for 1.0 GHZ microwave is written as

$$\delta = \sqrt{2/\omega\sigma\mu} = 5.8 \times 10^{-7} \quad [\mathrm{m}], \tag{5.2}$$

where σ is the electric conductivity of cupper, $5.96 \times 10^{7}\,\mathrm{m/\Omega}$. Since this value is much smaller than the thickness of the outer conductor, the function of shield is ensured. The shape of a loop is a square 5 mm on a side. The self-inductance of a square loop antenna is written as

$$L = \frac{2\mu a}{\pi}\left(\ln\frac{2a^2}{r} - \ln\left(a + a\sqrt{2}\right) + \sqrt{2} - 2\right) \quad [\mathrm{H}], \tag{5.3}$$

where a and r represent a side length and a radius of an antenna element respectively. Thus, the inductance is 5.04 nH, and the characteristic impedance of

Figure 5.13: Magnetic probing antenna (King probe)

(a) schematic diagram (b) a photograph

the measurement system is 50 Ω, resulting in a time constant of 1.01×10^2 ps. The time constant is about ten times as fast as a period of a diagnostic microwave, so that the skew of waves do not matter so much.

5.4 Triple Probe

Triple probe is installed to measure radial electron density and temperature profiles in the Mini-RT. It is a kind of Langmuir probe which has three probes. This measurement method enables us to obtain electron temperature and density without sweeping bias voltage [61]. Figure 5.14 show a photograph of the triple probe. The tips of them are made of tungsten and length and diameter of them are 5 mm and 1.5 mm, respectively. Figure 5.15 shows the schematic diagram for triple probe. The biased voltage between two probes is DC 90 V, and this value is assumed to be sufficiently large to repel electrons at probe3. Then electron temperature can be approximately obtained;

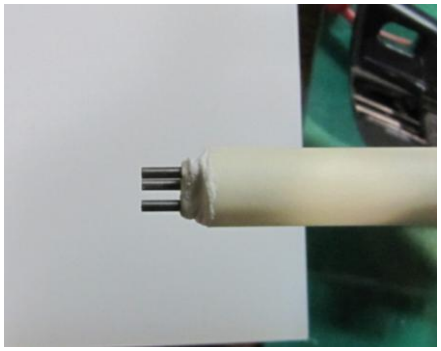

Figure 5.14: Tip head of triple probe

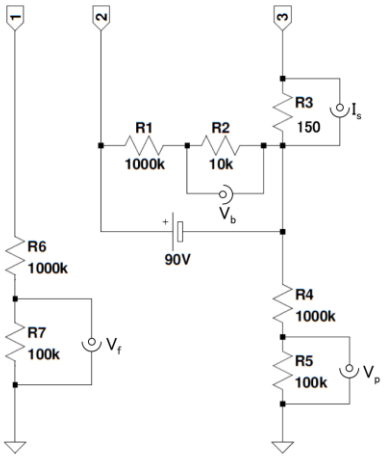

Figure 5.15: Schematic diagram fro triple probe measurement

$$\kappa T_e = \frac{e(V_1 - V_2)}{\ln 2} \tag{5.4}$$

$$I_{is} = 0.61 S e N_e \sqrt{\frac{k T_e}{m_i}}, \tag{5.5}$$

where S denotes surface area of probe tip.

Chapter 6
Experimental Results

In this chapter, experimental results of electromagnetic field measurement are described. The electromagnetic field profiles are separated into each component, i.e. electromagnetic, electrostatic and oscillating directions, and they show waveforms and wave characteristics. The EBWs characteristics to focus attention on are as follows; 1) EBWs have no cutoff density, 2) they are electrostatic-mode waves, 3) they are excited by mode conversion from electromagnetic waves in plasma, 4) their typical value of the wavelength is of the order of the Larmor radius. 5) they are longitudinally polarized, 6) they are backward wave mode (they have negative group velocity), and 7) their group velocity is in the range of the electron thermal velocity. We are trying identifying the EBWs by collating these characteristics with wave properties in experimental results.

6.1 FX-SX-B Conversion

6.1.1 Wave Forms

The results of FX-SX-B conversion are described in this section. This conversion requires steep gradient of density profile. As described in Ch. 3, the density profiles in the Mini-RT can be changed easily by applying levitation coil current. Figure 6.1 (a) shows electron density profile and Fig.6.1 (b) does temperature profile measured by triple probe, when internal coil current was 34 kA-turns and levitation coil current was 15 kA-turns. The levitation coil current makes a steep slope of electron density profile, while electron temperature profile

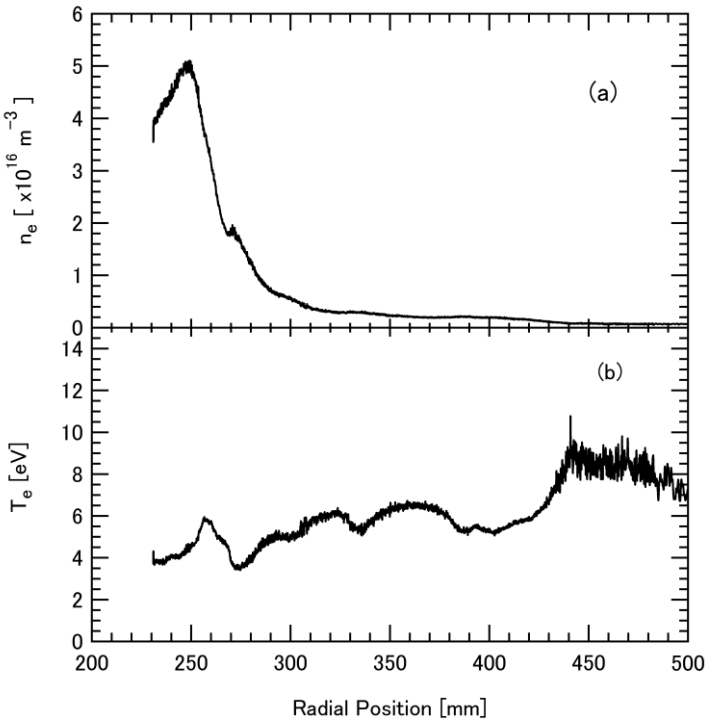

Figure 6.1: Electron density and temperature profile measured by triple probe. (a) shows electron density profile, and does (b)electron temperature profile.

has nearly constant value about 6 eV. A diagnostic microwave at 1.0 GHz and 10 W was injected from low field side into this plasma which was produced by the microwaves at 2.45 GHz and 2.0kW. Several specific density curves for 1.0 GHz microwave in the magnetic profile of the Mini-RT are plotted in Fig. 6.2. This figure shows the cutoff layer as an intersection point between density profile and the curve. Thus, the R-cutoff is located at major radius R = 286 mm, the UHR is done at R = 282 mm, the P-cutoff is done at R = 280 mm and L-cutoff is done at R = 274 mm, respectively. The electromagnetic field profiles measured by probing antennas are shown in Fig. 6.3, where

(a) radial component of electric field measured by tip pole antenna (Ex),

(b) toroidal component of electric field measured by 35 mm dipole antenna (Ey),

(c) poloidal component of electric field measured by 35 mm dipole antenna (Ez)

and

(d) poloidal component of magnetic field measured by 5mm loop antenna (Bz),

respectively. The amplitude of the wave is a function of antenna element length or

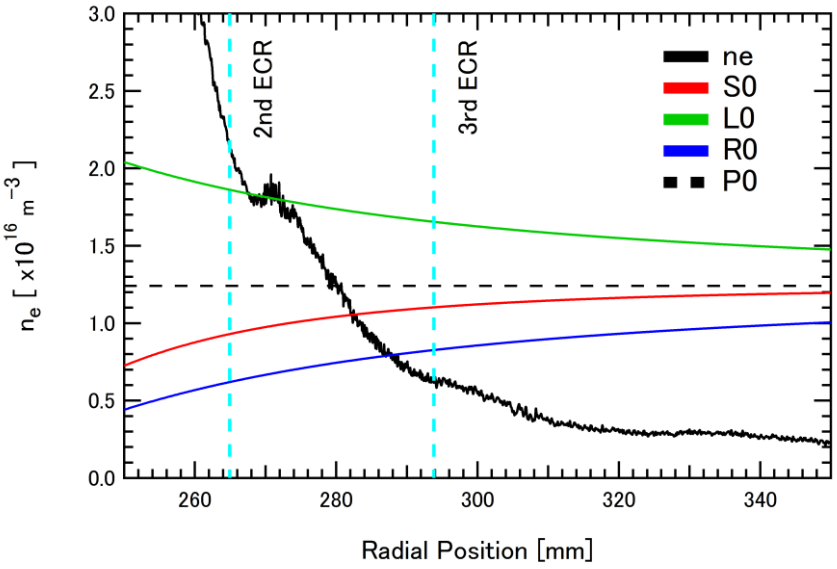

Figure 6.2: Specific density lines

The intersection point represents the location of cutoff or resonance layer.

its structure and the absolute value cannot be obtained with the circumstances, so that the vertical axis in Fig. 6.3 is applied arbitrary unit to. In this experiment, diagnostic X wave was injected perpendicularly to the magnetic field and toward the center of the device, so that Ex component corresponds to longitudinal polarization. Similarly, Ey and Bz component do to the X mode polarization and Ez do to O mode polarization, respectively. In addition, the blue lines and red lines show sine and cosine component, respectively. Here, radial profiles are divided into two regions by its plasma frequency. One is the lower density plasma region where $\omega_{pe} < \omega$, and the other is core plasma region where $\omega_{pe} \geq \omega$. The electromagnetic field measurements in Figs. 6.3 (b), (c) and (d) show a long-wavelength mode in the lower density region. This corresponds to an electromagnetic wave mode excited by excitation antennas on the outside of the plasma. In radial electric field measurement, shown in Fig. 6.3 (a), a short-wavelength mode is observed in the core plasma region. The wave in this mode propagates in the evanescent region over the cutoff layers, and is excited around the UHR region. The wavelength evaluated from the waveforms is around 20 mm, which exhibits a refractive index of ~ 15. In this era, electromagnetic mode waves are damped down, which suggests that the short-wavelength mode wave

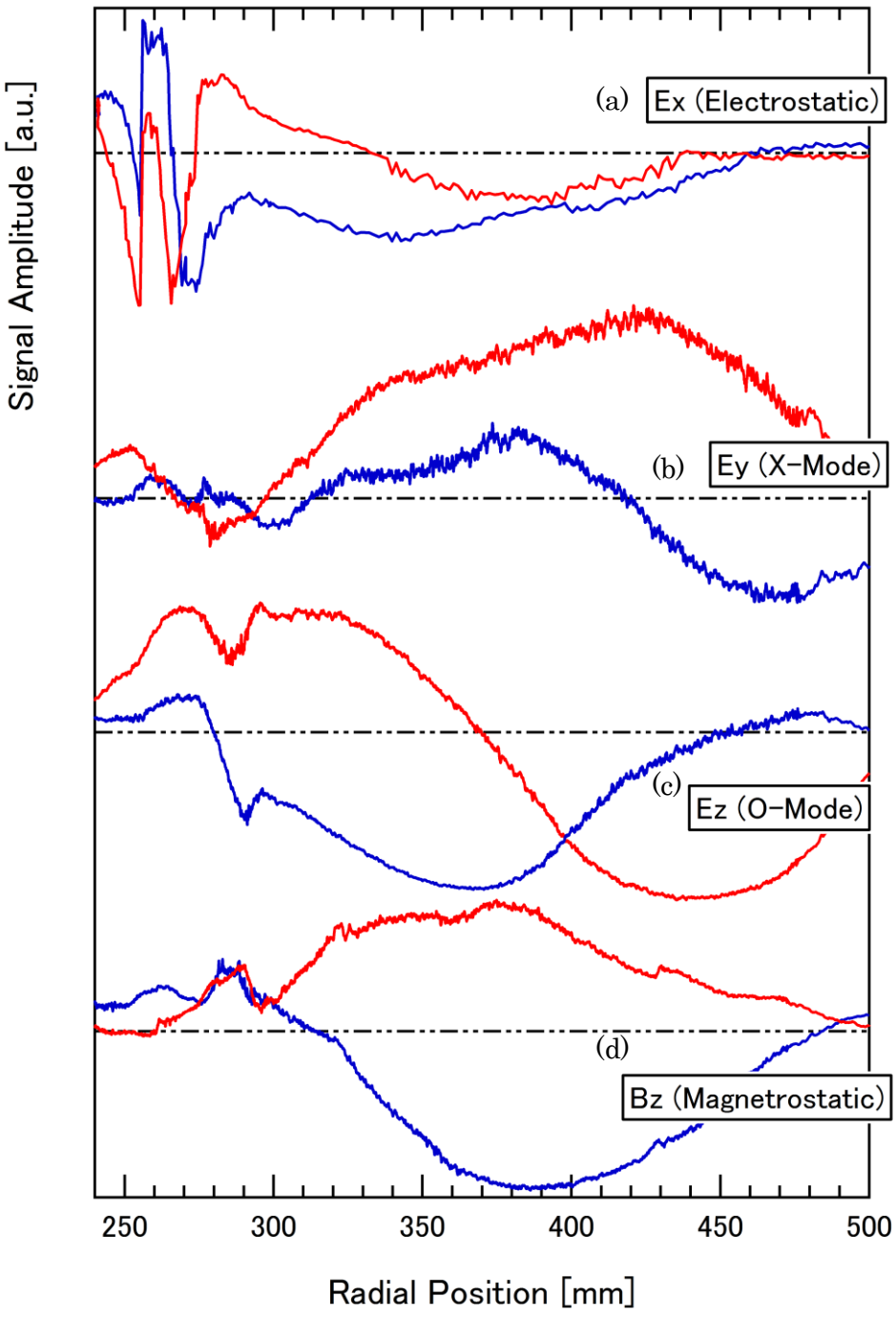

Figure 6.3: Electromagnetic field profiles for 1.0 GHz microwaves.

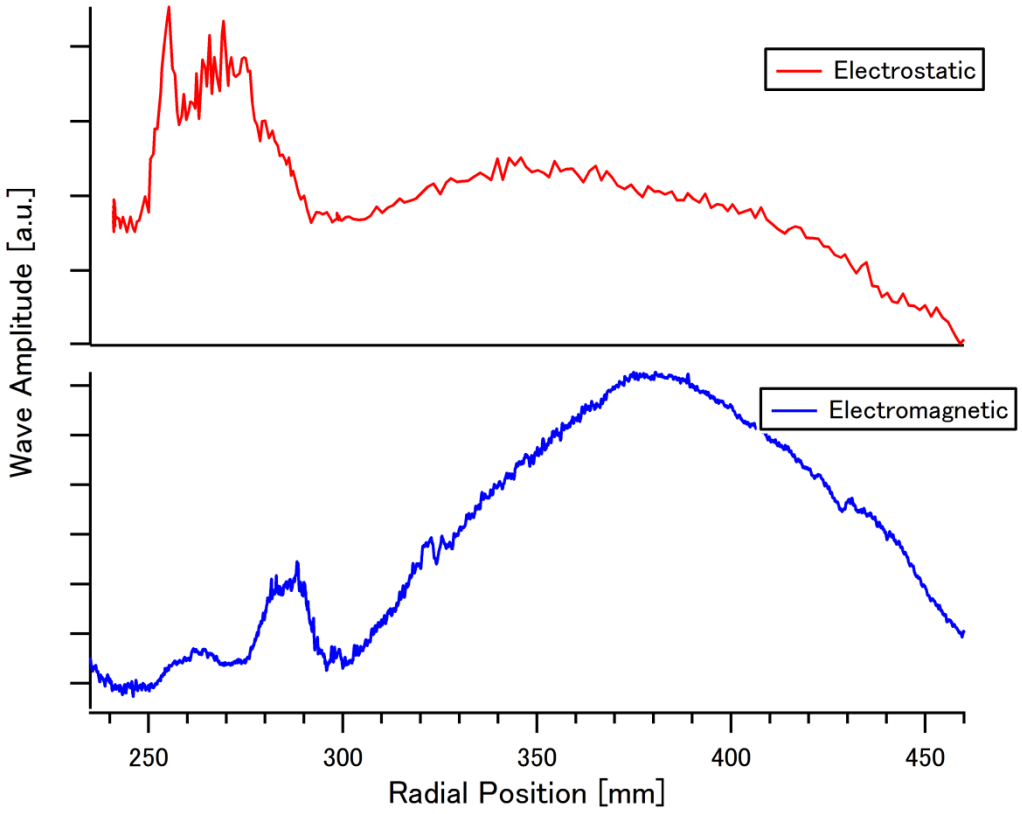

Figure 6.4: Amplitude profiles of electrostatic and electromagnetic component

shown in Fig.6.3 (a) are electrostatic mode waves excited by conversion from electromagnetic mode waves.

6.1.2 Amplitudes and Phases

IQ signals give us signals containing information on the amplitude and phase of the electromagnetic field. Amplitude is obtained as sum of squares of sine and cosine component, i.e. assuming the sine and cosine component are written as $X = A\sin\phi$ and $Y = A\cos\phi$, then $A^2 = X^2 + Y^2$. Figure 6.4 shows the profiles of amplitude of electrostatic (Fig.6.3 (a)) and electromagnetic (Fig.6.3 (d)) component. Although electrostatic and magnetic component cannot be compared directly, Figure 6.4 shows the relative variation of amplitude in each component. Since the

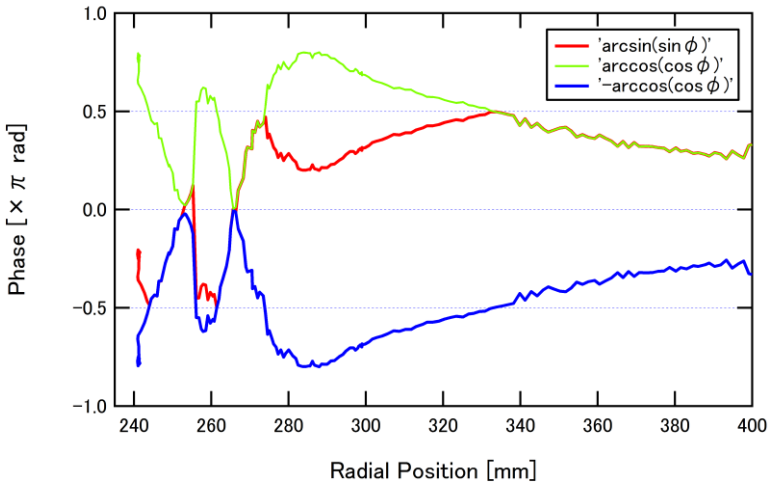

Figure 6.5: Phase profiles of electrostatic components

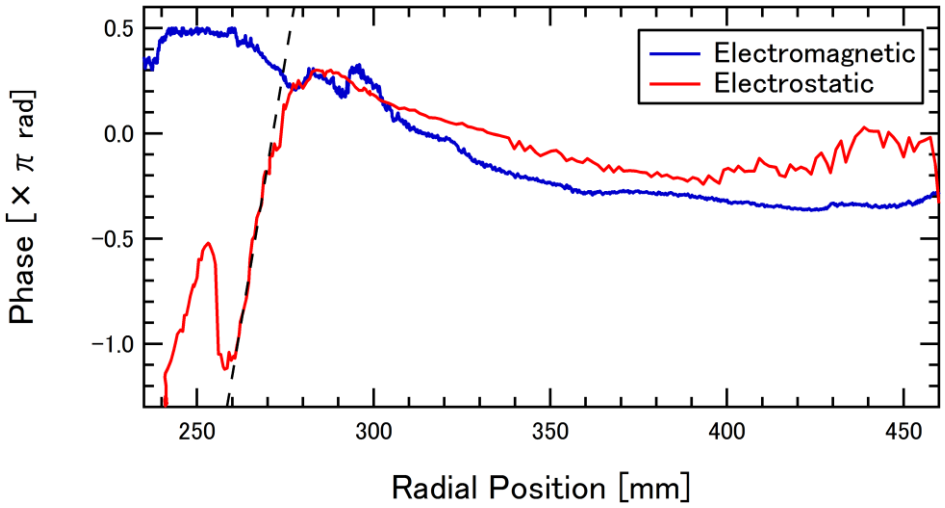

Figure 6.6: Phase profiles of electrostatic and electromagnetic component

Phase profiles are plotted by combination of arcsine and arccosine. The gradient of the tangential line give wave number and the refractive index of 15.

excitation antennas are located at a remove from the measurement line, the conductivity of the vacuum vessel wall cancels out the electromagnetic field at R = 500 mm, where probing antennas act as shielded. Thus, the waves end up like a standing wave between two reflections; at cutoff layer in the plasma and at vacuum vessel wall.

Phase profiles are also obtained by taking inverse function, that is $\phi = \sin^{-1}(X/A)$ *or* $\cos^{-1}(Y/A)$. Since the phase can be arbitrary value, it is

necessary to attend to the domain of inverse function. Figure 6.5 shows phase profiles of electrostatic component. We cannot distinguish $\sin\phi$ from $\sin(\pi-\phi)$ and $\cos\phi$ from $\cos(-\phi)$. Thus, a phase profile is determined by apposed inverse functions so as to be a connected gentle curve. A phase profile comparison between electromagnetic component and electrostatic component is shown in Fig. 6.6. The phase is a function of the spatial position and length of the transmission lines, so that the gradient of the phase profile gives the wave number vector. The figure confirms a reversal of the phase gradient around the UHR in the electrostatic mode wave. This suggests a change in the direction of the phase velocity, and Fig. 6.6 shows that the phase velocity at R < 255 and 260 < R < 280 is opposite to that in other regions. Thus, this electrostatic wave is a backward wave. In addition, the wave number, which is read from the tangential line plotted as the broken line in the figure, is 0.10 π mm^{-1}. It corresponds to refractive index of 15, which coincides with the value estimated from the waveform.

6.1.3 Dispersion Relation

Figure 6.7 shows the radial profile of the refractive index, which is calculated by solving the dispersion relation with the measured parameters and magnetic profile. The refractive index profile of the EBW is greater than 100, i.e. their wavelength is less than 3 mm, whereas experimentally observed wavelength is somewhat smaller (20mm). However, spatial properties coincide with experimental results. The drastic change of phase gradient in electrostatic component occur at the location of the UHR (R = 285 mm), where the SX waves are converted into EBWs. The SX mode contains electromagnetic component, so that amplitude profile of electromagnetic component has a local maximal value around the UHR.

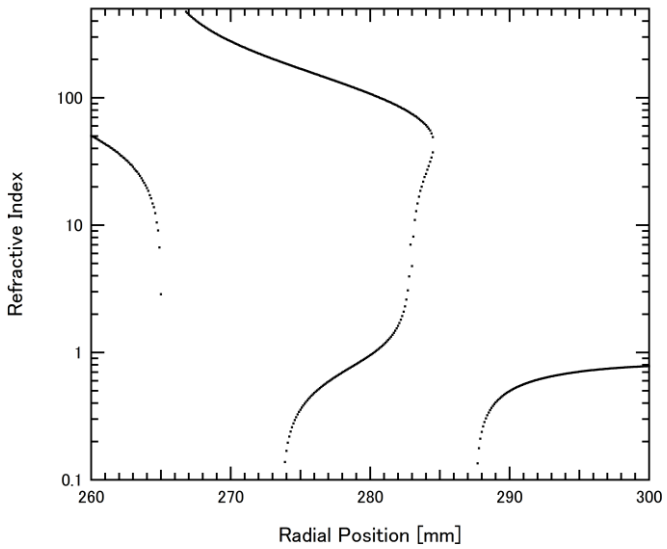

Figure 6.7: Perpendicular refractive index profile for 1.0 GHz X waves

To solve the dispersion relations, the smoothed density profile and a certain amount of T_e ~ 10 eV are substituted.

6.1.4 Configuration and Frequency Dependence

Figure 6.8 (a) shows another density profile, which has slightly moderate density gradient. This configuration is made by 35.9 kA turns of internal coil and 13.6 kA turns of levitation coil current, and the plasma is produced by 2.0 kW microwaves. Figure 6.8 (b), (c), (d) and (e) show longitudinal polarized waveform in this configuration for 1.0 GHz (b), 1.1 GHz (c), 1.2 GHz (d) and 1.4 GHz (e), respectively. In Fig.6.8 (b)–(e) short-wavelength mode waves appear, and the most noticeable one is for 1.1 GHz diagnostic microwaves. Their phase profiles are shown in Fig.6.9. The refractive indexes estimated from tangential line of phase profile are 17 for 1.1 GHz and 15 for 1.5 GHz. These values are an order of magnitude smaller than that of dispersion relations of the EBW. Figure 6.10 shows specific density curves of R-cutoff and the UHR, similarly to Fig. 6.2. The higher the incident frequency becomes, the higher density region the short-wavelength mode is excited at. As described in Ch. 2, the mode conversion efficiency of FX-SX-B conversion is estimated by tunneling parameter η ,which is a product of the wave number in vacuum and the distance between R-cutoff and the UHR. The relationship between

the location of the specific layers and appearance of phase reverse and tunneling parameters for each frequency is summarized in table 6.1.

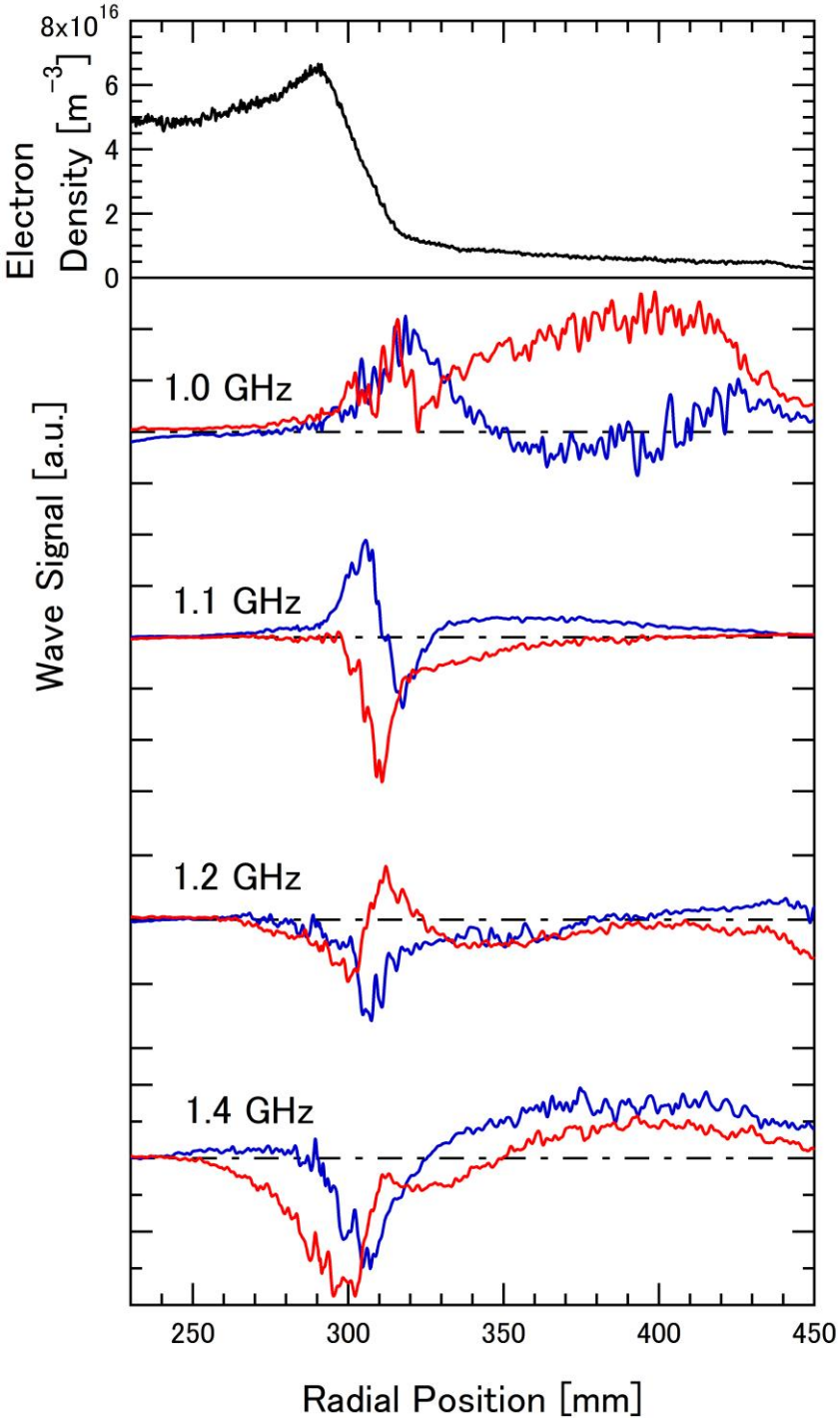

Figure 6.8: Electron density and electrostatic components under several injection frequencies

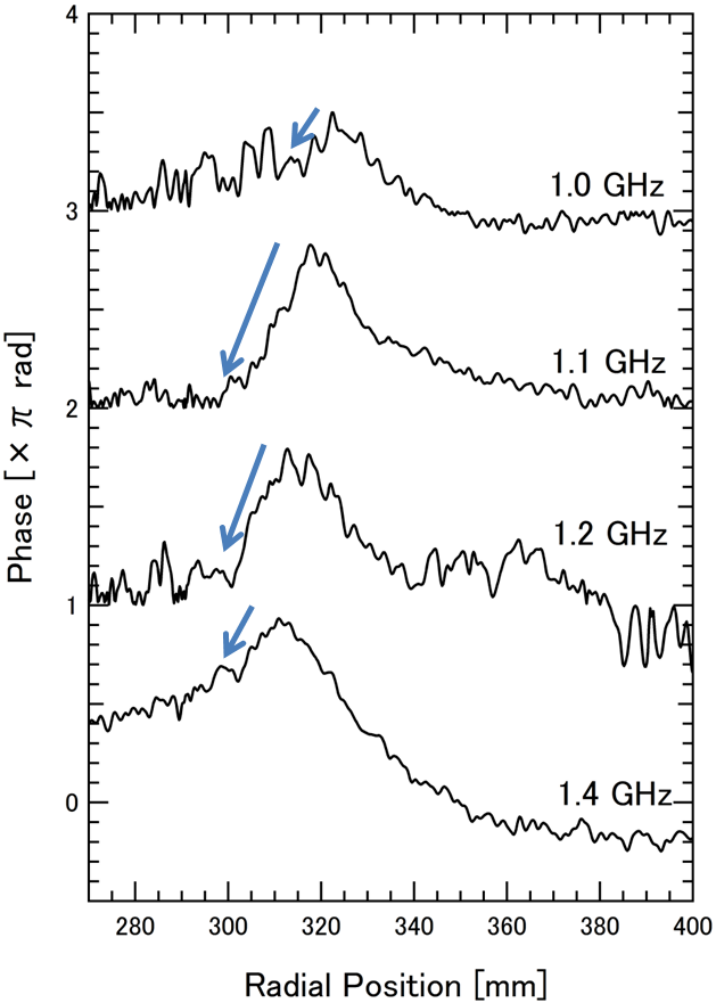

Figure 6.9: Phase profiles under several injection frequencies

Table 6.1 Relationship between frequencies and locations of the UHR

frequency	Rcutoff	UHR	Phase reverse	η
1.0	286	282	282	0.0816
1.0	334	322	323	0.0628
1.1	322	317	316	0.0801
1.2	317	315	312	0.0628
1.4	312	310	310	0.0753

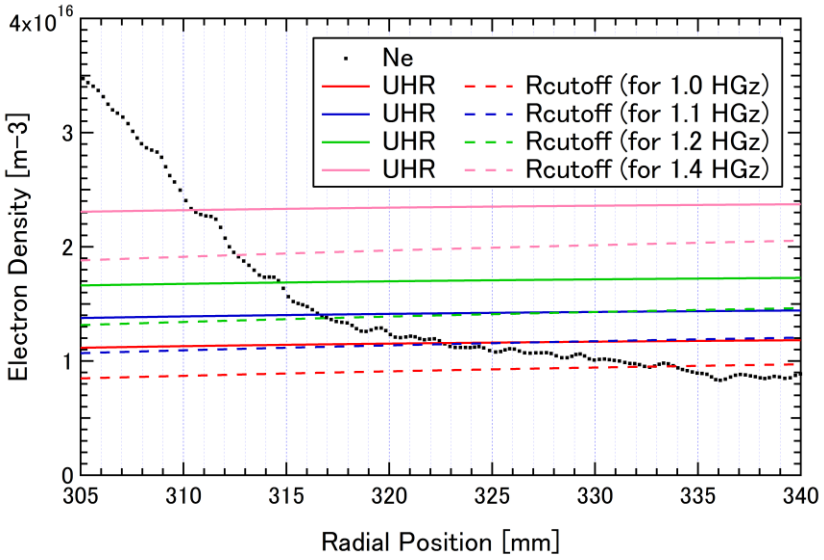

Figure 6.10: Specific density curves for several frequencies

6.2 O-X-B Conversion

6.2.1 Wave Forms

O-X-B conversion contains two conversion processes, i.e. the first transition from O mode to X mode and the second one from SX mode to EBW mode. At first, obliquely injected O mode has its polarization in the poloidal cross section. After the O-X conversion, the incident wave mainly has ellipsoidal polarization in a plane which is perpendicular to the magnetic field. Finally, the injected wave is converted into the EBW which is polarized longitudinally. Radial profiles of electromagnetic field show these variations of polarization.

Figure 6.11 (a) and (b) shows the density profiles measured by the triple probe, when the internal coil current is 27.6 kA turns without applying levitation coil current, respectively. In this case, incident waves are O-mode, so that the P-cutoff layer is located at R = 320 mm. Figure 6.12 shows the waveforms; they are wave signals of electromagnetic component measured by magnetic loop antenna directed at toroidal direction, and electrostatic component measured by tip pole antenna directed at radial direction, respectively. Diagnostic microwaves are

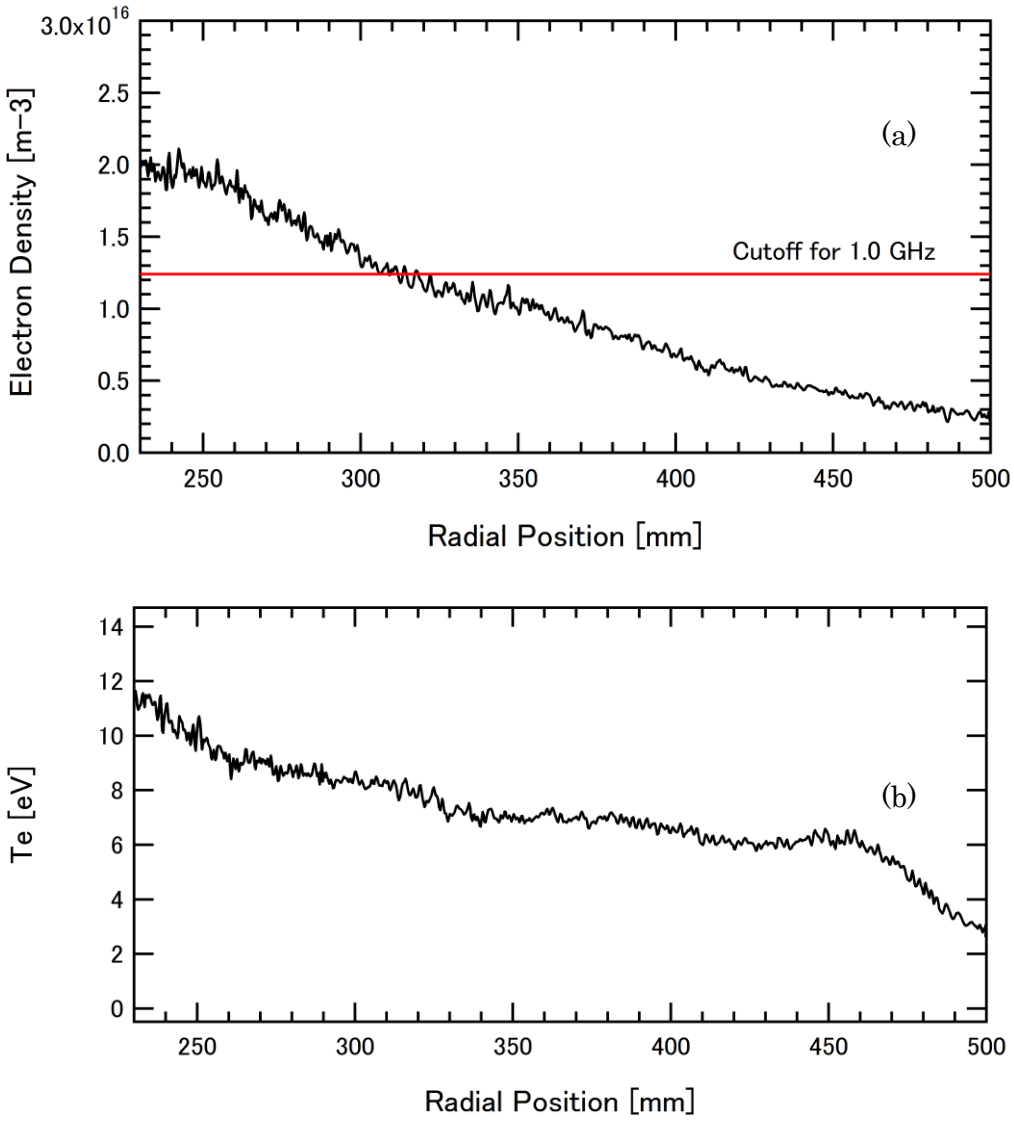

Figure 6.11: The electron density and temperature profiles for O-X-B conversion

injected from top of the vacuum vessel with O mode. The diagnostic microwaves at 1.0 GHz and 10W are injected with the injection angle $\theta = 71.1°$. The UHR is located in the outer region of the core plasma. Similarly to the FX-SX-B conversion, a short wavelength mode is observed in radial electrostatic measurement at the core plasma region, as shown Fig. 6.11 (b). The wavelength of this mode is estimated 15 mm from the waveform and this value corresponds to refractive index of 20. On the other hand, electromagnetic component, as they are shown in Fig. 6.11 (a), waves are damped down at the region. In the outer region, where the density is lower, the

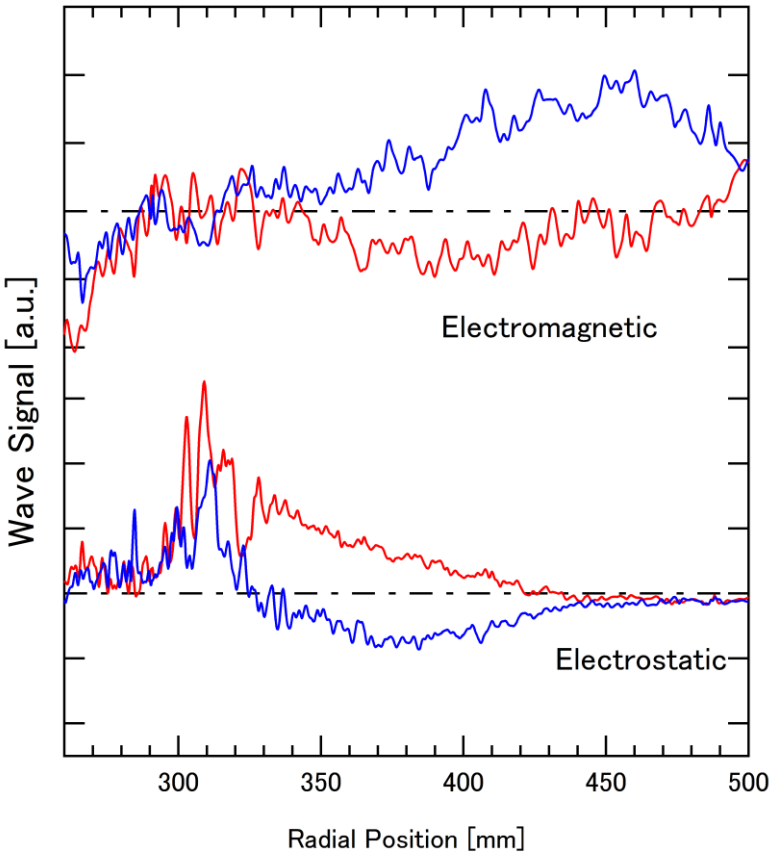

Figure 6.12: Comparison of waveforms between electromagnetic components and electrostatic ones.

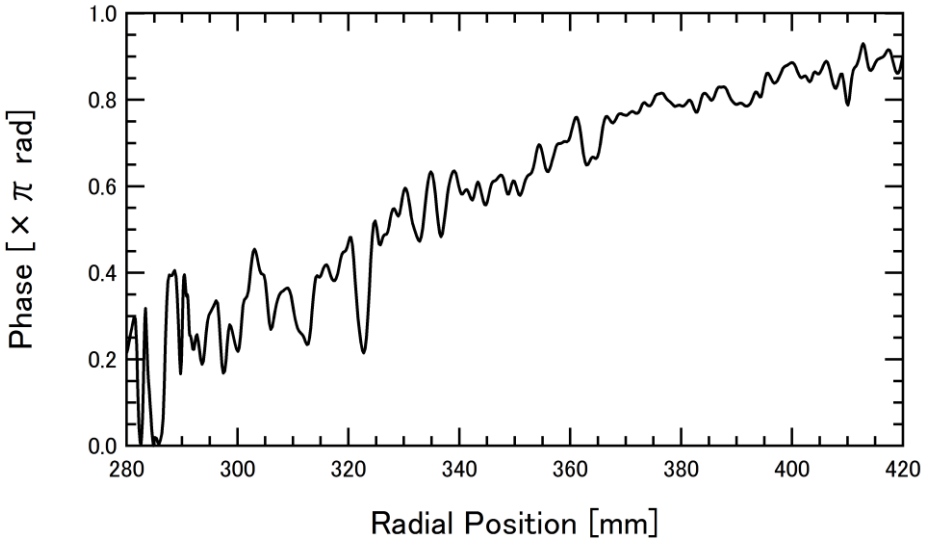

Figure 6.13: Phase profiles of electrostatic component

There is no drastic change of gradient of the phase profile

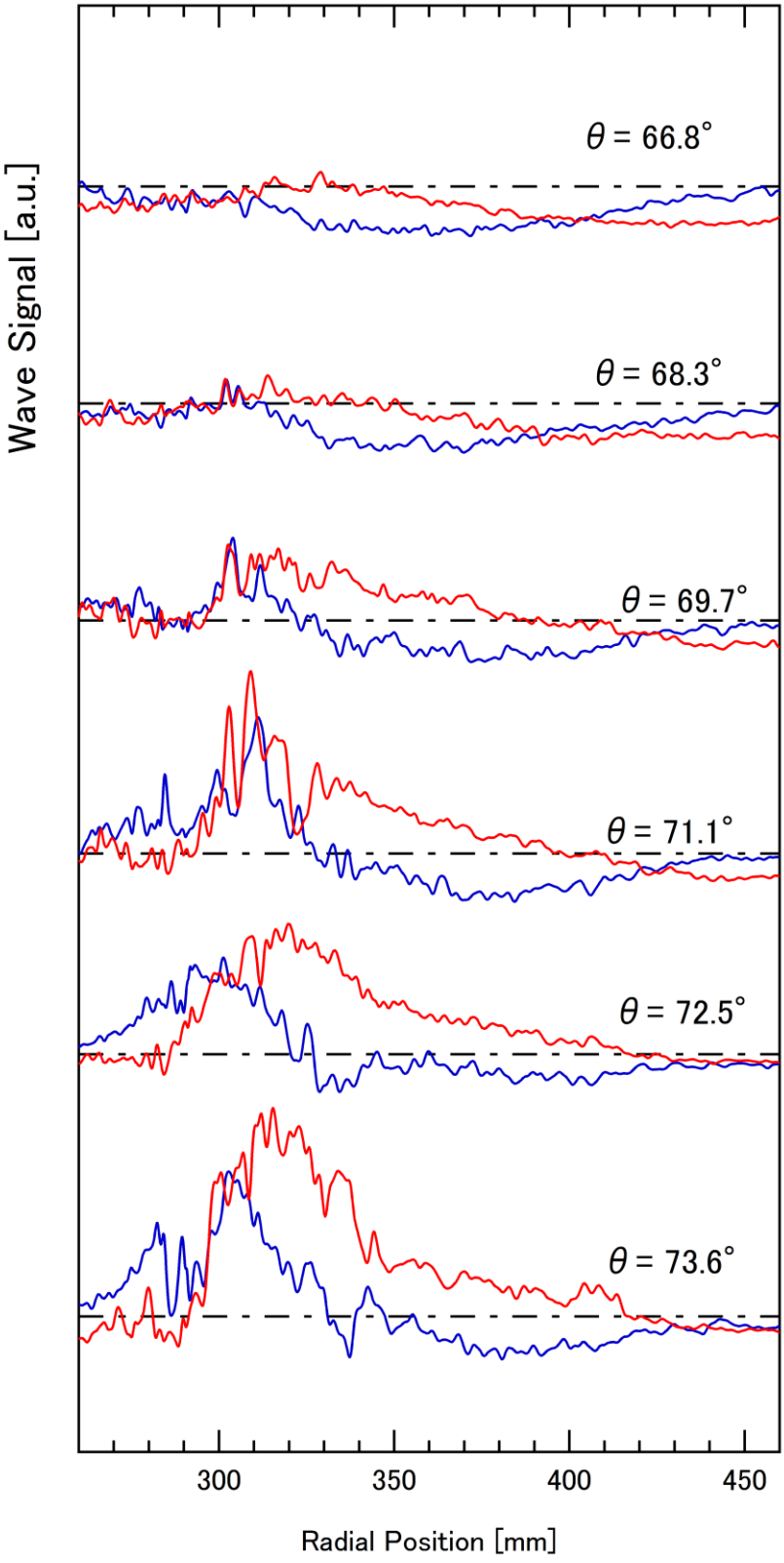

Figure 6.14: Variation of waveform with different injection angle

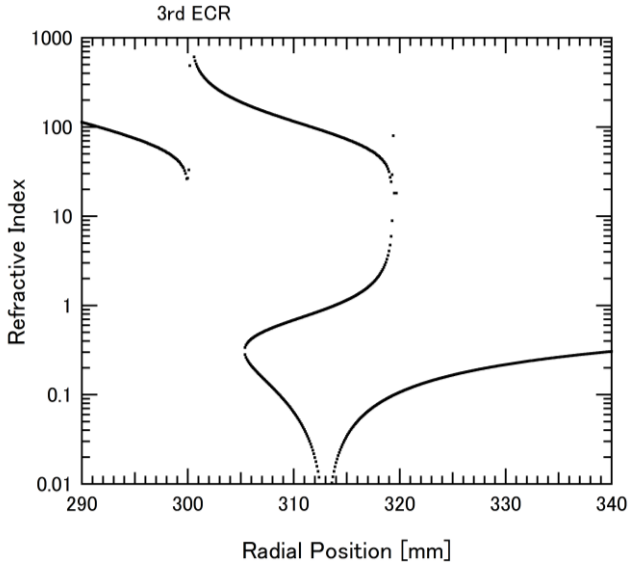

Figure 6.15: Dispersion relation for oblique O mode at optimal angle

waves of all the components show the long wavelength mode. These characteristics obtained only when θ is 71.1°. If the injection angle slightly differs from this value, the short-wavelength mode cannot be observed. The waveforms of the short -wavelength mode collapse with differing from $\theta = 71.1°$. The phase profiles of them are shown in Fig. 6.12 by taking the inverse function. A drastic reverse of the phase gradient cannot be observed, although the wavelength becomes shorter. However, as mentioned, this short-wavelength mode does have the dependence on injection angle. Figure 6.14 shows the variation of waveforms with alternation of injection angle. We cannot obtain the absolute value of the amplitude with this apparatus, but in obvious, these wavelength and amplitudes are changed at the core plasma region. It is only at $\theta = 71.1°$ that the short-wavelength mode is observed, and no drastic change of the gradient of phase profile is observed at any injection angle.

Figure 6.15 shows the perpendicular refractive index profile for 1.0 GHz with keeping optimal value of parallel component. The density profile shown in Fig. 6.11 (a) and magnetic field give us the optimal angel $\theta = 68.8°$. Similarly to the FX-SX-B conversion, the refractive index obtained from dispersion relation is about one order larger than that from experiment. In addition to the information of wavelength, the dispersion relation shows that four modes can exist near the UHR

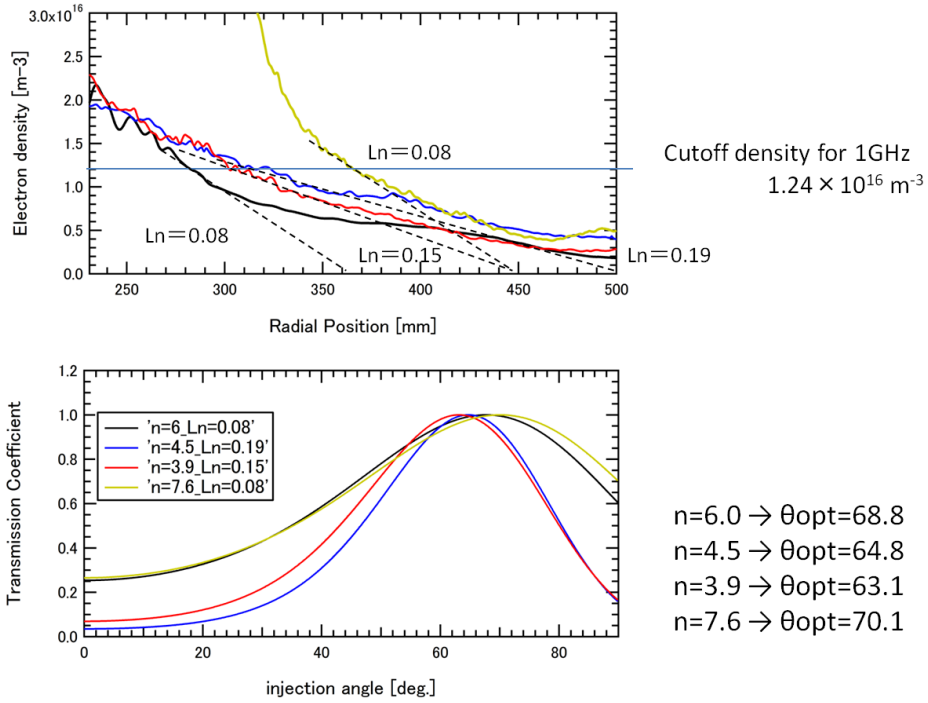

Figure 6.16: Density profiles and conversion coefficient curves.

Here, "n" denotes the ratio of frequencies between injected microwaves and electron cyclotron at the plasma cutoff layer.

layer, i.e. injected O waves, SX waves converted from O mode, SX waves propagating toward the UHR and the EBWs converted from SX mode. Thus, waveforms in this region seem to be superimposed state. This overlap prevents us from evaluating phase profiles by taking the inverse function of the waveforms.

6.2.3 Configuration Dependence

In the O-X-B conversion, optimal injection angle is determined by density profiles and magnetic field. The EBW excitation experiments via O-X-B conversion were carried out in several density profiles. Figure 6.16 shows the electron density profiles and these density gradient lengths at each P-cutoff layer. The density gradient length and strength of magnetic field at the P-cutoff give us the conversion efficiency and optimal injection angle, as shown in Fig.6.16, by using Eq. (2.66) and (2.68). Figure 6.17 shows the variation of waveforms with different injection angle in the case where optimal angle is 64.8°. The short-wavelength mode laps over the

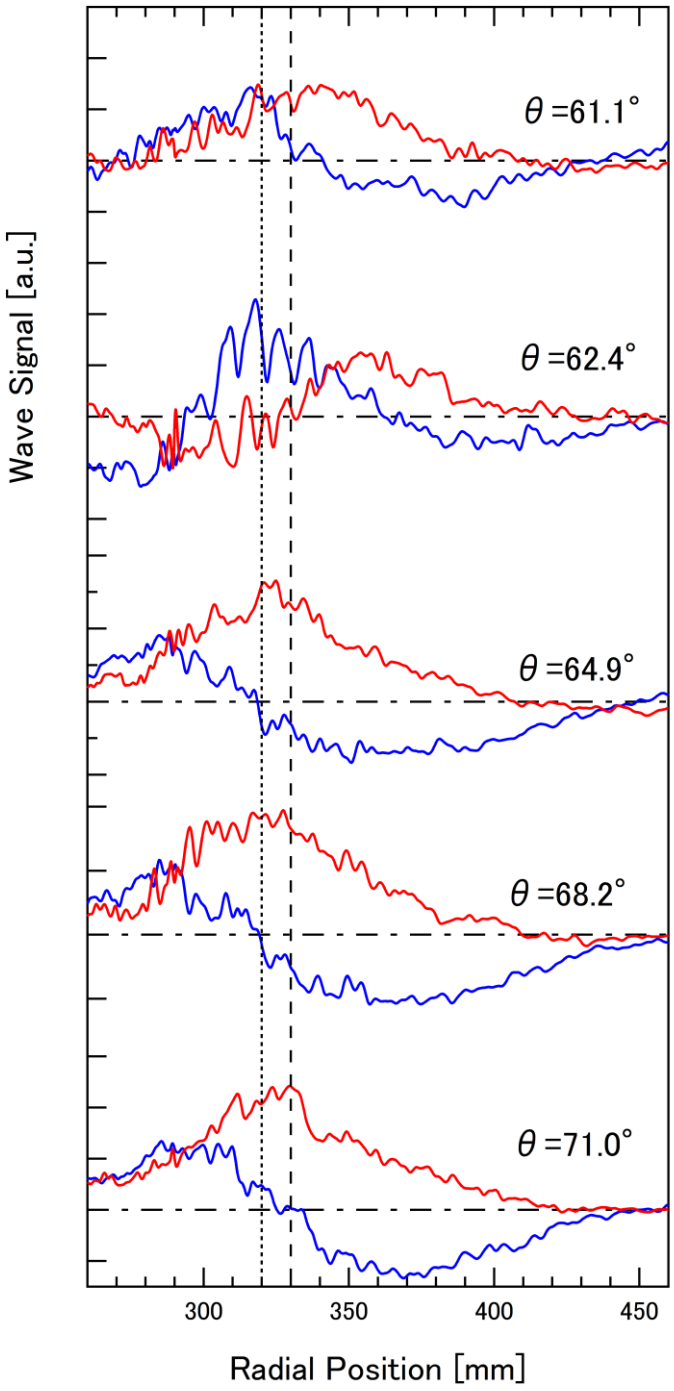

Figure 6.17: Variation of waveforms with different injection angle when the optimal angle is 64.8 degree.

The dot line and broken line show the location of the P-cutoff layer and the UHR respectively.

long wavelength mode only when the experimental injection angle is 62.4°. The relationship between optimal angle and experiment is shown in Fig 6.18. Error bars in this figure is evaluated as extent of conversion efficiency and injected microwaves. Experimental results not necessarily coincide with the expected line because of paucity of available data and length of error bars. However, it may be said that the result is showing a certain constant relationship between excitation of the short-wavelength mode and initial injection angle of incident microwaves. Dependence on the oblique injection angle is an important property of O-X conversion and having this dependence suggests injected microwaves are converted into SX mode that have the blanch connecting the EBW mode.

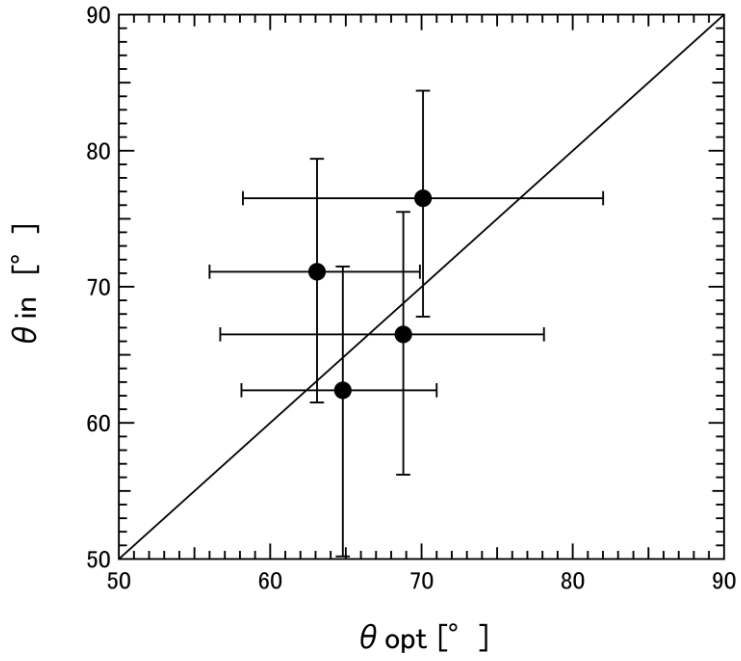

Figure 6.18: Relationship between theoretical optimum and experimentally obtained injection angel about the O-X conversion

6.3 SX-B Conversion

6.3.1 Wave Forms and Dispersion Relation

As described in Ch. 2, in SX-B conversion, it is necessary to restrict the density profile so that the L-cutoff layer does not appear between excitation antenna and the UHR layer. In addition, the frequency of the incident X waves has to be lower than the electron cyclotron frequency. EBW excitation experiments were carried out, paying these limitations.

Figure 6.19 shows the density profile and wave signals. This configuration was made by 35.9 kA-turns internal coil current without applying levitation coil current. In the toroidal electric measurement, shown in Fig. 6.19 (c), a long-wavelength mode is dumped down around R = 300 mm, whereas in longitudinal electric field measurement, shown in Fig. 6.19 (b) a short-wavelength mode is excited in the region of $260 < R < 300$. A phase profile of Fig. 19 (b) is plotted in Fig. 6.20. In this figure, the reverse of the phase gradient is not observed. The refractive index estimated from tangential line of the phase profile is about 3.8, and the refractive index profile, which is calculated by solved dispersion relation, is shown in Fig. 6.21. The UHR is located at R = 265 and L-cutoff does not appear. Although the refractive index of EBW is slightly smaller than that of the previous two conversion cases because of lower density, it is at least, about 20 ~ 30 near the UHR. On the other hand, in the case of improper condition for SX-B conversion, i.e. the density is enough high to appear the L-cutoff layer between the excitation antenna and the UHR. The case that L-cutoff layer prevents incident SX waves from reaching the UHR is shown in Fig. 6.22. Both waves electromagnetic and electrostatic component are damped down immediately and cannot propagate toward the UHR layer, because the injected microwaves burst into the evanescent region right after the launching from the excitation antenna. The refractive index profile obtained by solving dispersion relation with this density profile and magnetic field is shown in Fig. 6.23. The evanescent region lies between the antenna and the L-cutoff layer which is located at R = 300 mm.

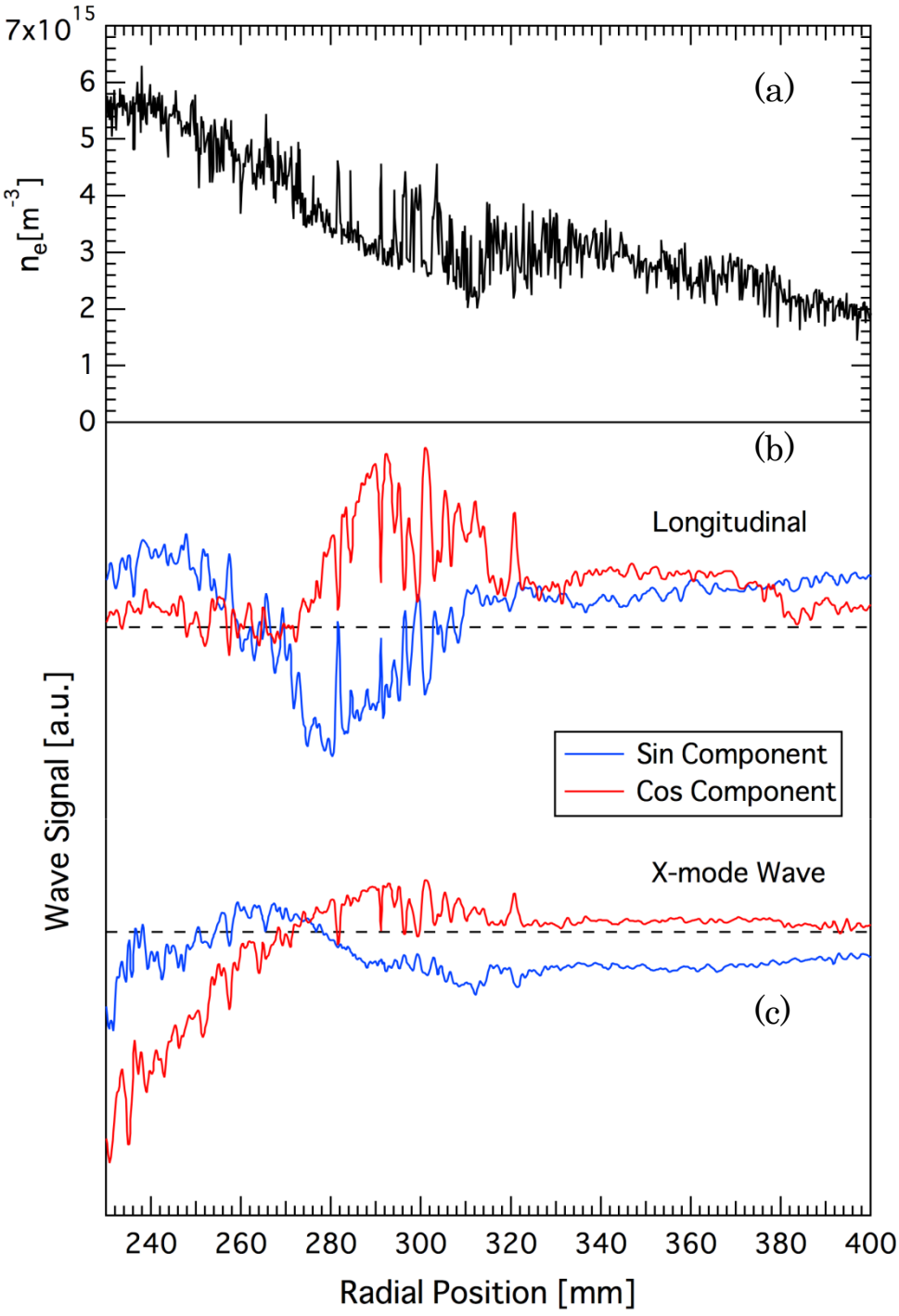

Figure 6.19: Short-wavelength mode excitation via high filed X injection

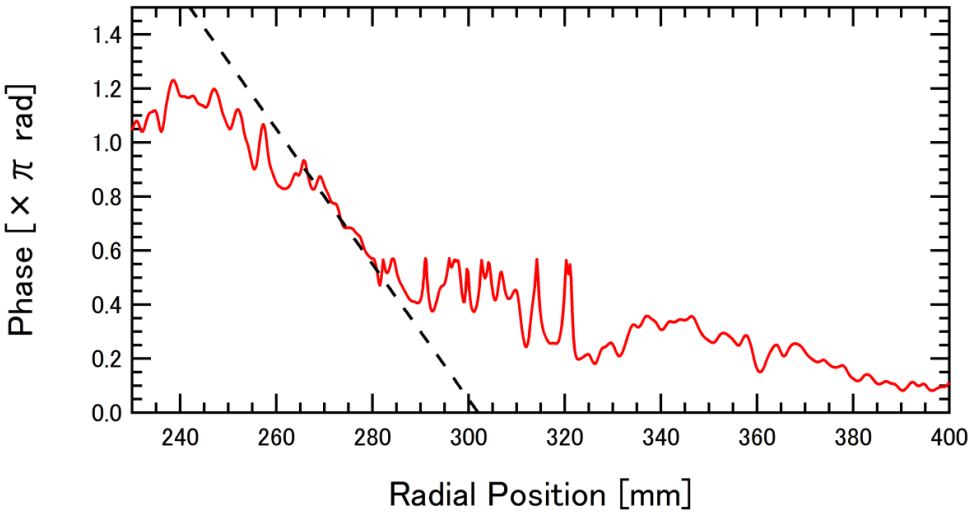

Figure 6.20: The phase profile of longitudinal component

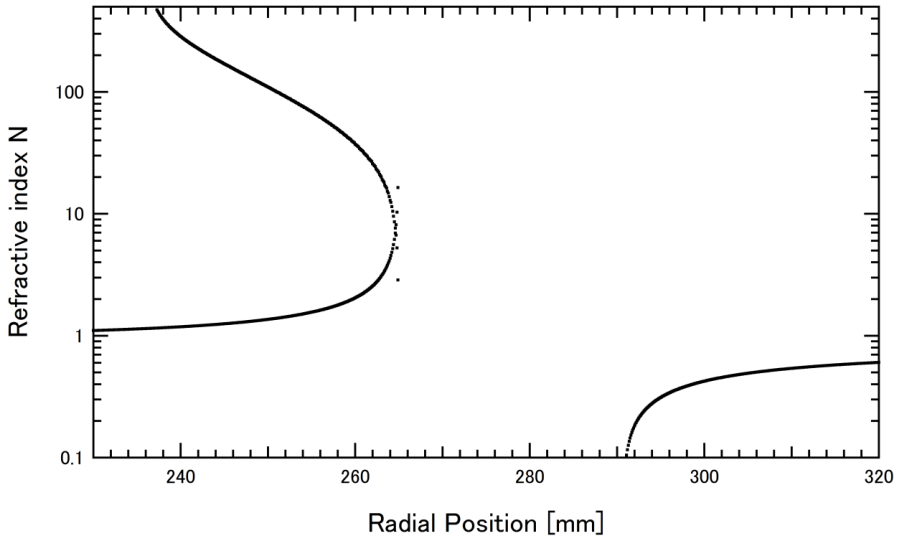

Figure 6.21: Dispersion relation for 1.0 GHz microwaves

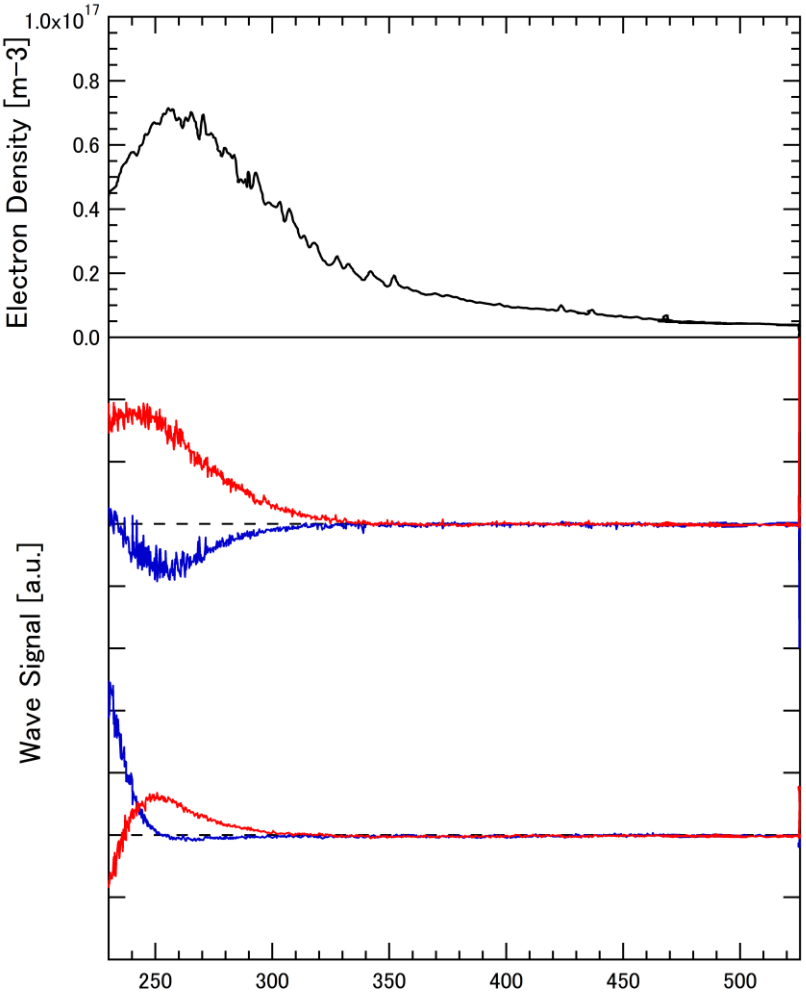

Figure 6.22: SX injection into the too high density plasma

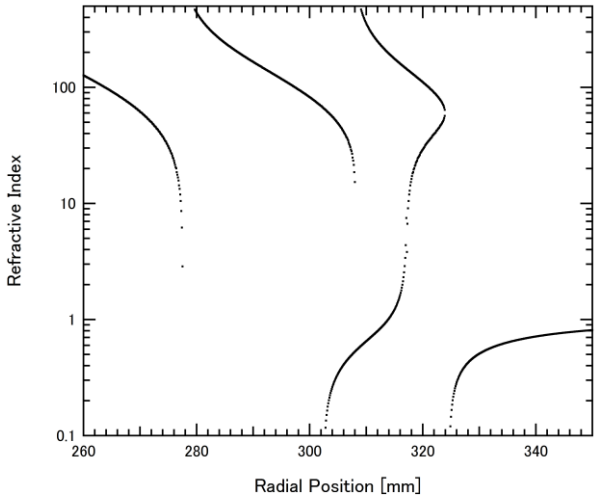

Figure 6.23: Refractive index profile in cutoff case

Chapter 7
Discussion

As shown in the previous chapter, we observed signals having most of the characteristics of the EBW; propagation in the evanescent region, excitation around the UHR, short wavelength, electrostatic mode, backward wave mode and observed at some certain conditions. However, quantitative discrepancies exist between the experimental observations and the theoretical values.

7.1 High Energy Electrons

As mentioned, experimentally observed wavelength is about one order longer than theoretical value. The EBW has a wavelength of the order of the electron Larmor radius, and therefore, the electron temperature is one of the most important parameters for determining their wavelength. The EBW's wavelength of 20 mm represents an electron temperature of approximately 1keV. The plasmas are produced by ECH in the Mini-RT device, and ECH plasmas have possibilities to contain high energy electrons because of quasi-linear diffusion of resonant electrons [62]. Thus, measurements of electron energy distribution function (EEDF) [63] in the Mini-RT were carried out with Druyvesteyn method. The ideal I-V characteristic of Langmuir probe in transition region can be written as [64]

$$I_e(V) = \frac{en_eS_p}{8^{1/2}m_e^{1/2}}\int_{E_c}^{\infty}\left(1-\frac{E_c}{E}\right)E^{1/2}F(E)dE, \tag{7.1}$$

where S_p is surface area of the probe tip, E_c is minimum energy of electron which can reach the probe and $F(E)$ is the EEDF, respectively. By using the second derivative of Eq. (7.1), one can obtain following equation [65] [66];

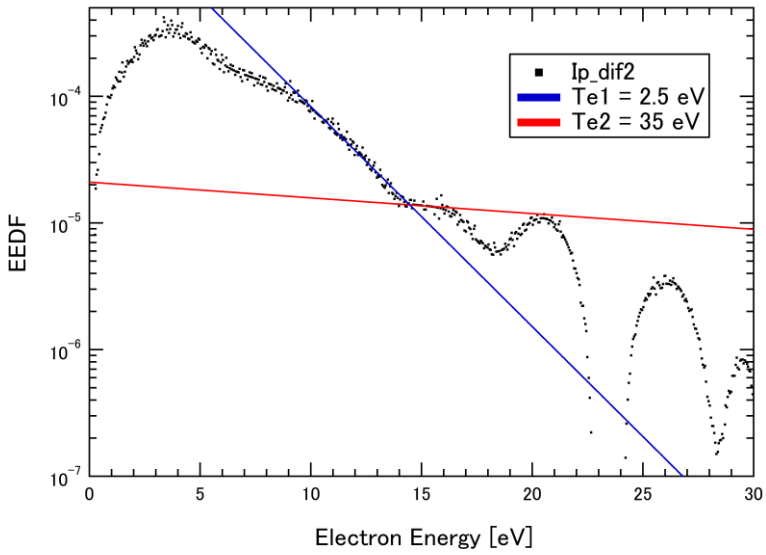

Figure 7.1: EEDF measurement

Two tangential lines represent each electron temperature.

$$\frac{d^2 I_e}{dV^2} = \frac{e^2 S_p n_e}{4}\sqrt{\frac{2e}{m_e}}\frac{F(eV)}{\sqrt{V}}. \tag{7.2}$$

Assuming that the EEDF consists of two-temperature Maxwellian, Eq. (7.2) is proportional to $\exp(-eV\,/\,\kappa T)$.

Figure 7.1 shows a result of EEDF measurement in the Mini-RT plasma. A Langmuir probe is inserted into core plasma region (R = 300 mm), and bias voltage are swept ± 120 V by a bipolar power supply. To obtain EEDF, I-V characteristics curve was differentiated numerically. As shown in Fig. 7.1, differentiated signal is distorted by negative spike noises. Two temperatures estimated from the tangential line by rather main force, are

$$T_{bulk} = 2.5\ eV, \qquad n_{bulk} = 5.0 \times 10^{16}\mathrm{m}^{-3}:\ 80\%$$
$$T_E = 35eV, \qquad n_E = 1.0 \times 10^{16}\mathrm{m}^{-3}:\ 20\%.$$

Starting with the FX-SX-B conversion, the reflective index profile with these parameters is plotted in Fig. 7.2. The high energy electrons affect on the refractive index near the UHR and do not near the ECR. On the other hand, experimentally observed waves, as shown in Fig. 6.6, have constant value of k in broad region. Thus, short-wavelength mode waves observed in Ch. 6 cannot be identified as the EBWs whose wavelength is extended by effects of hi-energy electrons. In addition, high

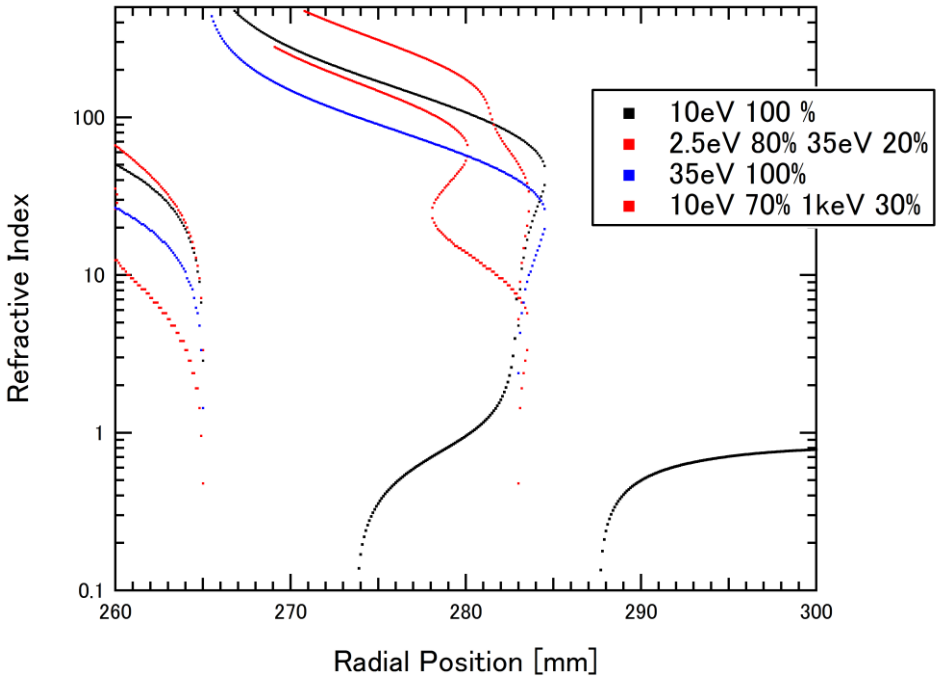

Figure 7.2: Refractive index profiles with two temperature model

energy electrons have an effect on sheath formation and measurement of probes, so that electron density profiles may have much amount of error. The scale and allocation of probes also become something of problems themselves. In this work, the elements of triple probe are adopted tungsten rods whose length and diameter are 5mm and 1.5 mm, respectively. Figure 7.3 shows the comparison between refractive indexes, waveforms and phase profiles for (a) 1.0 GHz, (b) 1.1 GHz and (c) 1.4 GHz with concerning the size of probes. These figures may suggest that the short-wavelength mode is the Slow X mode which is about to be converted into the EBW mode. The reversal of phase profiles means the reflected waves at L-cutoff layer. In addition, even if density profiles could not obtained correctly, the short-wavelength mode moves the location of excitation to inner region according to its frequency, as shown in Fig. 6.8. That is, excitations of this short-wavelength mode occur at a certain region related to plasma density, magnetic field and their frequency.

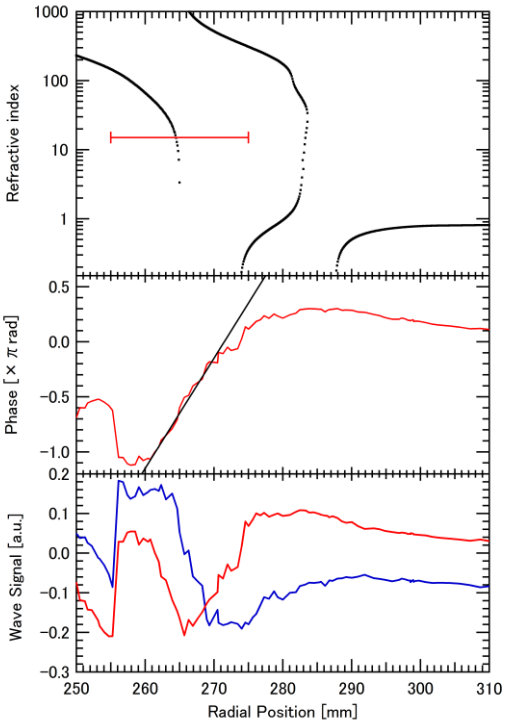

(a) 1.0 GHz

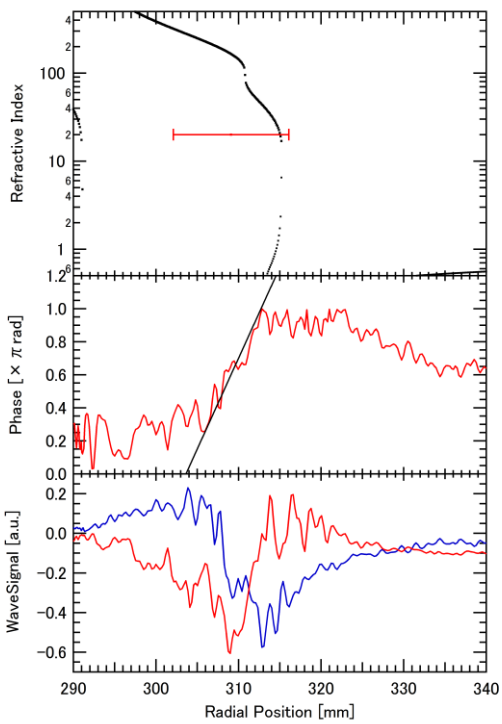

(b) 1.1 GHz

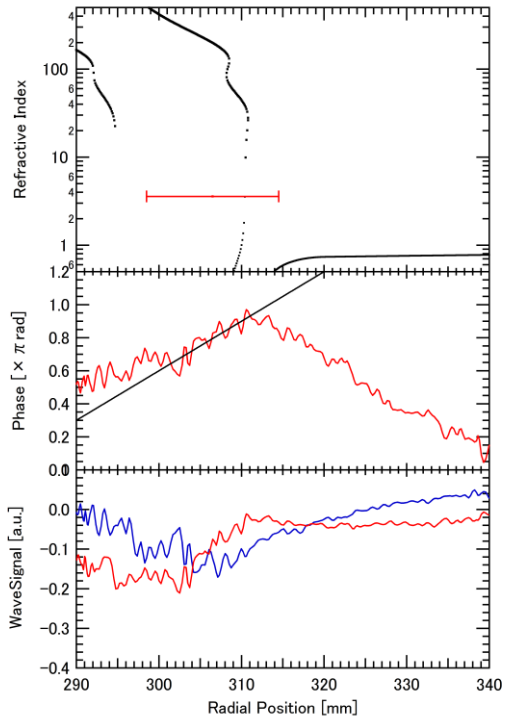

(c) 1.4 GHz

Figure 7.3: Comparisons between Refractive index profiles and locations of excitation short-wavelength mode

Refractive indexes are estimated from tangential lines on phase profiles.

Chapter 8
Conclusion

The objective of this work was to substantiate characteristics of the Electron Bernstein Waves by excitation and measurement in the internal torus plasmas. The EBWs, as well known, have several properties that are undeniably good for heating high beta plasmas, that is, the EBWs have no cutoff density. Recently, to realize advanced nuclear fusion reactors, various plasma confinement and heating methods have been investigated. A dipole confinement is one of the magnetic plasma configuration structures which are similar to a space planet. The Mini-RT device which is an internal coil device was constructed to confine hi-beta plasmas with planetary magnetic field and high density plasma production is achieved. To verify the characteristics of the EBWs in the dipole confinement plasmas, this research dealt with experimental measurement of the EBWs in a directly manner and with numerical simulations by using the Finite-Difference Time-Domain method.

The EBWs are excited at the Upper Hybrid Resonance layer in the plasmas, that is, to harness EBW heating and current drive, it is necessary to inject microwave to the UHR and to convert the mode of incident wave. The excitation scenarios have three accesses to the UHR, i.e. 1) perpendicular X wave injection from high field side, 2) perpendicular X wave injection from low field side and 3) oblique O wave injection from low field side. These three methods are complementary, that is, there is one appropriate approach to excite the EBW according to the target plasmas. On the other hand, the Mini-RT device has two magnetic coils to structure magnetic coordination for plasma confinement, and applying coil current enables us to change plasma profiles easily. Thus, all the three excitation schemes can be applied.

After a brief introduction to the basic physics of waves in plasma, two numerical analyses are demonstrated; one is the trajectory of waves with ray tracing and the other is temporal evolution of mode conversion from electromagnetic mode to electrostatic mode with Finite-Difference Time-Domain method. The ray tracing code demonstrates the propagation of the incident wave as a ray trajectory, i.e. the injected O waves propagate toward the core plasma and the mode of them is converted into the X mode. Furthermore the X waves are converted into the EBWs at the UHR and absorbed at the harmonics of electron cyclotron resonance. Since ray tracing method uses the approximation of geometrical optics, to investigate propagation of waves in the Mini-RT, the Maxwell equations needs to be directly solved. Thus, the FDTD method is adapted to the wave analysis in the Mini-RT. By taking into account the warm plasma effects on the FDTD code, FX-SX-B conversion is demonstrated in 1D plasma model with time development.

For experimental verification of properties of the EBWs, waves in plasma are directly measured with probing antenna by interferometry demodulation. To examine the mode conversion of the waves from the electromagnetic mode to the electrostatic one, the electromagnetic and electrostatic components were measured simultaneously. The experimental results show many properties of mode conversion from electromagnetic to electrostatic. That is;

(i) EBWs have no cutoff density.

➔ Experimentally excited waves propagate in higher density region than cutoff density.

(ii) They are electrostatic mode waves.

➔ Comparison with signals emitted by magnetic loop antennas show the waves do not have electromagnetic component.

(iii) They are excited by mode conversion at the UHR layer.

➔ Characteristics of the waves, such as wavelength, spatial phase gradient, amplitudes of electrostatic and magnetic component and polarization, drastically change at the UHR. In addition, according to the transfer of the UHR by variations in plasma confinement and frequencies of the incident microwaves, the locations of

these changes are shifted to the expected region.

(iv) Their typical value of the wavelength is of the order of the Larmor radius.

➔ The wavelength obtained by experimental results is much smaller than that in vacuum, but it is about one order larger than that obtained from dispersion relation.

(v) They are longitudinal polarized.

➔ Pole antennas directed to the radial, toroidal and poloidal direction show the waves mainly have longitudinal polarization.

(vi) They are backward wave mode (they have negative group velocity).

➔ The reverse of phase gradient suggests the change of the direction of wave number vector and phase velocity; however this is clearly observed in FX-SX-B conversion only due to the superposition of multiple modes around the UHR.

Furthermore,

(vii) they have three excitation scenarios and each scenarios have a certain proper condition.

➔ In FX-SX-B conversion, the short-wavelength mode having above properties is obviously observed with the small distance between the R-cutoff and the UHR, i.e. necessity of steep gradient of density profile has been shown in the experiments.

➔ In O-X-B conversion, the short-wavelength mode is observed in a certain initial injection angle, and the angle varies with changes in plasma configuration. The experimental results show the angle between incident waves and magnetic field has a significant relationship to excitation of the short-wavelength mode.

➔ In SX-B conversion, the short-wavelength mode is observed in high density plasma without appearing the evanescent region. This result indicates the density limit of EBW excitation and plasma heating.

As seen above, observed signals have most characteristics of the EBWs, but their wavelength is about one order larger than theoretical one. Since the energetic electrons have a great affect on the wavelength of EBWs made of electron coherent motion, measurement of energy distribution functions are carried out. Although the EEDF measurement may suggest the existence of high energy electrons, they are inadequacy for explanation. Taking into account of the scale of probes as an error

factor, the short-wavelength mode is considered as the Slow X mode which is about to be converted into the EBW mode. We could not obtain decisiveness evidences of direct observation of the EBWs, but at least, we have directly observed that the injected wave reach to the UHR and change its characteristics. Therefore, it would be safe to say that directly observation of excitation scheme in all the three methods is achieved.

Bibliography

[1] R. Feldcacher, "Nuclear Reaction Cross Sections and Reactivity Parameter Library and Files," Wagramerstrasse Vienna, (1987).

[2] T. Watanave and H. Akio, "Analytical Curve Fitting for Maxwellian Reactiveties," J. Jap. Soc. Plasma Science and Nucl. Fus. Res. **74**, 850 (1998).

[3] C. F. Wandel *et al.*, "A Compilation of Some Rates and Cross Sections of Interest in Controlled Thermonuclear Research," Nuclear Instruments and Methods **4**, 249 (1959).

[4] J. D. Lawson, "Some Criteria for a Power Producing Thermonuclear Reactor," Proc. Phys. Soc. B **70**, 6 (1957).

[5] S. M. Mahajan and Z. Yoshida, "Double Curl Beltrami Flow: Diamagnetic Structures," Phys. Rev. Lett. **88**, 4863 (1998).

[6] Z. Yoshida *et al.*, "Variational Principles and Self-Organization in Two-Fluid Plasmas," Phys. Rev. Lett. **88**, 095001 (2002).

[7] O. Mitarai *et al.*, "Plasma Current Start-up by ECW and Vertical Field in the TST-2 Spherical Tokamak," J. Plasma Fusion Res. **80**, 549 (2004).

[8] Hiroshi Gota *et al.*, "Separatrix shapes and internal structures of a field-reversed configuration plasm," Phys. Plasma **10**, 4763 (2003).

[9] E. A. Lazarus *et al.*, "Higher beta at higher elongation in the DIIID tokamak," Phys. Fluids B **8**, 2220 (1991).

[10] K. Kobayashi *et al.*, "Design status of EC system in ITER," Fusion Eng. Des. **53**, 475 (2001).

[11] H. P. Laqua, "Electron Bernstein wave heating and diagnostic," Plasma Phys. Control. Fusion **49**, R1 (2007).

[12] J. Preinhaelter *et al.*, "EBW power deposition and current drive in WEGW –

comparison of simulation with experiment," Plasma Phys. Control. Fusion **51**, 125008 (2009).

[13] V. F. Shevchenko *et al.*, "Electron Bernstein wave assisted plasma current start-up in MAST," Nucl. Fusion **50**, 022044 (2010).

[14] S. Shiraiwa *et al.*, "Heating by an Electron Bernstein Wave in a Spherical Tokamak Plasma via Mode Conversion," Phys. Rev. Lett. **96**, 185003 (2006).

[15] Y. Yoshimura *et al.*, "Electron Bernstein wave heating by electron cyclotron wave injection from the high-field side in LHD," Nucl. Fusion **53**, 063004 (2013).

[16] H. Igami *et al.*, "Experimental Results for Electron Bernstein Wave Heating in the Large Helical Device," Plasma and Fusion Res. **7**, 2402110 (2012).

[17] I. B. Bernstein, "Waves in a Plasma in a Magnetic Field," Phys. Rev. **109**, 10 (1958).

[18] K. Mitani, "Microwave Radiation from a Plasma in a Magnetic Field (I)," J. Phys. Soc. Japan **19**, 211 (1964).

[19] G. S. Kino and H. H. Weiss F. W. Crwford, "Excitation of Cyclotron Harmonic Resonances in a Mercury-Vapor Discharge," Phys. Rev. Lett. **17**, 229 (1964).

[20] R. S. Harp, "Propagation of Longitudinal Plasma Oscillations near Cyclotron Harmonics," App. Phys. Lett. **6**, 51 (1965).

[21] J. Preinhaelter and V. Kopecký, "Penetration of high-frequency waves into a weakly inhomogeneous magnetized plasma at oblique incidence and their transformation to Bernstein modes," J. Plasma Phys **10**, 1 (1973).

[22] T. Maekawa *et al.*, "Numerical Studies of Wave Trajectories and Electron Cyclotron Heating in Toroidal Plasmas," J. Phys. Soc. Jpn. **48**, 247 (1980).

[23] S. Gruber *et al.*, "Excitation of Longitudinal Waves near Electron - Cyclotron Harmonics," Phys. Fluids **11**, 122 (1968).

[24] H.Sugai, "Mode Conversion and Local Heatingbelow the Second Electron Cyclotron Harmonic," Phys. Rev. Lett. **47**, 1899 (1981).

[25] Y. Y. Podova *et al.*, "Direct Observation of Electron-Bernstein Wave Heating by

O-X-B Conversion at Low Magnetic Field in the WEGA Stellarator," Phys. Rev. Lett. **98**, 255003 (2007).

[26] F. F. Chen, *Introduction to Plasma Physics and Controlled Fusion*. Plenum Press, New York (1984).

[27] H. T. Stix, *The Theory of Plasma Waves*. McGraw-Hill, New York (1962).

[28] H. T. Stix, *Waves in Plasmas*. American Institute of Physics, New York (1992).

[29] D. G. Swanson, *Plasma Waves*, 2nd ed. Institute of Physics Publishing, Bristol (2003).

[30] T.H.Stix, "Radiation and Absorption via Mode Conversion in an Inhomogeneous Collisionfree Plasma," Phys. Rev. Lett. **15**, 878 (1965).

[31] S. J. Bucksbaum, A. Bers W. P. Allis, *Waves in Anisotropic Plasmas*. MIT Press, Cambridge, Massachusetts (1963).

[32] K. Miyamoto, *Plasma Physics and Controlled Nuclear Fusion*. University of Tokyo Press, Tokyo (2004).

[33] K. G. Budden, *Radio Waves in the Ionosphere*. Cambridge Univ Press, London (1961).

[34] A. K. Ram *et al.*, "Mode conversion of fast Alfvén waves at the ion-ion hybrid resonance," Phys. Plasmas **3**, 1976 (1996).

[35] A. K. Ram and S. D. Schultz, "Excitation, Propagation, and damping of electron Bernstein waves in Tokamaks," Phys. Plasmas **7**, 4084 (2000).

[36] H. Weitzner and D. B. Batchelor, "Conversion between Cold Plasma Modes in an Inhomogeneous Plasma," Phys. Fluids **22**, 1355 (1979).

[37] F. Volpe, "Analytical solution of the O-X mode conversion problem," Physics Letters A **374**, 1797 (2010).

[38] E. Mjølhus, "Coupling to Z mode near critical angle," J. Plasma Phys. **31**, 7 (1984).

[39] F. R. Hansen *et al.*, "Full-wave calculations of the O-X mode conversion process," J. Plasma Phys. **39**, 319 (1988).

[40] T. E. Dowling, W. B. Mckinnon F. Bagenal, *Jupiter : the planet satellites*

magetosphere. Cambridge University Press, New York (2004).

[41] Y. Ogawa *et al.*, "Research on high-Beta Plasma Based in Two-Fluid Relaxation Teoly," J. Plasma Fusion Res. **5**, 100 (2002).

[42] Z. Yoshida *et al.*, "First Plasma in the RT-1 Device," Plasma and Fusion Res. **1**, 008 (2006).

[43] K. Natsume *et al.*, "Experimental Results of the HTS Floating Coil Using REBCO Tapes for the Mini-RT Upgrading," IEEE Transactions on Applied Superconductivity **24**, 460114 (2014).

[44] Y. Ogawa *et al.*, "Design, Fabrication, and Persistent Current Operation of the REBCO Floating Coil for the Plasma Experimental Device Mini-TY," Plasma and Fusion Res. **9**, 1405014 (2014).

[45] T. Uno, *Finite Difference Time Domain Method for Electromagnetic Field and Antennas*. Corona Publishing Co., Tokyo (1998).

[46] U. S. Inan and R. A. Marshall, *the FDTD method*. Cambridge University Press, New York (2011).

[47] H. Hojo *et al.*, "2D Full Wave Simulation on Electromagnetic Wave Propagation in Toroidal Plasma," J. Plasma Fusion Res. **78**, 387 (2002).

[48] A. Kohn *et al.*, "Full-wave modeling of the O–X mode conversion in the Pegasus toroidal experiment," Phys. of Plasmas **18**, 082501 (2011).

[49] K. Yee, "Numerical solution of initial boundary value problems involving maxwell's equations in isotropic media," IEEE Transactions on Antennas and Propagation **14**, Issue 3, 302 (1966).

[50] A. Taflove, "Reivew of the formulation and applications of the finite-difference time-domain method for numerical modeling of electromagnetic wave interactions with arbitrary structures," Wave Motion **10**, 547 (1988).

[51] A. Taflove and S.C. Hagness, *Computational Electrodynamics: The Finite-Difference Time-Domain Methos*. Artech House, Boston (2005).

[52] W. Webb and L. Hanzo, *Modern quadrature modulation: principles and applications for fixed and wireless communications*. Pentech Press, London

(1994).

[53] M. Brambilla, "Finite Larmor Radius Wave Equations in Tokamak Plasmas in the Ion Cyclotron Frequency Range," Plasma Phys. Control. Fusion **31**, 723 (1989).

[54] M. Brambilla, "Numerical simulation of ion cyclotron waves in tokamak plasmas," Plasma Phys. Control. Fusion **41**, 1 (1999).

[55] P. J. Barret *et al.*, "Dispersion of Electron Plasma Waves," Plasma Phys. **10**, 911 (1968).

[56] I. Toshitaka *et al.*, "Instability of the Trivelpiece Mode in a Magnetized Beam-Plasma System," J. Phys. Soc. Jap. **42**, 1730 (1977).

[57] J. A. C. Cabral, "Coupling of a Trivelpiece-Gould wave to a new type of electromagnetic wave observed around the electron cyclotron frequency in an inhomogeneous plasma column," Plasma Phys. Control. Fusion **31**, 267 (1989).

[58] Roy Ediss, "Probing the magnetic field probe," EMC & Compliance Journal, Issue 47 (2003).

[59] S. Adachi, *Electromagnetic Engineering*. Corona Publishing Co., Tokyo (1983).

[60] L. Millanta and L. Chiosi, C. Carobbim, "The-high frequency behavior of the shield in the magnetic probes," Electromagnetic Compatibility, IEEE International Symposium **1**, 35 (2000).

[61] S. L. Chen and T. Sekiguchi, "Instantaneous Direct - Display System of Plasma Parameters by Means of Triple Probe," J. Appl. Phys. **36**, 2363 (1965).

[62] C. F. Kennel *et al.*, "Velocity Space Diffusion from Weak Plasma Turbulence in a Magnetic Field," Phys. Fluids **9**, 2377 (1966).

[63] K. Uehara *et al.*, "Electron Energy Distribution Function Measured by Electrostatic Probes at Divertor Plasma in JFT-2M Tokamak," Jpn. J. Appl. Phys. **42**, 657 (2003).

[64] B. H. M. Mott-Smith and I. Langmuir, "The Theory of Collectors in Gaseous Discharges," Phys. Rev. **28**, 727 (1926).

[65] M. J. Druyvestein, "Der Niedervoltbogen," Z. Phys. **64**, 781 (1930).

[66] O. Kazuyuki, "Measurements of Electron Energy Distribution Function," Jap. Soc. Plasma Sci. and Nuclear Fusion Res. **69**, 939 (1993).

[67] H. P. Laqua *et al.*, "Electron-Bernstein-Wave Current Drive in an Overdense Plasma at the Wendelstein 7-AS Stellarator," Phys. Rev. Lett. **90**, 075003 (2003).

[68] J. Preinhaelter and V. Kopecky, "Penetration of High - Frequency Waves into A Weakly Inhomogeneous Magnetized Plasma atOblique Incidence and Their Transformation to Bernstein Modes," Institute of Plasma Physics Czechoslovak Academy of Sciences, research report (1972).